



JÖNKÖPING UNIVERSITY
School of Engineering

Doctoral Thesis

Control of Particles Codeposition and Strengthening Mechanisms in Nickel Based Nanocomposite Coatings

Santiago Piñate

Jönköping University
School of Engineering
Dissertation Series No. 063 • 2021



JÖNKÖPING UNIVERSITY

School of Engineering

Doctoral Thesis

Control of Particles Codeposition and Strengthening Mechanisms in Nickel Based Nanocomposite Coatings

Santiago Piñate

Doctoral thesis in Materials and Manufacturing

Control of Particles Codeposition and Strengthening
Mechanisms in Nickel Based Nanocomposite Coatings
Dissertation Series No. 063

© 2021 Santiago Piñate

Published by
School of Engineering, Jönköping University
P.O. Box 1026
SE-551 11 Jönköping
Tel. +46 36 10 10 00
www.ju.se

Printed by Stema Specialtryck AB, year 2021

ISBN 978-91-87289-67-5



ABSTRACT

Surface durability is a key factor in the service life of components. Depending on the aggressiveness of the environment, surface deterioration by wear or corrosion leads to failure of the bulk material and eventually to the loss of functionality of the component. Therefore, designing surfaces to withstand service requirements is a critical aspect for industrial product realisation.

Electroplating is an attractive technique to mass-produce affordable protective coatings due to its low cost and high performance, easy maintenance of the process, and adjustable production times. Producing nanocomposite coatings by electroplating has received significant attention for decades due to their potential to provide excellent wear and corrosion protection.

Nanocomposites provide the possibility of combining different materials to achieve multifunctionality and, due to the nanometer size of the reinforcer phase, promote additional strengthening effects in the matrix not present in microcomposites. Additionally, the reduction in the size of the reinforcer provides advantages in wear protection as the risk of third-body abrasion is reduced. However, the industrial applicability remains limited due to the lack of control in their production process.

The present work focuses on the relationship between the input parameters and the codeposition of SiC, MoS₂ and graphite particles, identifying critical factors and providing methods to control the process better. Furthermore, a correlation between the nickel matrix microstructure and codeposition is established, linking them to the strengthening effects and final performance of the nanocomposite coating.

New methods were developed to provide a reproducible electroplating process. A surface treatment for the reinforcing powder minimised the differences between the particles surface state deriving from different batches, supplier or production routes. Composites produced with surface-treated nanoparticles showed reproducible results displaying similar codeposition rate and

hardness values. Additionally, a pulse-reverse plating waveform, adapted to the SiC particles average size, was designed and optimised to deposit a reproducible and improved particles content even in the presence of anionic surfactants, typically used to reduce coatings porosity and defects.

The study of the impact of the reinforcer phase on the electrocrystallisation of the nickel matrix showed that the microstructure was significantly affected by the size, chemistry and dispersion of the particles, promoting changes in the preferred crystal orientation, grains morphology and size. The strengthening mechanisms were linked to the microstructural changes resulting from the process parameters, particles codeposition and the agitation mode. Different models were used to predict the hardness of the composites based on the contribution and combination of each strengthening factor: Hall-Petch, Orowan, enhanced dislocation density and particles incorporation, showing a good agreement with the experimental data.

Furthermore, the wear behaviour of the composites was analysed and connected to the hardening effects. The analysis highlighted how particles content, dispersion, type and size of the reinforcer contribute to the protection against wear.

A novel multifunctional composite coating based on a dual dispersion mix of hard SiC particles and self-lubricant MoS₂ particles was designed, resulting in a surface with high hardness, low friction and low wear.

Keywords: *Dispersion coatings; nanocomposite; Controlled particles codeposition; Surface treatment; ζ -potentials; Pulse-reverse deposition; Ultrasound agitation; ElectrocrySTALLISATION; Microstructure; Strengthening mechanisms; Hardness; Wear.*

SAMMANFATTNING

Ytors robusthet är en nyckelfaktor för komponenters livslängd. I krävande applikationsmiljöer kan ytan skadas av korrosion eller nötning som fortplantar sig till basmaterialet vilket kan leda till att komponenten förlorar sin funktionalitet. Det är därför viktigt att under produktutveckling konstruera komponenttytor som motstår tilltänkta driftsmiljöer.

Elektroplätning är en attraktiv metod för kostnadseffektiv volymtillverkning av skyddande funktionella beläggningar då processen är flexibel och enkel att underhålla. Därför har också möjligheten att elektroplätera nano-kompositbeläggningar med utmärkta nötnings- och korrosionsegenskaper uppmärksamats de senaste decennierna.

Nano-kompositer öppnar för möjligheten att kombinera olika material för att uppnå multifunktionalitet. Nano-partiklarna bidrar med en härdningseffekt utöver vad som kan uppnås med mikro-partiklar. Ytterligare är risken för nötningsskador på grund av lösrivna partiklar mindre för nano-kompositer. Dock är den industriella användningen begränsat av att tillverkningsprocessen är svår att kontrollera.

Denna avhandling fokuserar på förhållandet mellan ingångsparametrar och inkorporering av SiC-, MoS₂- och grafitpartiklar genom att identifiera kritiska faktorer och tillhandahåller metoder för bättre processkontroll. Dessutom har ett samband mellan nickelmатrisens mikrostruktur och inkorporerade partiklar identifierats som förklarar härdningseffekten och kompositbeläggningens egenskaper.

Nya metoder för att skapa en reproducerbar pläteringsprocess har utvecklats. En förberedande ytbehandling av partiklarna minskar skillnader i ytkemiska egenskaper härstammande från olika leveranser, producenter och tillverkningsmetoder. Kompositbeläggningar tillverkade med ytbehandlade partiklar var reproducerbara med avsikt på partikelhalt och hårdhet. Ytterligare designades en bipolär strömpuls anpassad efter SiC-partiklarnas

genomsnittliga storlek så att en reproducerbar ökad partikelmängd kan inkorporeras. Detta gäller även i närvaro av anjoniska ytaktiva medel, som vanligtvis används för att minska beläggningens porositet och defekter.

Studien av partiklarnas påverkan på elektrokristallisationen av nickelmatriken visade att partiklarnas storlek, sammansättning och spridning hade en avsevärd effekt på mikrostrukturen. Partiklarna påverkade den föredragna kristallorienteringen samt kornens form och storlek. Härdningsegenskaperna kopplades till förändringar i mikrostrukturen beroende på processparametrar, partikelinkorporering och omrörningsläget. Olika modeller användes för att förutsäga kompositernas hårdhet baserat på bidrag från följande härdningsfaktorer: Hall-Petch, Orowan, ökad dislokationstäthet och partikelinkorporering, vilka visade god överensstämmelse med experimentella data.

Slutligen undersöktes kompositbeläggningarnas nötningsegenskaper och kopplades till partikelhärdning. Särskild vikt lades på hur partikelhalten, -spridningen, -typen och -storleken bidrar till skyddet mot slitage.

En ny multifunktionell komposit baserad på en dubbel dispersionsblandning av hårda SiC-partiklar och självsmörjande MoS₂-partiklar utvecklades och resulterade i en yta med hög hårdhet, låg friktion och lågt slitage.

Nyckelord: *Dispersionsbeläggning; nanokomposit; kontrollerad inkorporering av partiklar; ytbehandling; zeta-potential; bipolär pulsplätering; ultraljudsomrörning; elektrokristallisation; mikrostruktur; härdningsmekanism; hårdhet; nötning.*

ACKNOWLEDGEMENT

I would like to express my sincere gratitude to:

KK-Stiftelsen for the financial support that made the project FunDisCo (project reference number 20310117) possible.

The industrial partners in the FunDisCo consortium Husqvarna, Swedev, LPTech and Candor Sweden.

My main supervisor Prof. Caterina Zanella, for her continuous patient, guidance and care. Thank you for the support and inspiration to grow as a researcher.

My supervisor Prof. Peter Leisner for his valuable comments and suggestions. Thank you for the inspiring scientific talks and assistance, which helped me during this work.

COST Action MP1407 for providing the funds and supporting my short-term scientific mission hosted in Technische Universität Ilmenau, Germany, and financing my participation in the e-MINDS training school in Germany, Belgium and Hungary. Thank you to all the committee members.

Technische Universität Ilmenau, Germany, especially Prof. Andreas Bund and Dr Adriana Ispas, for hosting my visit and your help in the characterisation of ζ -potentials.

Linköping University, Sweden, Assoc. Prof. Fredrik Eriksson for his contribution with the XRD measurements, and Prof. Per Persson and Dr Ingemar Persson for their contribution with the TEM imaging and analysis. Thank you for your help.

Prof. Andrew Cobley, thank you for the fruitful discussions, which helped me to improve this work.

Assoc. Prof. Ehsan Ghassemali, thank you for your contribution and assistance through these years, and thank you to all my colleagues and friends at the Department of Material and Manufacturing. I am especially thankful to Dr Maximilian Sieber for his help and Nessrine Nefzi, Jacob Steggo, Toni Bogdanoff, Dr Johan Börjesson and Dr Patrick Conway for their support in the experimental and characterisation work.

All my friends around the world. Even if we might be apart, there was never a distance in my heart.

Jerri, Anna and Lisa for being my adoptive loving family in Sweden.

My parents and siblings, I am forever grateful for your support and endless love. My love knows no distance.

My wife, Sofia. With you, I am at home. I love you.

Santiago Piñate Horrillo, Jönköping 2021.

SUPPLEMENTS

The following supplements constitute the basis of this thesis:

Supplement I

S. Pinate, A. Ispas, P. Leisner, C. Zanella

Electrocodeposition of Ni composites and surface treatment of SiC nano-particles

Surface and Coatings Technology, 2021. Vol. 406, pp. 12663

DOI: 10.1016/j.surfcoat.2020.126663 ([*Open access*](#))

CRedit (Contributor Roles Taxonomy) statement:

S. Pinate: Methodology, Validation, Formal analysis, Investigation, Writing - Original Draft, Visualization.

A. Ispas: Investigation, Resources, Writing - Review & Editing.

P. Leisner: Conceptualisation, Methodology, Validation, Writing - Review & Editing.

C. Zanella: Conceptualisation, Methodology, Validation, Resources, Writing - Review & Editing, Supervision, Project administration, Funding acquisition.

Some of the work published in the supplement was partially disclosed in the 4th WORKSHOP e-MINDs, COST Action MP1407, Milano, Italy 2019 as an oral presentation, and in the PRiME 2020, Pacific Rim Meeting on Electrochemical and Solid State Science as a conference video presentation titled:

Surface modification of nano-size SiC powders and Can We Consider SiC Nanoparticles Inert When We Add Them to Electrodeposition Systems?

Supplement II

S. Pinate, P. Leisner, C. Zanella

Electrocodeposition of nano-SiC particles by pulse-reverse under an adapted waveform

Journal of The Electrochemical Society, 2019. Vol. 166, pp.

D804-D809. DOI: 10.1149/2.0441915jes

CRedit (Contributor Roles Taxonomy) statement:

S. Pinate: Conceptualisation, Methodology, Validation, Formal analysis, Investigation, Writing - Original Draft, Visualisation.

P. Leisner: Methodology, Validation, Writing - Review & Editing.

C. Zanella: Conceptualisation, Methodology, Validation, Resources, Writing - Review & Editing, Supervision, Project administration, Funding acquisition.

Some of the work published in the supplement was partially disclosed in the Electrochem 2019, Glasgow, Scotland, as part of the conference oral presentation titled:

Electrocodeposition of nano-SiC particles under an adapted Pulse-reverse waveform.

Supplement III

S. Pinate, N. Nefzi, C. Zanella

Role of anodic time in pulse-reverse electrocodeposition of nano-SiC particles

Manuscript submitted for journal publication

CRedit (Contributor Roles Taxonomy) statement:

S. Pinate: Conceptualisation, Methodology, Validation, Formal analysis, Investigation, Writing - Original Draft, Visualization, Supervision.

N. Nefzi: Investigation, Writing - Review & Editing.

C. Zanella: Conceptualisation, Methodology, Validation, Resources, Writing - Review & Editing, Visualization, Supervision, Project administration, Funding acquisition.

Supplement IV

S. Pinate, F. Eriksson, P. Leisner, C. Zanella

Effects of particles codeposition and ultrasound agitation on the electrocrystallization of metal matrix composites

Manuscript submitted for journal publication

CRedit (Contributor Roles Taxonomy) statement:

S. Pinate: Methodology, Validation, Formal analysis, Investigation, Writing - Original Draft, Visualization.

F. Eriksson: Validation, Investigation, Formal analysis, Resources, Writing - Review & Editing.

P. Leisner: Conceptualisation, Methodology, Validation, Writing - Review & Editing.

C. Zanella: Conceptualisation, Methodology, Validation, Formal analysis, Resources, Writing - Review & Editing, Supervision, Project administration, Funding acquisition.

Some of the work published in the supplement was partially disclosed in the 32nd International Conference on Surface Modification Technologies (SMT32), San Sebastian, Spain 2018 as part of the conference oral presentations titled:

Effect of the electrocrystallization condition on the passivity of Ni matrix composite coatings, and

Influence of the particle size on the electrocrystallization of nickel matrix composite coatings.

Supplement V

S. Pinate, C. Zanella

Wear behaviour of Ni-based composite coatings with dual nano-SiC:Graphite powder mix

Coatings, 2020. Vol. 10, pp. 1060.

DOI: 10.3390/coatings10111060 ([Open access](https://doi.org/10.3390/coatings10111060))

CRedit (Contributor Roles Taxonomy) statement:

S. Pinate: Conceptualisation, Methodology, Validation, Formal analysis, Investigation, Writing - Original Draft, Visualisation.

C. Zanella: Conceptualisation, Methodology, Validation, Formal analysis, Resources, Writing - Review & Editing, Visualization, Supervision, Project administration, Funding acquisition.

Supplement VI

S. Pinate, P. Leisner, C. Zanella

Wear resistance and self-lubrication of electrodeposited Ni-SiC:MoS₂ dual composite coatings

Manuscript submitted for journal publication

CRedit (Contributor Roles Taxonomy) statement:

S. Pinate: Conceptualisation, Methodology, Validation, Formal analysis, Investigation, Writing - Original Draft, Visualisation.

P. Leisner: Methodology, Validation, Writing - Review & Editing.

C. Zanella: Conceptualisation, Methodology, Validation, Formal analysis, Resources, Writing - Review & Editing, Visualization, Supervision, Project administration, Funding acquisition.

Supplement VII

S. Pinate, E. Ghassemali, C. Zanella

Strengthening mechanisms by particles codeposition and wear behaviour of electroplated Ni-SiC coatings

Manuscript for journal publication

CRedit (Contributor Roles Taxonomy) statement:

S. Pinate: Conceptualisation, Methodology, Validation, Formal analysis, Investigation, Writing - Original Draft, Visualisation.

E. Ghassemali: Formal analysis, Investigation, Writing - Review & Editing.

C. Zanella: Conceptualisation, Methodology, Validation, Formal analysis, Resources, Writing - Review & Editing, Supervision, Project administration, Funding acquisition.

TABLE OF CONTENTS

CHAPTER 1 INTRODUCTION.....	1
1.1 BACKGROUND.....	1
1.2 METAL MATRIX COMPOSITE COATINGS.....	2
1.2.1 Strengthening mechanisms in nanocomposites.....	3
1.3 ELECTRODEPOSITION	6
1.3.1 Basic principles of electrocrystallisation and controlling parameters.....	7
1.3.2 Composite Electrodeposition.....	11
1.4 STATE OF THE ART	17
1.4.1 Gap between previous research and the present study.....	17
CHAPTER 2 RESEARCH OBJECTIVE	21
2.1 PURPOSE AND AIM	21
2.2 RESEARCH DESIGN.....	22
2.2.1 Research perspective.....	22
2.2.2 Research questions.....	22
CHAPTER 3 RESEARCH APPROACH	25
3.1 RESEARCH STRATEGY AND METHODOLOGY	25
3.1.1 Research strategy.....	25
3.1.2 Research ethics and quality assurance	27
3.2 MATERIALS AND EXPERIMENTAL PROCEDURE.....	28
3.2.1 Materials.....	28
3.2.2 Electrodeposition parameters and set-up.....	31
3.3 CHARACTERISATION AND TESTING	34
3.3.1 Sample preparation.....	35
3.3.2 Characterisation of particles in suspension	35
3.3.3 Imaging techniques	37
3.3.4 Non-Imaging techniques	39
3.3.5 Tribological tests	43

CHAPTER 4 SUMMARY OF RESULTS AND DISCUSSION.....	45
4.1 INTERACTIONS BETWEEN PARTICLES AND ELECTROLYTE.....	45
4.1.1 Surface treatment	46
4.1.2 Particles ζ -Potentials and particles size	47
4.1.3 Titration	48
4.2 PARTICLES CODEPOSITION	50
4.2.1 Effects on hydrogen evolution reaction (HER)	50
4.2.2 Particles codeposition rate	52
4.3 MICROSTRUCTURAL CHANGES.....	61
4.4 HARDNESS AND WEAR BEHAVIOUR.....	72
4.4.1 Hardening by particles codeposition	72
4.4.2 Strengthening mechanisms	74
4.4.3 Wear behaviour	82
CHAPTER 5 CONCLUSIONS	89
CHAPTER 6 FUTURE WORK	93
REFERENCES	95
APPENDED PAPERS	109

INTRODUCTION

CHAPTER INTRODUCTION

The purpose of this chapter is to provide the fundamental principles on electrodeposition of nickel matrix composite coatings. This chapter covers important definitions and concepts that are used in the following chapters.

1.1 BACKGROUND

Surface durability is a key aspect of industrial product realisation. The surface of the component is first to respond to the aggressiveness of the environment, and its deterioration can lead to the failure of the bulk material and eventual loss of the functionality of the component. Thus, the design of durable surfaces often ranks highly on the product development requirements as it is critical for the service life of the component.

The type of interactions between surface and environment varies depending on the application of the product. Surfaces require tailoring of the properties for each particular use. Moving parts, for example, are under constant tribological load and must withstand wear. Hard coatings act as protective layers for the bulk material by increasing the surface wear resistance when properly applied. Different coating techniques such as sol-gel, CVD, PVD, and electroless/electrodeposition are available methods to produce coatings to improve wear resistance [1]. Electroplating is an attractive technique due to the easy maintenance of the process, its low cost and high performance, and adjustable production times to mass-produce affordable pure metals, alloys or metal matrix

composite capable of granting wear resistance when deposited on the surface.

Electroplated protective hard chromium coatings have been widely applied across Europe due to their wear resistance and corrosion protection in car components, tools and cutting devices [2]. The European Chemicals Agency (ECHA) has, however, enforced in REACH ("Registration, Evaluation, Authorisation and Restriction of Chemicals") the restriction to hexavalent chromium [3], a key ingredient in the electrodeposition of these coatings because of the environmental hazard and carcinogenic threat on humans. These new policies force European companies to adapt and find suitable alternatives for hard chromium while providing coatings with similar performance, also fulfilling the new regulations.

Composite coatings are one of the readily available alternatives to be produced by electrodeposition. Composite materials offer the capability of tailoring the surface based on the requirements of the component and application. For instance, wear-resistance coatings combine a corrosion-resistant metal acting as the matrix and a second phase where hard particles are used to harden the material and self-lubricating particles to decrease friction [1,4]. Considering that the performance of the composite coating rests on the successful incorporation of the reinforcer, a technological challenge is assuring the controlled incorporation of the reinforcer material.

1.2 METAL MATRIX COMPOSITE COATINGS

Metal matrix composite materials are made by combining two or more materials [4]. The metal acts as the matrix, and the other is incorporated as the reinforcer phase (Figure 1). Opposite to alloys, in composite materials, each phase retains its chemical and physical properties. The second phase can be varied to improve the underlying properties of the matrix or provides new ones. Therefore, the overall properties of the composite are the combination of properties of the single materials functioning together as one. For instance, composites used as wear-resistance coatings [5–8] include a material harder than the matrix such as SiC,

Al_2O_3 , WC, thus providing a better resistance against wear or might include solid lubricants like PTFE, Graphite, MoS_2 , granting self-lubrication to reduce friction and anti-stick characteristics [8,9]. Additionally, the matrix alloy composition can also be adjusted to enhance the corrosion resistance of the composite [10,11].

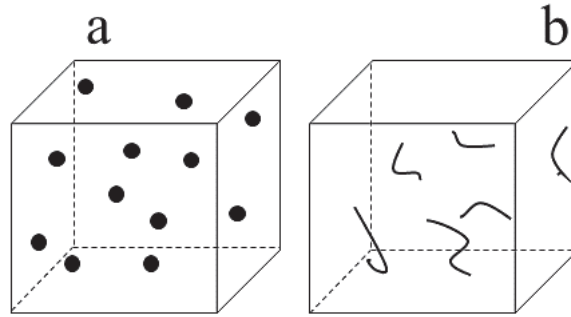


Figure 1: Composites with (a) particles or (b) fibers as reinforcer phase.

The selection of the shape and size of the reinforcer material is a key aspect to consider in the designing of composite materials. For instance, nano-sized particles can promote hardening mechanisms in the material, which are not present in composites containing micro-sized particles. Hence, in cases where the content of particles are similar, nanocomposites show higher hardness values and wear resistance than microcomposites [12–15].

1.2.1 Strengthening mechanisms in nanocomposites

The plastic deformation of a material occurs after subjecting the material to sufficient strain that no longer elastically recover. The stress-induced "plastic" flow forces a rearrangement of the microscopic structure of the material, so atoms move to a new position [16]. This mobility in the crystal structure can occur as dislocation motion. Thus, in structures where mobility is impeded due to crystal structure defects, an increase in strain is required to allow the dislocation to continue to move. Consequently, crystal defects such as interstitial atoms, other dislocations and grain boundaries increase the material's resistance to plastic deformation, therefore, increasing its yield strength and hardness [5,17]. The strengthening mechanisms which increase the strength

and hardness of metal matrix nanocomposites are summarised as follows:

Orowan strengthening: refers to the resistance of closely spaced hard particles to the passing dislocations. Particles force dislocations to bow around the particles instead of shearing through them. The strengthening effect decreases with the increase of the reinforcer size and the increase of the inter-particles spacing [18,19]. The increase in the material yield strength due to the Orowan mechanism is expressed as:

$$\Delta\sigma_{ow} = \frac{0.13G_m b}{\lambda} \ln \frac{d_p}{2b}$$

where G_m is the shear modulus of the matrix, b is the Burgers vector, d_p is the average diameter of particles, and λ is the inter-particles spacing.

Enhanced dislocation density: Dislocations interact with each other, generating stress fields in the material that can impede dislocation motion. Additionally, an entanglement of dislocations resulting from a cross of dislocations acts as pinning points that oppose dislocation motion. Therefore, conditions that promote an increase in the dislocation density increases the chance of creating pinning points.

Dislocations can result from a response to stress, for example, as the result of thermal expansion (difference in the (CTE) coefficient of thermal expansion) or elastic modulus (EM) mismatch between the matrix and reinforcement particles [20].

The strengthening by the effect of thermal mismatch is given by:

$$\Delta\sigma_{dd} = M\beta G_m b \sqrt{\rho_{CTE}}$$

where M is the Taylor factor, β is a constant in the order of 1.25, G is the shear modulus of the matrix, b is the Burgers vector, and ρ_{CTE} is the density of dislocations caused by CTE mismatch, calculated by:

$$\rho_{CTE} = \frac{A\Delta\alpha\Delta TV_p}{bd_p(1 - V_p)}$$

where A is a geometric constant related to the shape of the particles d_p is their size and V_p the volume content, $\Delta\alpha$ is the difference in the thermal expansion coefficient, and ΔT is the difference between process temperature and test temperature.

The strengthening by modulus mismatch (EM) is approximated by:

$$\Delta\sigma_{EM} = \sqrt{3}\alpha G_m b \sqrt{\rho_{EM}}$$

where α is a material-specific coefficient, G_m is the shear modulus of the matrix, b is the Burgers vector, and ρ_{EM} is the density of dislocations caused by EM mismatch estimated by:

$$\rho_{EM} = \frac{6V_p}{bd_p} \varepsilon$$

where V_p is the volume fraction of particles and d_p is their size, and ε is the bulk strain of the composite.

Load bearing effect: occurs when there is a coherent interface at an atomic level between the matrix and particles [18]. Thus, there is a shear transfer of load from the soft matrix to the hard particles. The strengthening by the load-bearing effect on the material decreases with the content of particles. In some cases, the effect is negligible due to small percentages of particles [19,20]. The increase of yield strength by the load-bearing effect can be expressed by:

$$\Delta\sigma_{load} = 0.5V_p\sigma_{ym}$$

where V_p is the volume fraction of particles, and σ_{ym} is the matrix yield strength.

Grain refinement: grain boundaries act as anchoring points impeding the propagation of dislocations. The Hall-Petch relationship establishes that in smaller grain, the yield strength, and hardness, increases because of the higher number of grain boundaries. The effect of the grain size on the strength of the material is approximated by:

$$\sigma_y = \sigma_0 + \frac{k}{\sqrt{d}}$$

where σ_0 is the resistance of the metal lattice to dislocation motion, k is a strengthening coefficient dependant on the metal, and d is the average grain size.

Second phase hardening: the addition of a second phase causes a change in the total hardness of the composite depending on the intrinsic hardness of the reinforcer and its volume fraction. The general rule of mixture of composites [2] can be adapted to calculate the theoretical hardness of the composite in relation to the reinforcer fraction:

$$H_{dispersion} = H_m(1 - V_p) + H_p(V_p)$$

where V_p is the volume fraction of the reinforcer, H_m is the hardness of the matrix, and H_p is the hardness of the reinforcer.

In electrodeposited nanocomposites, the metal matrix and the type and size of the reinforcement particles are actively chosen, and the process parameters route is designed to maximise the increase of the strengthening effects granted by the crystal structure. For instance, the process parameters: current density, agitation type and electrolyte composition are used to modify the matrix grain size [21,22]. The strengthening by particles codeposition is maximised by guaranteeing sufficient incorporation of the reinforcer particles to provide hardening. Particles should be of appropriate size and evenly distributed within the matrix to encourage Orowan strengthening. Furthermore, the enhanced dislocation density strengthening may result from crystal defects and local stresses due to local changes in the electrocrystallisation of the metal [23] or the electric field due to particles codeposition. Indeed, Stappers et al. [24] showed variations of the electric current field in the deposition of nickel-iron due to the codeposition of micro-size glass and graphite particles.

1.3 ELECTRODEPOSITION

Electrodeposition is defined as the electrochemical process where a metallic film is formed by reducing metal ions from an electrolyte onto a surface [21]. An external power supply provides an electric current flow among two electrodes: a cathode (negative) and an

anode (positive), immersed in an electrolyte containing soluble salts of the depositing metal. This technique can be used to electrodeposit nickel-based coatings, as represented in Figure 2, where the electrolyte contains nickel salts, and the surface to be plated acts as the cathode, and a soluble nickel anode dissolves, replenishing the Ni ions in the electrolyte. The cell can be adjusted based on the geometry of the substrate. For instance, in some cases, multiple anodes can be used to improve the current distribution.

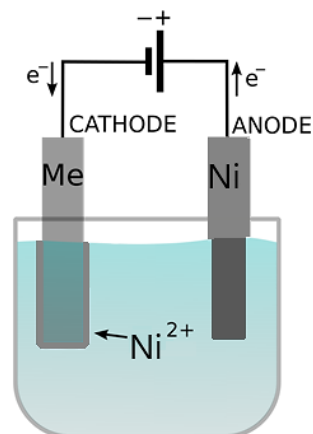


Figure 2: Electrodeposition of nickel.

1.3.1 Basic principles of electrocrystallisation and controlling parameters

Electrocrystallisation refers to the formation of the metal crystal by an electrochemical reaction. During electrodeposition, a transfer of electrons occurs through the surface of the cathode, causing the reduction of metal ions into their metallic form. This process can be divided into sequential steps [21], as shown by Figure 3: The metal ions are (1) carried to the cathode from the bulk electrolyte by mass transport through diffusion, convection and electromigration. (2) A charge transfer occurs on the cathode, and the partially reduced metal atoms are adsorbed at the surface. (3) Loosely bound adatoms will diffuse across the electrode surface to active growth sites, where they are incorporated into the crystal lattice at the kink sites or an atomic step [25]. Local stresses and defects in the microstructures, e.g. dislocations, may arise if atoms are misplaced into the crystal due to insufficient energy or time to allow atoms to diffuse along the surface to reach a kink or step site.

The growth mode of the metal also varies in relation to the presence of inhibitors. Inhibiting growth cause differences in the atom arrangement of the crystal lattice [25,26], leading to different metal microstructures. Winand [27] classified the most commonly

encountered microstructures based on the intensity of inhibition and the ratio between current density and the limiting ion concentration or current.

Figure 4 shows a schematic diagram proposed by Winand [27]. The field-oriented isolated crystals type (FI) occurs at low inhibition and under high current densities, leading to powder deposits or films with dendritic structures. The basis oriented reproduction type (BR) forms by an initial lateral growth of the film, transitioning to FI or field-oriented texture type (FT). The latter is characterised by crystals growing perpendicular to the substrate as columns. In the unoriented dispersion type, fine grains arranged randomly substitute the columns.

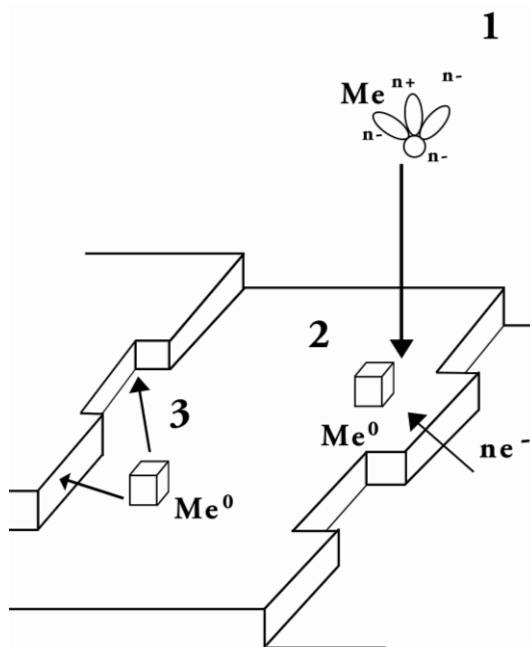


Figure 3: Schematic representation adapted from Gamburg et al. [21] of the sequential steps of an electrocrystallisation process: (1) Mass transfer of the metal ion, (2) charge transfer and partial adsorption of the adion and (3) diffusion to an active growth site.

In nickel electrocrystallisation with low or no inhibition, the adatoms are reduced and attach across the whole surface, forming isolated nuclei that grow vertically parallelly to the current lines [25] as columns. This is known as normal or non-inhibited nickel growth, and the $\langle 100 \rangle$ crystal direction dominates the growth mode [26]. In nickel electroplating, additives mixed in the electrolyte or side reactions during electrodeposition can promote inhibition or microstructural changes. Hydrogen adsorption (H_{ads}),

gaseous H_2 , and $Ni(OH)_2$ act as nickel growth inhibitors and might promote different crystal orientations instead of $\langle 100 \rangle$.

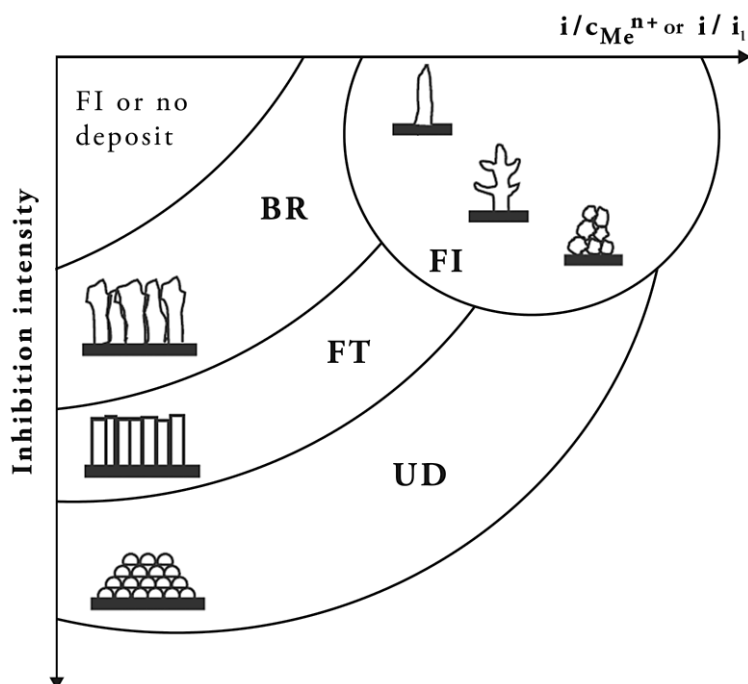


Figure 4: Diagram adapted from Winand [26], depicting different types of microstructures as function of the current density and metal ion concentration ($i/c_{Me^{n+}}$) or the diffusion limiting current (i/i_l), and the inhibition intensity.

1.3.1.1 Electrolytic bath

The electrolytic bath parameters: electrolyte composition, pH, temperature, and agitation play an active role in the metal deposition. The set-up is adjusted depending on the metal to be deposited, allowing also modifying the microstructure of the metal: grain size and shape and preferred crystal orientation [28–32].

In nickel deposition, the two most common nickel baths compositions are the Watts bath [33], based on nickel sulphate as nickel source, and the sulfamate bath, based on nickel sulfamate salts. In both cases, nickel chloride is often added to increase the conductivity of the solution and aid in the dissolution of the anode by avoiding passivation. However, high levels of chloride

concentration might affect the ductility and internal stresses of the deposit negatively. Additionally, boric acid is added as a buffering agent to limit the pH changes during electroplating due to hydrogen evolution reaction (HER).

Nickel electroplating is highly susceptible to changes in the electrolyte pH. At low pH ($\text{pH} < 3.5$ [21]), the hydrogen reduction is more intense, resulting in a decrease in current efficiency (CE) and possible hydrogenation of the deposit or the substrate. At higher pH ($\text{pH} > 5.6$ [21]), nickel hydroxides precipitate and might incorporate into the deposit, reducing its hardness and leading to a brittle layer.

The electrolyte formulation, in some cases, also includes additives. 'Brighteners' are used to assure shiny deposits, giving a uniform finer grain microstructure to the deposit [34]. Levellers act on the surface to smoothen the profile by selectively mask roughness peaks and lead more metal deposition to valleys. Other additives, such as wetting agents, facilitate the release of hydrogen bubbles clinging at the surface of the electrode formed during electrodeposition, avoiding porosity formation [35]. The electrolyte temperature can be adjusted to improve solubility and conductivity, and the bath agitation enhances the mass transport from the bulk electrolyte to the surface of the cathode [21].

1.3.1.2 Electric current

The Butler–Volmer equation [25] describes the kinetics of the electrochemical reaction by establishing that the electric current passing through the electrodes depends on the applied overpotential exponentially. Faraday's law of electrolysis [36] relates the charge, i.e. electric current and time, to the amount of deposited metal deposition. The relationship between the charge and deposited mass is described by:

$$m = \frac{QM}{nF}$$

Where m is the mass of the deposited metal, Q is the net charge applied to the cell given by the applied electric current (I) for a

specific time (t), M is the atomic weight of the deposited metal, n is the number of electrons needed to reduce the ion, and F is the Faraday constant.

In practice, other reactions happen simultaneously to the metal reduction during electrodeposition. These are referred to as side reactions. Part of the applied electric current is used in these reactions, decreasing the efficiency of the process. In the previous section, pH is highlighted for its role in nickel electroplating's side reactions. For instance, due to the hydrogen evolution reactions, the current efficiency in the electrodeposition of pure nickel from Watts baths is typically between 90 and 98% [37].

An external rectifier supplies and modulates the intensity and type of the electric current, providing control over reaction kinetic and, therefore, the microstructure of the metal [38]. The type of applied current can be modified: Direct current (DC) is the constant flow of cathodic current used to reduce ions at the cathode, pulse current (PC) alternates cathodic current (on), and zero current (off), and pulse-reverse current (PR) alternates between cathodic and anodic current by inverting the direction of the current. Each technique possesses advantages. For instance, DC benefits of shorter deposition times for the same current density average, whereas a pulsed on-off or a reverse current waveform with a high cathodic current density favours grains nuclei initiation, resulting in finer microstructures with high hardness.

Current distribution is also an important characteristic to be taken into account in electrodeposition. Current density (i) is the electric current (I) per unit area. In order to deposit a uniform coating, ideally, the current should be distributed uniformly across the cathode. In practice, the cell geometry and cathode surface heterogeneity, such as shielding, the distance between electrodes, or sharp edges, causes variations in the electric field distribution.

1.3.2 Composite electrodeposition

The electrodeposition of composite coatings is the entrapment of particles by the depositing metal (Figure 5). Different steps are

recognised: addition and dispersion of particles in the electrolyte, transport of particles to the surface of the cathode, and entrapment by the growing metal. Each of these steps involves a series of interrelated mechanisms that determine the success of particles entrapment.

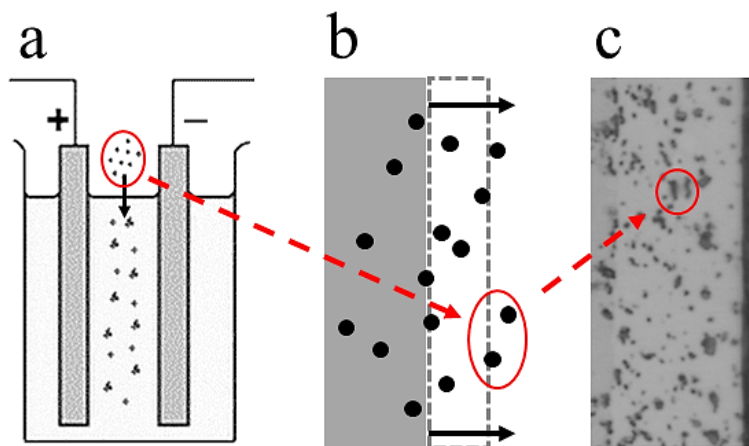


Figure 5: Electrodeposition of composites. (a) Particles addition to the electrolyte, (b) particles entrapment by the metal and (c) composite coating. Particles are encircled in red.

1.3.2.1 Interaction between particles and electrolyte

The particles-electrolyte interactions are shaped by the surface chemistry and size of the particles and the electrolyte composition and conductivity [39]. After adding the particles to the electrolyte, different interactions occur between the particles surface and the medium. For instance, depending on the particles surface charge, different ions are absorbed, surrounding the particles in an ionic cloud [40]. Also, pollutants present on the surface of the particles, e.g. partial oxidation, weakly adsorbed compounds, or manufacturing byproducts, might react and incorporate into the electrolyte. These different particles-electrolyte interactions might affect the stability of the dispersion, causing agglomerates to form, and thus, potentially affect particles codeposition negatively.

The measurements of ζ -potential values can help characterise the suspension stability of the particles [41]. The ζ -potential is the

potential at the outer Helmholtz layer of the particles ionic cloud, which varies with the ionic strength of the electrolyte, temperature, or type of ions. (Figure 6). ζ -potentials values are not measured directly but obtained by the Henry equation [41] from the electrophoretic

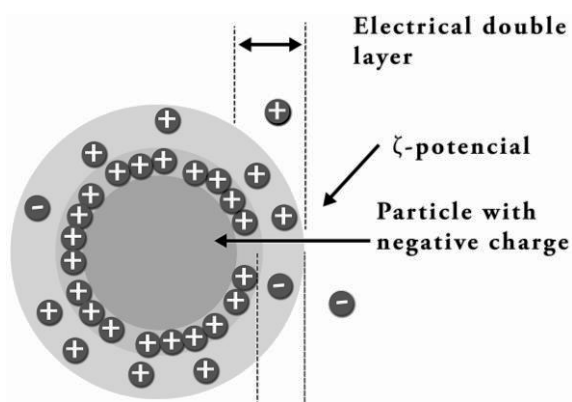


Figure 6: Representation of an ionic cloud surrounding a particle with a negative surface charge.

mobility measured by Laser Doppler Velocimetry. The technique has the limitation of requiring, in some cases, diluted solutions to take the measurements, and thus, measured values represent environments far from the working conditions.

Particles with absolute ζ -potentials values higher than 30 mV are considered as stable dispersions, while particles with lower values ($|\zeta\text{-potential}| < 30 \text{ mV}$) will tend to flocculate and sediment, requiring continuous agitation. Dynamic light scattering (DLS), i.e. illuminating the suspension with a laser, can be employed to measure the size of the agglomeration of the particles by measuring their Brownian motion [41]. The motion correlates to the particle size by the fluctuations in the scattered light's intensity. For instance, large particles move slowly, fluctuating the pattern's intensity also slowly, whereas smaller particles move quickly, and thus the fluctuation of the pattern is also quick.

ζ -potentials values require considering the measurements conditions since the values are not intrinsic to the chemistry of the particles. For instance, nano-SiC particles in nickel Watts bath showed negative ζ -potentials by previous studies [42,43], while positive ζ -potential values were reported in nickel sulfamate [44] or KCl electrolyte [45].

1.3.2.2 Effects of the agitation on particles suspension

The bath agitation plays two critical roles in the electrodeposition of composites: avoid the flocculation and sedimentation of particles, and promote their transport toward the cathodic surface.

Some of the agitation methods in composite electroplating are agitation by a pump, ultrasonic agitation and mechanical stirring. The agitation by a pump is standard on an industrial scale, but exhaustive academic research on this topic is limited. The mechanical stirring of the solution involves controlling the agitation by a rotor by adjusting the RPM of a blade, the rotation of the cathode, or a rotating magnet placed at the bottom of the cell, typically used on a laboratory scale.

The agitation can promote or even pose an obstacle to the transport of particles, affecting their codeposition rate negatively. Low stirring speeds lead to particles sedimentation, decreasing the content of the particles [46,47], while high speeds can remove particles away from the surface of the cathode before their entrapment by the growing metal, also resulting in low particles incorporation [48,49].

Ultrasonic (US) agitation is a proven method to improve particles dispersion and de-agglomeration [50]. Applying ultrasound to a liquid medium, such as the electrolyte, causes an acoustic stream that propagates through the electrolyte as a series of compression and rarefaction cycles [51]. When the ultrasonic power is sufficient, a cavity or 'bubble' may form during the rarefaction cycle [52], which break the weak van der Waals forces dispersing and deagglomerating the particles [50]. Parameters such as ultrasonic power and frequency can be adjusted to improve particles de-agglomeration while affecting their incorporation rate [53–56]. High US power might hinder codeposition due to a bouncing-back effect, in which the vibrating cathode pushes away particles as they approach its surface [57,58]. While low-frequency US (20 kHz) shows high and better-dispersed particles content compared to high frequencies (850 kHz) [59] because of more extended periods to cause cavitation effectively. US agitation has also shown grain refinements effects in metal electrocrystallisation [60].

1.3.2.3 Influence of the electric current in particles codeposition

Composites coatings can be produced by different galvanostatic techniques using: direct current (DC), pulse current (PC) or pulse-reverse current (PR). These methods directly influence the metal electrocrystallisation, affecting the particles codeposition [9,61] by modifying the metal deposition rate, thus the entrapment of particles, and by affecting particles electrophoresis. Particles can also influence the current distribution, affecting the metal electrocrystallisation. For instance, conductive particles might cause dendritic growth and porosity in the metal deposit [62,63].

The direct current deposition is the most commonly used technique to obtain composites. However, there is disagreement about the role of the current density in the particles codeposition. In some studies, the high current density is associated with a decrease in particles content [12,64], while in others, an increase is reported [65,66]. The literature shows improvements in the codeposition if PC or PR are used instead of DC [67–72]. However, the benefits of pulse plating over direct current in particles codeposition are also controversial.

In pulse-reverse plating, a particular line of research showed that plating and stripping times could be modulated based on the particles size to improve the codeposition rate. Podlaha et al. [73] reported a noticeable increase in particles content after plating under pulse-reverse a metal thickness similar to the particles average diameter in each cathodic period. Similarly, Xiong-Skiba et al. [74] achieved a high nanoparticle content (up to ~ 23 wt%) by plating a metal thickness N times the particles average diameter in each successive cathodic cycle and stripping the metal $N-1$ times.

1.3.2.4 Prediction models for particles codeposition

Different models have been developed in the last decades [9,61] to explain the mechanisms that govern particles codeposition and predict their incorporation rate based on the parameters of the process. Table 1 provides a summary of the existing models and their main assumptions.

Table 1: List of theoretical models that describe the mechanisms of particles codeposition in composite electroplating, adapted from Low et al. [9].

Guglielmi [75]	This model described codeposition as two consecutive steps: (i) adsorption, where a layer of loosely absorbed particles is built at the cathode's surface, and (ii) electrophoresis, where the electric field at the interface promotes strong surface adsorption, and thus particles are entrapped by the growing metal. The fluid dynamics conditions were not considered.
Celis et al. [76]	Celis et al. proposed that particles transport is proportional to the mass transport of ions toward the cathode. Firstly, an adsorbed layer of ionic species is built around the particles after their addition to the plating solution, followed by particles transport by convection-diffusion. Finally, incorporation depends on the probability and number of transported particles.
Fransaer et al. [77]	This model used trajectory analysis to describe the favourable conditions given by the tangential forces acting on the particles to improve codeposition rate.
Hwang et al. [78]	Hwang et al. emphasised on the role of the current density in particles codeposition. Codeposition rates are correlated to the reduction of the ions adsorbed at the surface of the particles.

Table 1 (continued): List of theoretical models that describe the mechanisms of particles codeposition in composite electroplating, adapted from Low et al. [9].

Vereecken et al. [79]	The model described the transport of particles as controlled by convection-diffusion, considering as well hydrodynamics and assumed that particles incorporation increases by residence time at the cathode's surface.
Berçot et al. [80]	This model improved Guglielmi's model by incorporating a mathematical model accounting for hydrodynamic conditions.

The main element to consider from these models is their restriction to specific conditions, limiting their validity outside the constraints of the experimental set-up. Thus, none of these models is sufficient to provide control or predict particles codeposition, and further work is required on the topic.

1.4 STATE OF THE ART

1.4.1 Gap between previous research and the present study

There is a great interest in the transition from micro-sized reinforcement particles to nano-sized ones to produce composite coatings. Thanks to their nanometric size, nanopowder can promote additional strengthening effects in the matrix not present in microcomposites. For wear-resistance coatings, nanoparticles are preferable over the larger hard particles as, in some cases, they can lead to third-body abrasive wear when breaking loose. Additionally, manufacturers aim for cost-effective production methods, i.e., shorter production times or less material and smaller sizes. Hence, the protection of the surface requires thinner coatings, limiting the size of the reinforcer phase.

The literature presented in this section shows that the electrodeposition of nanocomposites is a complex system with

multiple correlations between parameters that synergise or antagonise with particles codeposition. Even under laboratory conditions, reproducibility and predictability in the content of nanoparticles are not achievable with the current state-of-the-art knowledge. This leads to a lack of reliability and robustness and limits the industrial applicability of electrodeposited nanocomposites.

Nickel electroplating is a technologically ready and mature process that provides a solid platform for studying nickel-based nanocomposites, thanks to decades of research and sound data on the electrocrystallisation of pure metal. Early studies focused on comparing electroplated composites to pure nickel and define the synergies between codeposition and electrocrystallisation. Later studies recognised this was insufficient since particles codeposition is also affected by the electrodeposition parameters. Hence, successive research focused on variable correlation and defining the mechanisms that rule over particles transport and codeposition. However, the work is unfinished.

The theoretical models to predict particles codeposition, introduced in the previous section (Table 1), are only valid in laboratory conditions due to intercorrelated process variables. Furthermore, only the models proposed by Verecken et al. [79] and Berçot et al. [80] were built considering submicron-size particles, while the rest of the models considered micro-particles. Therefore, the generalisation of the identified mechanisms in nanoparticles codeposition to current studies is limited. The process is virtually new when multiple parameters are modified. For this reason, the present research carries out the electrodeposition in a simple electrochemical environment, facilitating a better study of single aspects of the electroplating process. The research aims to fill the knowledge gap and better understand what parameters control the codeposition of particles, leading to more reproducible results and identifying the codeposition synergies.

The interaction between particles and electrolyte has a significant effect on codeposition [81–85]. These interactions are often characterised by ζ -potentials values and correlated to particles

content. However, the research perspective is generally placed on the role of the electrolyte and not at the particles surface state, which is often underestimated or unknown. Differences in the particles surface state, even in particles with the same chemistry, might affect the particles codeposition and lead to unreliability in the production when the process uses particles from different batches or suppliers. The present study examines the correlation between codeposition and the particles surface state and investigates how to provide control to the process by a novel powder surface treatment.

Wear resistance composites require a rich and controlled codeposition of hard particles because of their hardening effect on the material. Pulse plating is a promising technology capable of increasing the content of the particles compared to direct current plating [86–88] if properly designed. Although the work of Podlaha et al. [73] and Xiong-Skiba et al. [74] showed promising results, increasing nanoparticles content up to 23 wt.%, their research was not further developed in the last decades. The present study examines a novel design of a pulse-reverse waveform adapted to the particles average size inspired in their work. The research highlights the effects of the design of the waveform in particles codeposition, specifically the roles of the electric current intensity and length of the anodic pulse. Since the proposed technique requires extensive anodic time to strip the equivalent thickness of the particles average diameter, increasing The risk of electrode passivation increases considerably. A new approach is examined to prevent electrode passivation by incorporating a train of short anodic pulses during the reverse cycle. The design of the pulsed anodic train, inspired by Aroyo et al. [89], has never been employed before in composite electrodeposition by pulse-reverse deposition.

The present study also deepens the understanding of the effect of particles in metal electrocrystallisation. Particles alone can modify the deposit microstructure [90–93] and alter the preferential crystal growth [67,86,91], and although these aspects have been considered in previous studies, the particles codeposition role in metal crystallisation requires further analysis. As mentioned in the

previous section, different process parameters, other than the particles, can cause changes in the metal electrocrystallisation. Therefore, it is critical to study electrocrystallisation and particles codeposition without the influence of additional parameters. The electrodeposition is carried out on a pure nickel bath with simple chemistry under the same electroplating conditions, so variations in the metal correlate directly to the particles codeposition. This research implements a comprehensive analysis of the relations between particles codeposition, electrocrystallisation and strengthening mechanisms since both reinforcing particles and nickel microstructure influence the mechanical properties of the composite coating.

The strengthening mechanisms present in electrodeposited nanocomposite coatings and their magnitude differ partially from nanocomposites produced by other manufacturing methods. The study of the strengthening effects requires considering that metal crystallisation is driven by electric current and not by solidification and that nucleation only occurs at the surface of the cathode surface. Furthermore, in electrocodeposition, particles incorporation is carried out by engulfing the particles by metal growth, and particles do not act as inoculants in the liquid. The present work studies the strengthening mechanisms present in electrodeposited nanocomposites using quantitative data and empirical relations to identify the hardening effect granted by particles codeposition, metal microstructure, and the synergism between particles and metal.

The present work also studies the relationships between the hardening effects present in nanocomposites and their wear behaviour. The surface protection against wear by novel multi-material coatings is studied, in addition to the traditional single powder composites. This study complements the very few studies available from the literature where dual composites based on hard particles and self-lubricants showed an outstanding performance compared to the single-particle systems [94–96]. The present study aims to extend the knowledge on the topic.

RESEARCH OBJECTIVE

CHAPTER INTRODUCTION

This chapter describes the research objective of this thesis. The purpose and aim of the work are described and connected to the research questions.

2.1 PURPOSE AND AIM

The surface of the material endures the conditions of the environment during use. In aggressive environments, the surface might deteriorate over time due to wear or corrosion leading to the failure of the bulk material, jeopardising the service life of the component. Electrodeposited composite coatings are designed to avoid deterioration by providing specific functionalities to the surface, depending on the future application of the component.

The design of the electrodeposition process and the type of reinforcement define the metal microstructure and the successful incorporation of the reinforcer phase. The combination of these two elements, matrix and particles, govern the performance of the material. At present, the effects of the process parameters on particles codeposition are not fully understood. This leads to uncertainty in the final microstructure of the coating and low reproducibility concerning the particles incorporation rate. Therefore, the performance of the surface cannot be predicted or controlled.

The purpose of this thesis is to provide a better understanding of the mechanisms of particles incorporation and the resulting strengthening mechanisms in electrodeposited nanocomposites. This thesis aims to explore means to improve the control of particles codeposition by studying the particles surface state and

providing tools to control its impact on the codeposition. Moreover, a novel current waveform is studied as a mean to improve SiC codeposition. Additionally, the synergistic effect of particles codeposition in the electrocrystallisation of metals is examined and linked to the strengthening mechanisms. To conclude, the wear resistance provided by a novel dual composite where hard carbides and self-lubricant particles are combined is studied. The wear behaviour of the dual and single powder composites is compared and related to the metal microstructure and particles codeposition.

2.2 RESEARCH DESIGN

2.2.1 Research perspective

In this thesis, the experimental research was designed as true experimental. The hypotheses were tested by the method involving cause-and-effect relationships [97]. The definition of hypotheses was based on the observation and collection of quantitative data provided by the experiments. Deductive reasoning, supported by general principles, was used to test hypotheses in specific circumstances. Hypotheses were validated or refuted based on the empirical evidence. The experimental variables were narrowed based on the literature review or previous work. In this thesis, typical experimental techniques adopted among the research community were identified and used, permitting the generalisation of research findings.

2.2.2 Research questions

When electrodeposited nanocomposites properties are compared across literature results, the lack of control in the production process is evident. Currently, no deposition technique allows a controlled production of nanocomposites, which evidently is the target goal of any industrial process. Therefore, the knowledge of the influence of the process parameters on particles codeposition and how particles content relates to the mechanical properties is crucial.

Based on the literature review, the following observations are made:

(i) Particles codeposition is affected differently by the multiple input parameters, which in some cases are not fully defined. Most studies neglect the impact of the particles surface state, receiving minor considerations or treated as uncontrolled. Research must consider the role of the particles surface state as a critical and relevant aspect to study in particles codeposition.

(ii) The concept of a pulse-reverse waveform based on the particles size to improve the particles incorporation rate requires further development due to the reduced number of publications on this topic. Moreover, parametric studies of the design of the waveform and its impact on particles codeposition should be performed.

(iii) The study of the strengthening mechanisms in electrodeposited nanocomposites is limited because of the high dependency between process parameters and particles codeposition, complicating a comprehensive study of the metal electrocrystallisation. The strengthening mechanisms must be studied first as single instances identifying the governing factors and then as an accumulate that defines the mechanical properties of the composite.

Four research questions are formulated to tackle the identified knowledge gap and satisfy the purpose and aim of the research:

- RQ1:** What are the particles-electrolyte interactions and their effect on the electrodeposition, and how can these effects be controlled?
- RQ2:** What variations in the deposition parameters will improve the control of the particles codeposition process?
- RQ3:** What is the role of particles with different chemistry, size, content and dispersion in the electrocrystallisation of nickel?
- RQ4:** What is the relationship between codeposition, strengthening mechanisms and wear behaviour on Ni-based composites?

RESEARCH APPROACH

CHAPTER INTRODUCTION

This chapter describes the research approach and strategy used in this work to answer the research questions. The research design is firstly described, followed by a description of the materials, experimental procedures, and characterisation techniques.

3.1 RESEARCH STRATEGY AND METHODOLOGY

3.1.1 Research strategy

The principal objective of this thesis is to explore causal links between process parameters, codeposition, microstructure, and mechanical properties. The process variables such as temperature, pH, the cathode and anode materials and geometry, and the electrolyte composition are kept constant to reduce the number of dependencies between parameters.

A bath with basic chemistry, constituted by one or two metal salts, reduces the correlations between variables and simplifies the examination of the synergies between codeposition and electrolyte. Therefore, a single metal (nickel) additive-free bath is chosen to deposit pure nickel as the matrix. The electrolyte formulation is maintained fixed, so the conductivity and concentration of ions are constant for all the experiments. Furthermore, the same area is selected on all samples for analyses and testing, thus minimising the variations due to fluid dynamics or current distribution.

The particles-electrolyte interactions are characterised to determine their impact on the codeposition of particles. The purpose of Supplement I is to characterise the behaviour of as-

produced particles in the electrolyte by ζ -potential measurements and titration. The supplement suggests the application of a powder pre-treatment aimed to bring the particles to a similar surface state. The pre-treatment removes the variable that the particles surface state represents, hence addressing RQ1. Supplement III analyses by ζ -potentials the effect of adding a surfactant (SDS) in the electrolyte, studying how an additive typically used in industrial baths affects the particles-electrolyte interactions, also addressing RQ1.

The control of the particles content in electrodeposited composites is the foundation of a potential industrial process, and thus, it is the main research interest of RQ2. Supplement I analyses the capability of a powder surface treatment to grant reproducibility independently of the particles production route, supplier or the impurity residuals from production that can vary from batch to batch. Supplement II studies the potential of improving the particles codeposition rate by adjusting a pulse-reverse waveform adapted to deposit a metal thickness equivalent to the particles average diameter during the cathodic pulse and strip half of the thickness during the anodic pulse, addressing RQ2. Supplement III tests the deposition technique suggested in Supplement II, thereby studying the control over the particles codeposition rate by modifying the design of the waveform, also referring to RQ2.

Supplements I, II, IV, V and VI address RQ3 by comparing the metal microstructure of samples with different particles sizes, volume content and dispersion. Supplement I covers the codeposition of SiC particles with different sizes under the same current density. In Supplement II SiC particles with the same sizes are codeposited by varying the current type and intensity of the process. In Supplement IV, the US agitation is used to promote the dispersion of particles of different sizes. Supplements V and VI present the combination of particles with different chemistry: graphite and MoS₂, to define their impact on the metal microstructure and propose the production of dual composite coatings. In particular, Supplement VI studies the exceptional tribological properties of dual SiC:MoS₂ nanocomposite as a result of the combination of the particles and their effect on the Ni microstructure.

In Supplement VII, all samples produced for Supplements I, II, IV, V and VI are analysed by tribological tests to study the relationship between SiC volume content, material microhardness and wear behaviour. Additionally, Supplement VII studies in detail the strengthening caused by particles codeposition, addressing RQ4. Figure 7 summarises the connection between the research questions studied in this thesis and the appended supplements.

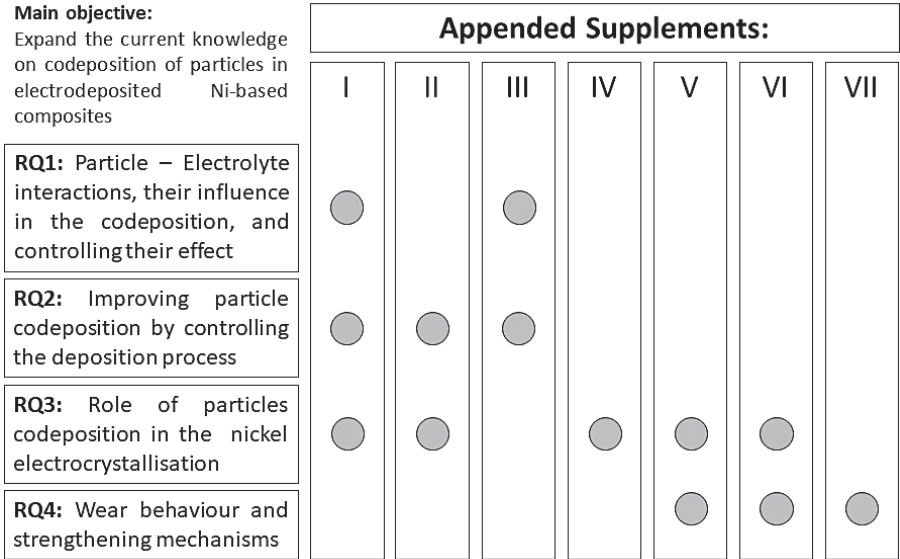


Figure 7: Schematics of the research strategy and the connection between research questions and supplements.

3.1.2 Research ethics and quality assurance

The reproducibility of the research data was verified by replicating the characterisation on multiple samples, taken randomly, and produced under the same conditions. The reliability was increased by gathering data consistently in the same area of the specimens across all samples to assure minimal variation in critical parameters. Each sample was marked and registered in full detail, updating the experimental journal to track the source of unforeseen changes in the standard conditions. The validity of the research was ensured by characterising all samples following standardised methodology. When available, the results were

compared to previous studies. A high degree of consistency in the production of samples was achieved by maintaining the same manufacturer for each of the electrodeposition materials. The studies presented in this work were done with no conflict of interest.

3.2 MATERIALS AND EXPERIMENTAL PROCEDURE

In order to allow the comparison between results from each supplement, some of the process parameters remained constant across the different sets of electrodeposition experiment.

The electrodeposition was performed in a thermally controlled cell at 45 °C and with a constant pH of 3.0. The pH of the plating solution was stabilised before each electrodeposition by adding H₂SO₄ or NaOH. The configuration of the electrodes was in parallel vertical, where the cathode was a low carbon steel plate and the anode a nickel sheet with 99.9% of purity. Before electroplating, the substrates were mechanically ground with SiC grade #1000, cleaned ultrasonically in a diluted 5% degreaser (TICKOPUR R 33; DR H STAMM GmbH) and activated by pickling for 8 min in 2.5 M H₂SO₄.

3.2.1 Materials

3.2.1.1 Nickel electrolyte

The electrolyte formulation of this thesis was based on a Watts bath [33]. The composition, pH and temperature of the solution remain fixed in all depositions. The electrolyte is varied only in Supplement III by adding sodium dodecyl sulfate (SDS). The deposition bath composition and parameters are listed in Table 2.

Table 2: Electrolyte composition and parameters.

NiSO ₄ ·7H ₂ O	240 g L ⁻¹	SDS (Sodium dodecyl sulfate)	0.4 g L ⁻¹ in Supplement III only
NiCl ₂ ·6H ₂ O	45 g L ⁻¹	pH	3.0
H ₃ BO ₃	30 g L ⁻¹	Temperature	45 °C

3.2.1.2 Particles

The experimental work used different particles in the production of composite coatings:

- SiC powder of 50 nm size particles (gnm© #SiC-110 spherical β-SiC)
- SiC powder of 60 nm size particles (Iolitec GmbH #NC-0002 spherical β-SiC)
- SiC powder of 500 nm size particles (gnm© #SiC-110 irregular angular-shaped β-SiC)
- Graphite powder of 400 nm size particles (Iolitec GmbH #CP-0019 irregular angular-shaped Graphite)
- MoS₂ powder of 90 nm size particles (Iolitec GmbH #NC-0017 spherical MoS₂)

Supplement I includes the analysis of composites containing 300 nm size SiC particles (ESK-SiC GmbH. NF25 spherical β-SiC), while Supplement IV studies 5 μm size SiC particles (H.C.Starck© SiC grade UF-05 α-SiC). The results from these studies are not included in the discussion section of this thesis, and their complete study can be examined in the appended papers.

Supplements V and VI consist of a study of dual composites containing a dispersion mix of particles with a ratio of 10:10 g L⁻¹. In these supplements, the single powder composites were produced from a 10 g L⁻¹ powder load. Hereinafter, "10 g L⁻¹" is included in the sample name to refer to this condition. The samples produced with a 20 g L⁻¹ load do not include any remark.

Table 3 shows the variation of particles type and average size in each supplement.

Table 3: Particles type, mean size and concentration of the composite coatings.

Supplement	Particles	Average size (nm)	Concentration(gL ⁻¹)
I	SiC, SiC(ST)	50, 60, 500	20
II, III	SiC	60	20
IV	SiC	50, 500	20
V	SiC, Graphite	60, 400	10:0, 0:10, 10:10
VI	SiC, MoS ₂	60, 90	10:0, 0:10, 10:10
VII	SiC	50, 60, 500	10, 20

The bath suspension was continuously stirred mechanically with a magnet, and additionally, ultrasounds (Hielscher, 24 kHz, 0.087 W cm⁻³) were applied for 30 minutes before electroplating for deagglomerating the particles.

3.2.1.3 Pre-treatment of particles

Supplement I applies a surface treatment (ST) based on nitric acid (described in detail in Supplement I – Table II) to the particles: SiC 50, 60 and 500 nm. Hereinafter, "ST" is included in the name of the samples produced from surface-treated particles. The as-produced particles do not include any remark.

The surface treatment was prepared by adding 20 g L⁻¹ of SiC into 1 L of distilled water and stirred (200 RPM) for 30 min. The suspension was filtered by MUNKTELL© analytical filter paper (Quality 00H, ash content 0.007%), maintaining at least 100 mL of suspension to avoid particles agglomeration. The suspension volume was set to 1 L, and 20 mL L⁻¹ nitric acid (65%) were added

and stirred for 15 min. The suspension was again filtered and rinsed with distilled water until it reached a pH of 6.0.

After the final rinsing step, the deposition bath (described in Table 2) was prepared immediately in the H₂O-SiC/ST suspension to avoid the drying and agglomeration of the particles. The solution was agitated by ultrasound (Hielscher, 24 kHz, 0.087 W cm⁻³) for one hour, and the pH adjusted afterwards to 3.0.

3.2.2 Electrodeposition parameters and set-up

3.2.2.1 Electrolytic cell

The electrodeposition in all supplements was carried out in a 500 mL volume electrolyte, except for Supplement III, where the plating bath volume was 2 L. In the 500 mL cell configuration (Figure 8), the cathode area was 0.15 dm², and the distance between electrodes was 7 cm. The US horn, immersed in the electrolyte, was positioned 2 cm above the cathodic surface to avoid shielding the cathode during electrodeposition. In the 2 L cell, the cathode surface was 0.25 dm², and the separation between electrodes was 12 cm. Hereinafter, the samples produced in the 2 L cell includes the "2L" in their name, whereas the rest, produced in the 500 mL cell, do not have any remarks.

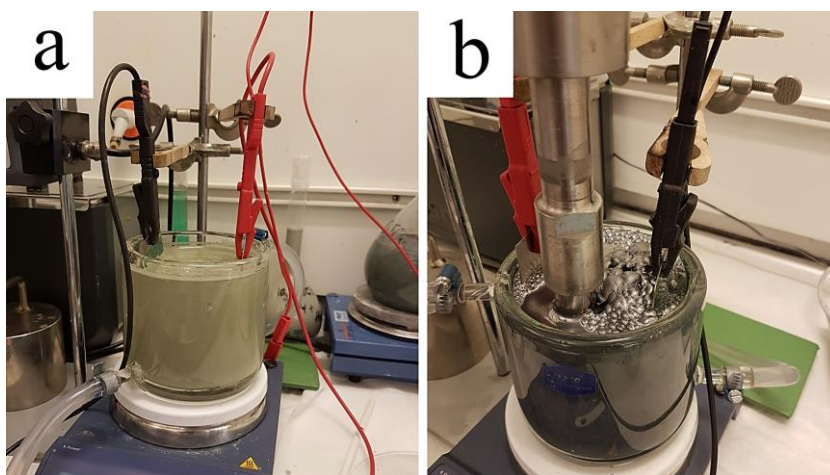


Figure 8: Electrodeposition in a 500 mL volume bath of (a) Ni-SiC50 under magnetic stirring and (b) Ni-MoS₂ under ultrasonic agitation.

3.2.2.2 Electric current

Table 4 shows the different electric current type and intensity used in the experimental work.

Table 4: Electrodeposition current control conditions.

Supplement	Electric current type	DC density (A dm ⁻²)	PR waveform
I, IV, V, VII	direct current (DC)	4	-
II, VII	direct current (DC) and pulse-reverse (PR)	4; 10	Adapted to SiC50
III	pulse-reverse (PR)	-	Adapted to SiC60
VI	direct current (DC)	2.33; 4	-

In Supplements II and III, the pulse-reverse waveform was adapted to deposit a metal thickness equivalent to the particles average diameter (50 or 60 nm) during the cathodic pulse and strip half of the thickness during the anodic pulse (1D-1/2D, Figure 9). In Supplement III, the pulse reverse waveform (PR) was modified, maintaining the same design of 1D-1/2D, and therefore the same charge by modifying the shape of the anodic pulse: increasing the anodic current density during the anodic cycle (PR_{hia}) or increasing the total anodic cycle time (PR_{hat}). The waveforms are depicted in Figure 10 and described in detail in Supplement III.

The studies of high-frequency PR deposition (500 Hz, $i_c = 10$ A dm⁻² and $i_a = 4$ A dm⁻²), described in Supplement II, are briefly discussed in the results and discussion section below. Hereinafter, "PR-HF" is included in the name of the samples produced under the high-frequency PR waveform. In the present work, nanocomposites were also produced by pulse on-off (PP_{on-off}) plating, where the cathodic peak current density of the PP_{on-off} waveform was equal to 10 A dm⁻², and the average current density of the pulse was 4 A dm⁻².

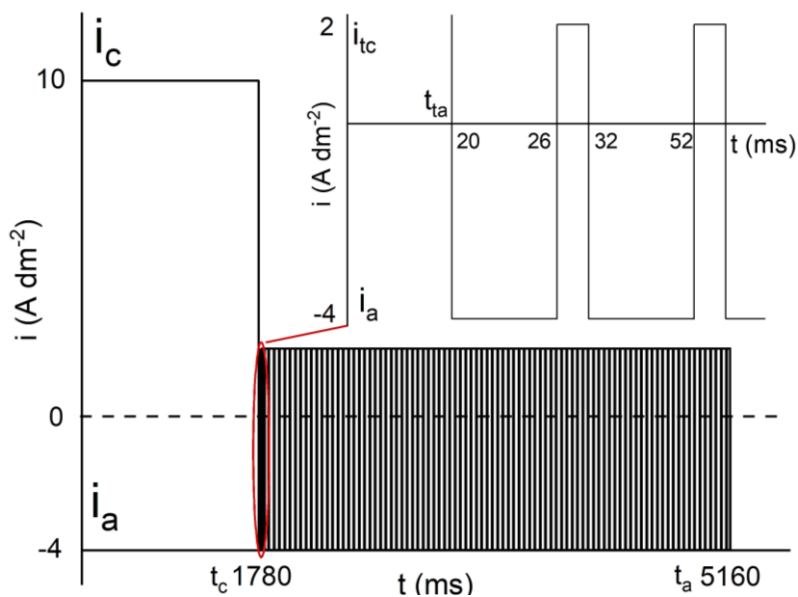


Figure 9: 1D-1/2D pulse-reverse waveform adapted to the average diameter of the particles (60 nm).

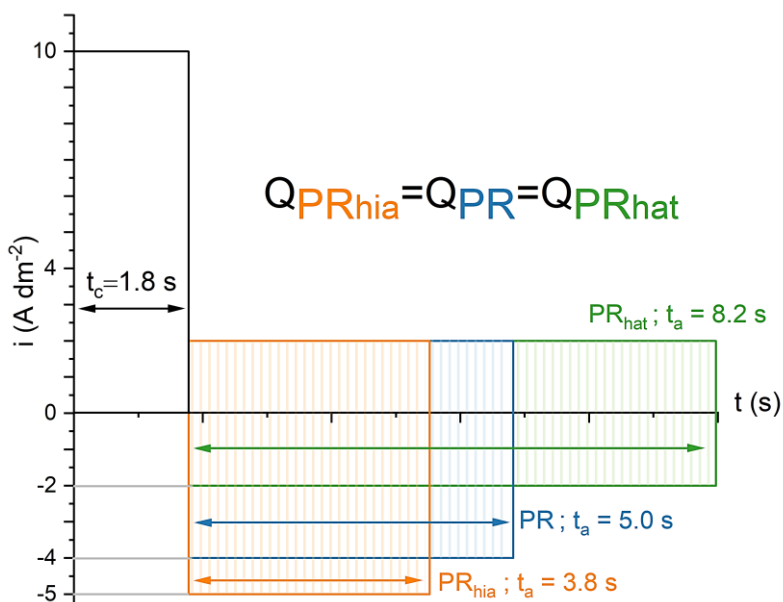


Figure 10: Scheme of 1D-1/2D pulse-reverse waveforms with different anodic cycles adapted to the average diameter of the particles (60 nm).

Supplement VI introduces a pre-study aimed to optimise the efficiency of the electrodeposition of dual composites containing SiC and MoS₂. As a result, the current density used in the deposition of dual SiC:MoS₂ nanocomposites was modified to 2.33 A dm⁻². The appended paper describes the pre-study in detail.

The electrodeposition for all the experiments performed in this thesis was designed to maintain an equal process net charge (≈ 1800 C) to deposit the same amount of metal and prevent differences between the performances of the sample related to thickness variation.

3.2.2.3 Agitation mode

Two modes of agitation were used in the experimental work: Stirring at 200 RPM by a cylindric-shaped rotating magnet (0.7 cm diameter and 6 cm in length) placed on the bottom of the cell, and agitation by an ultrasonic (US) horn immersed in the bath (Hielscher, 24 kHz, 0.087 W cm⁻³).

Supplements I to V and VII report the electrodeposition under stirring, while Supplement IV under US agitation. The US power was measured by a multimeter connected to the device. Hereinafter, "US" is included in the name of the samples produced under US agitation, whereas the rest do not include any remark.

3.3 CHARACTERISATION AND TESTING

The current efficiency (CE) of the deposition was calculated as the ratio between the deposited mass minus the particles mass and the theoretical deposited mass as predicted by Faraday's law. The variation in pH (Δ pH) of the electrolyte was measured by comparing the pH after deposition to the initial pH. The average thickness of the coating was approximated considering nickel's density (8.91 g cm⁻³) and the deposited mass.

3.3.1 Sample preparation

The samples were marked according to their production condition and sectioned in a squared shape. Only the specimens located in the middle of the coating were selected for analysis, as depicted by the red-coloured sections in Figure 11a, to avoid areas affected by the higher current density concentrated at the edges of the samples.

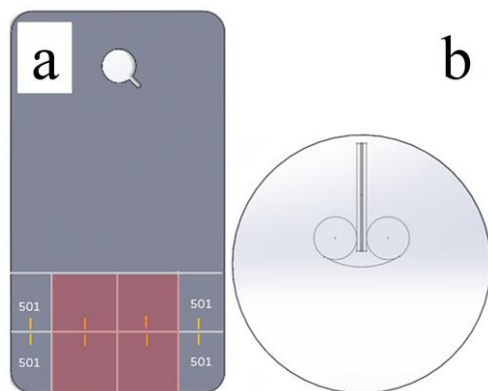


Figure 11: (a) Cutting of samples, red-coloured squares show the selection for analysis, (b) Sample mounting for cross-section analysis.

For the cross-section analysis, the samples were mounted in PolyFast conductive resin (Struers®), as shown in Figure 11b. The yellow marks located in the centre of the square (Figure 11a) represent the interest area where the cross-section analysis was carried out.

The mounted samples were ground with SiC papers of different granulometry from grit size of P800 (FEPA) to P4000 (FEPA) and gradually polished mechanically with different synthetic clothes with diamond particles suspension of 3 and 0.5 μm .

3.3.2 Characterisation of particles in suspension

3.3.2.1 Potentiodynamic cathodic polarisation test

Supplement IV reports potentiodynamic polarisation curves to compare the hydrogen evolution reaction (HER) in the absence or presence of SiC50 or SiC500 particles. The polarisation tests were

recorded under the same conditions as the electrodeposition bath (pH, temperature, conductivity, electrode geometry) without the metal salts. The polarisation was applied from OCP to cathodic overvoltage equivalent to a current density of 5 A dm^{-2} . An Ag/AgCl (3M KCl) electrode was used as the reference electrode and a platinum electrode as the counter electrode, while the working electrode was the same steel substrate used in the deposition. An IVIUM Vertex potentiostat was used for the electrochemical measurements, and the sweep rate was set as 2 mV s^{-1} .

3.3.2.2 Particles size in suspension, ζ -Potential measurements and Titration

The particles agglomeration size of SiC50 and 500 nm, and the ζ -potentials of the particles: SiC 50, 60 and 500 nm were determined by Zetasizer Nano ZS (Malvern Instruments, Herrenberg). In order to guarantee values close to the electrodeposition conditions, the measurements were taken in a diluted (25%) additive-free Watts electrolyte (included in Supplement I) and after SDS addition (included in Supplement III), with a concentration of 0.2 g L^{-1} SiC at pH 3.0 and a temperature of 45°C .

The refraction index of the particles was set to 2.610 and the electrolyte adsorption to 0.900. The pH was adjusted by H_2SO_4 or NaOH, and the dispersion was kept in continuous agitation and US for five minutes before measurements. The size and ζ -potentials of the particles were expressed as the average value of three different sets of ten measurements.

The buffering capacity of SiC 50, 60 and 500 nm particles was studied in Supplement I. Firstly, 20 g L^{-1} of particles were added to distilled water (60 mL) and the pH after stabilisation was recorded. Secondly, the pH was adjusted to 3.0 by HCl, and lastly, the titration was carried out with NaOH 0.01M as titrator. Since the pH was expected to increase during electrodeposition due to the hydrogen reduction on the cathode surface [26]. The titration was done only toward alkalisation.

3.3.3 Imaging techniques

3.3.3.1 Microscopy

All the scanning electron microscopy (SEM, JEOL 7001F and TESCAN Lyra 3) analyses were carried out under the same conditions for all the samples. The observation of the samples was done at the surface and the cross-section. A selection of the images taken during these analyses is included in this thesis.

jViewer image analyser was used to measure particle size and the inter-particles distance, centre to centre, between neighbouring particles in selected samples. The analysis was carried out in two images under two magnifications (18.5 kx and 138 kx).

The samples in Supplement VI were prepared for cross-sectional scanning transmission electron microscopy (STEM) by conventional mechanical polishing and Ar-ion milling methods. STEM was carried out using a Tecnai G2 TF20 UT electron microscope, operated at 200 kV. Images were acquired in STEM mode using a high-angle annular dark-field (HAADF) detector.

The coatings were analysed in cross-section by electron backscattered diffraction (EBSD, EDAX-TSL). The diffraction of electrons forms Kikuchi bands into a phosphor screen corresponding to the diffracting lattice crystal planes [98]. The technique was used to define and draw maps of the samples grain size and shape, and grain orientation, as illustrated in Figure 12. The grain area maps (Figure 12a) uses colour codes to paint grains according to their areas, allowing a visual comparison of the grain sizes. The orientation map (Figure 12b) uses the colour codes to picture the crystal growth orientation. Whereas the inverse pole figures (Figure 12c) determined how textured the deposits are by measuring the max texture intensity in units of multiplies of random distribution (mrd).

The measurements were performed with an electron probe current ranging from 4 to 5 nA at an acceleration voltage of 15 kV. The EBSD maps were built for two samples for each plating condition with a step size of 80 nm. The analysed was done by OIM 5TM software in

the growth direction (perpendicular to the cross-section). Regions consisting of at least three similarly oriented connected points with a misorientation $<10^\circ$ were defined as grains. Their size was calculated by the number of points contained in the region, disregarding the data with a confidence index (CI) of <0.1 . Twin boundaries were excluded from these calculations. The impact of the anisotropic grain morphology of the microstructure on the grain size average was minimised by weighting the value of the area fraction of each grain. The average grain diameter was extrapolated by considering the grain as a circle. In reality, the shape of the grain in uninhibited electrodeposited nickel is elongated columns, while in large grains, the approximation deviates, in the smaller grains, as the result of grain refinement and in the scope of this research, the grains shape is closer to the hypothesis.

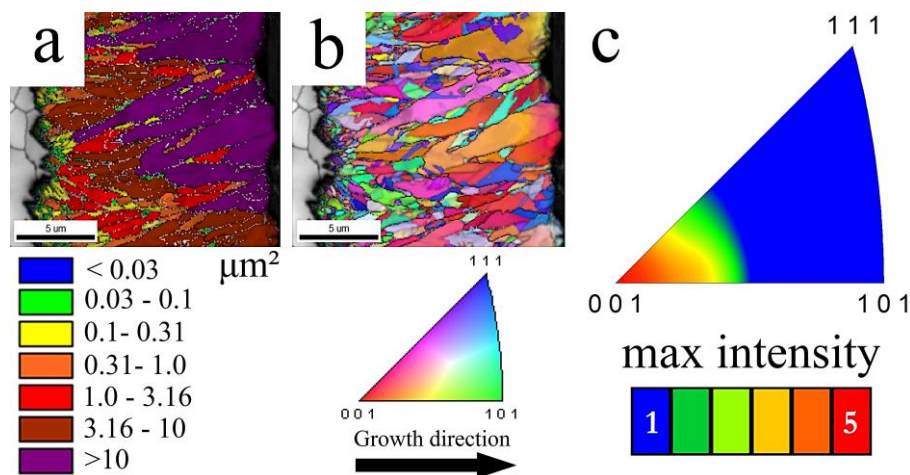


Figure 12: (a) Grain area (μm^2) map, including ranges of grain sizes as indicated by the colour bar, (b) Grain orientation map colour-coded in relation to the electrodeposits growth direction, shown by an arrow in the legend, (c) Inverse pole figure including the max texture intensity in units of multiplies of random distribution (mrd) as indicated by the colour bar.

3.3.4 Non-Imaging techniques

3.3.4.1 Chemical composition by Wavelength-dispersive X-ray spectroscopy (WDS)

Scanning electron microscopes can generate different types of signals. One of these is X-rays, emitted and collected after the interaction between the electron beam and the sample. These X-ray signals can be used for chemical composition analysis. The number and energy of the emitted X-rays were measured and matched to a chemical element. Wavelength-dispersive X-ray spectroscopy (WDS) allows reading a specific X-rays spectrum, permitting chemical analysis with high precision for light elements, such as Si, or low content. Therefore, WDS was preferred over other chemical analysis techniques.

The weight percentage of Si, Mo and C were calculated based on their pure standards. The standards and sample analyses were performed using an acceleration voltage of 10 kV and a beam current ranging from 13 to 20 nA. In Supplements I to VI, the SiC volume content was calculated starting from Si wt% data and assuming the particles to be stoichiometric and with a density of 3.22 g cm^{-3} . In Supplement V, the graphite volume content was calculated from C data and considering 2.23 g cm^{-3} as the particles density. In the case of the dual composite, the graphite content was calculated from the C wt% data, minus the C weight content of SiC. The elemental analysis of carbon was considered an estimation of the actual content because of the low accuracy of the analysis due to its low atomic number and abundance. In Supplement VI, the molybdenum disulfide content was calculated starting from Mo data and assuming the particles to be stoichiometric and with a density of 5.06 g cm^{-3} .

3.3.4.2 Reduced Young's modulus, microhardness and strengthening mechanism

The reduced Young's modulus (E_r) and the microhardness of the samples were obtained by micro indentation load-displacement behaviour [99] with a Berkovich pyramidal-shaped diamond tip

indenter (NanoTestTM Vantage). The indentations were done on the cross-section with a load of 100 mN and a dwell time of 10 s. Thirty indentations were done on two samples for each condition, and the value was expressed as the average and standard deviation. In all cases, the diagonal of the indentations were no less than 5 μm in length. Thus, the indentation was considered to cover a representative area of the composite.

The composites reduced Young's modulus was calculated by the general rule of mixture of composites [2] in relation to the fraction of the reinforcer and the elastic modulus values reported by Magnani et al. [100] for β -SiC (427 ± 2 GPa) and by Li et al. [101] for MoS₂ (265 ± 13 GPa).

The strengthening effects present in the composite were calculated considering the relationship between hardness and ultimate tensile strength ($H \approx 3.3\sigma_{\text{UTS}}$) reported by Ebrahim et al. [102] for an electrodeposited nickel. The strengthening mechanisms were defined as follows:

The grain size strengthening, explained by the Hall-Petch relationship, was calculated by:

$$H_{HP} = H_0 + \frac{k}{\sqrt{d}} \quad (1)$$

where H_0 and k corresponded to electrodeposited nickel, established by a linear fit calculated from the data of the pure Ni deposits produced using DC4, DC10 and PR, and d is the average grain size. The pure Ni produced using US agitation was excluded from the linear fitting because of the additional strengthening effects present in the samples.

The total grain size strengthening was defined as the sum of each factor that contributed to the grain refinement: ($H_{HP(\text{SiC})}$) particles codeposition [9], ($H_{HP(i)}$) current density [34], and ($H_{HP(\text{US})}$), ultrasonic agitation [60]. The grain size strengthening driven by the current density ($H_{HP(i)}$) was calculated and varied in the hardness calculations for the composites depending on the input current densities: DC4, DC10 and PR.

The Orowan strengthening was approximated by:

$$\Delta H_{ow} = \frac{0.13 G_m b}{\lambda} \ln \frac{d_p}{2b} \quad (2)$$

where G_m is the shear modulus of the nickel matrix (75 GPa [103]), b is the Burgers vector (0.249 nm for nickel [104]), d_p is the average diameter of codeposited particles, and λ is the inter-particles spacing, measured by microscopy imaging. The distance was measured in samples where the Orowan strengthening effect will result in hardening values higher than 0.05 GPa only. For composites containing SiC particles with average diameter sizes of 50 nm, 60 nm, and 500 nm, the minimum inter-particles distance to achieve such hardening effect is $\sim 0.74 \mu\text{m}$, $\sim 0.77 \mu\text{m}$ and $\sim 1.10 \mu\text{m}$, respectively, otherwise, the strengthening effect is considered negligible (< 0.05 GPa). Sanaty-Zadeh et al. [20] reported that the Orowan strengthening effect decreases with increased inter-particles distance (as a function of particle size), showing negligible values in the micrometre size range.

The load-bearing strengthening was considered negligible in the calculations due to the minimal effect on the material strength [19,20].

The total enhanced dislocation density was defined as the strengthening due to factors that contributed to the changes in the crystalline structure. The ($H_{dd(US)}$) enhanced dislocation density strengthening, as a result of strain rate deformation [105] due to work-hardening by ultrasounds [106], was calculated by the difference between the grain size strengthening, approximated by Hall-Petch (equation 1) and the experimental hardness of pure Ni produced using US agitation. This value was considered constant and as the ($H_{dd(US)}$) contribution from US agitation on all composites produced under the same current density and using US agitation. However, in practice, the value of the strengthening effect will vary based on the US power, frequency and distance from the US source to the electrode in the case of a submerged US horn, which in this study were constant.

The ($H_{dd(SiC)}$) dislocation density strengthening provided by the particles codeposition was not considered in the present study.

While in cast nanocomposites, this strengthening effect has a high contribution to the total strength of the material [19,20], the Taylor relationship explains the enhanced dislocation density in terms of the effect of thermal mismatch between metal and particles reinforcer. In electrodeposition, the process temperature is constant, and thus the Taylor relationship is not applicable. Nevertheless, changes in the metal crystal structure might occur due to particles affecting the current field. Stappers et al. [24] proved that the current density in the deposition of nickel-iron multilayers was affected by codeposited micro-size glass (PMMA) and graphite particles. However, to the best of the author's knowledge, similar studies in SiC or nano-sized particles are absent, limiting the understanding of the possible defects resulting from changes in the electric field by particles. Thus, an estimation of the strengthening effect is not possible due to the lack of approximation methods for electrodeposited nanocomposites, as the Taylor relationship approximates the strengthening in cast nanocomposites.

The particles hardening effect was approximated by the rule of mixture of composites [2,107,108]:

$$\Delta H_p = H_p(V_p) \quad (3)$$

where V_p is the volume fraction of particles and H_p their hardness (20 ± 0.5 GPa for β -SiC [100]).

The overall hardness of the composite was approximated by the contribution and combination of the strengthening effects present in the material. Two methods were used to determine the hardness, sums of contribution, and the modified Clyne method. The latter accounts for the interdependencies between strengthening mechanisms and particles codeposition [20].

The sums of contribution is defined as:

$$H_C = H_{HP(i)} + \Delta H_{HP(SiC)} + \Delta H_{HP(US)} + \Delta H_{dd(US)} + \Delta H_{ow} + \Delta H_p \quad (4)$$

and the modified Clyne method [20] as:

$$H_C = H_{HP(i)} + \Delta H_{HP(US)} + \Delta H_{dd(US)} + \sqrt{\Delta H_{HP(SiC)}^2 + \Delta H_{ow}^2 + \Delta H_p^2} \quad (5)$$

3.3.5 Tribological tests

Pin-on-disk tests (NanoTest™ Vantage) were carried out to analyse the samples wear behaviour (described in detail in Supplement VII). The coated samples were rotated at 70 RPM against a diamond ball (diameter of 100 μm), acting as counter material with a loading of 1 N and the equivalent sliding distance of 1.32 m. The tests were designed to avoid wearing the coating down to the substrate. Thus, the wear rates could be correlated directly to the composite and not to possible differences in the coating thickness between samples. The friction coefficient was recorded every second and automatically during the tests by a friction probe connected to the tip. The surface and wear track morphologies were analysed by a surface profilometer (Surtronic® S-100 Taylor Hobson®) and a scanning electron microscope (SEM). The worn volume (mm^3) was calculated by approximating a torus with a cross-section equivalent to a circle segment, as depicted in blue in Figure 13. The volumetric wear factor ($\text{mm}^3 \text{Nm}^{-1}$) was calculated by dividing the worn volume (mm^3) by the applied load (N) and the total sliding distance (m).

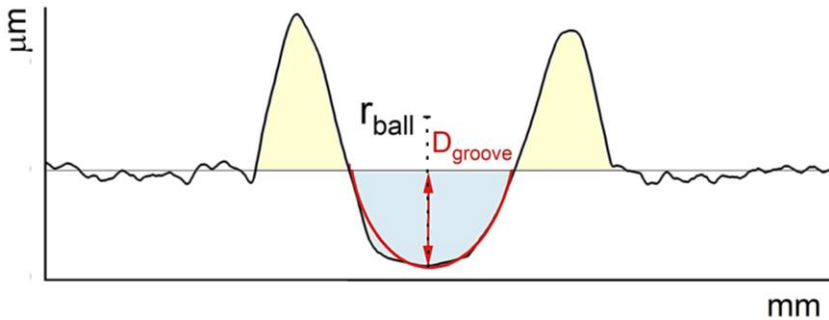


Figure 13: Area of the circular segment (red) draw by the radius of the ball (r_{ball}) and a sagitta equivalent to the depth of the wear groove (D_{groove})

SUMMARY OF RESULTS AND DISCUSSION

CHAPTER INTRODUCTION

The chapter is divided into four parts: the interaction of particles with the electrolyte, the influence of process parameters on the particles content, the microstructural changes, and the strengthening of the composites and wear behaviour.

4.1 INTERACTIONS BETWEEN PARTICLES AND ELECTROLYTE

The characterisation of interactions between particles and the aqueous solution comprises the main body of this section. Supplements I and III describe in details these studies.

The differences between particles behaviour were evident immediately after adding them to water or to the electrolyte. Each powder modified the initial pH of the solution differently (Table 5). The initial water pH was increased from 6.0 to 8.0 by adding SiC50 or to 6.5 by adding SiC60. Hovestad et al. [40] suggested adsorption of H^+ on the surface of the particles as a possible pH modifier. Similar behaviour was observed after adding the particles to the electrolyte despite the presence of boric acid as a pH buffering agent. The addition of SiC50 increased the Watts bath pH from 3.0 to 3.4, while SiC60 did not affect the electrolyte pH. After adding SiC500 to water or Watts bath, the opposite effect, a decrease in the pH, was observed. The differences in the magnitude of the pH variations and the contradictions between acidification and basification after particles addition revealed a discrepancy

between the surface state of the particles, leading to variations in the particles-electrolyte interaction.

Table 5: Water and Watts electrolyte pH, before and after the addition of particles.

Initial pH ₀	SiC50 pH	SiC60 pH	SiC500 pH
H ₂ O = 6.0	8.0	6.5	3.0
Watts = 3.0	3.4	3.0	2.7

A surface treatment of the particles was proposed to minimise the differences between different particles that nominally should have the same composition, answering RQ1. The suspensions were studied before and after pre-treatment and in the presence of a surfactant (SDS).

4.1.1 Surface treatment

Supplement I reports the study of a particles surface treatment. The research aimed to address RQ1 by providing a method to control the variable that the particles surface state represents in the electrodeposition of composites. A surface treatment based on nitric acid was developed to bring different particles to a common surface state even if particles were from different suppliers, different size or production route. Kobayashi et al. [109] used a similar surface treatment on Si or SiC to achieve SiO₂ surface layers by nitric acid oxidation in thin-film transistors.

The particles surface treatment (ST) consisted of: (i) Particles of different sizes and suppliers washed in water to dissolve any water-soluble residual substances from the manufacturing process. (ii) The solution was filtered to remove the water excess. (iii) Nitric acid was added to the solution and stirred for 15 min to allow the etching of the surface of the particles. (iv) The solution was rinsed and filtered with water until the pH was stable at 6.0. The residual water was translucent in all rinse and filtering steps, pointing to no noticeable loss of visible-sized particles.

4.1.2 Particles ζ -Potentials and particles size

The characterisation of the particles surface state by ζ -potentials, i.e. their interaction with the medium, before and after the surface treatment, is described in Supplement I. The effects of the addition of SDS in particles-electrolyte interactions is described in Supplement III. RQ1 is answered by studying the particles-electrolyte interactions and the capability of the surface treatment to control their effects and minimise the scattering in the powder behaviour.

The ζ -potential values of the particles in a diluted Watts bath were negative and close to zero (Figure 14), implying poor suspension stability with a tendency to flocculate [41]. Indeed, particle size measurements taken in the suspension showed an increase in size due to particles agglomeration. SiC 50 nm particles showed an agglomerations size of $430.4 \pm 120.1 \mu\text{m}$ after adding them to a diluted Watts bath, while SiC 500 nm showed an agglomeration size of $881.5 \pm 330.6 \mu\text{m}$. Supplement I includes cross-section SEM images of SiC500 (Figure 3 in supplement) showing incorporation of particles of a very different size from those measured in suspension, while SiC50 SEM imaging did not show any particles agglomeration.

SiC50 and SiC60 showed similar ζ -potential values, whereas SiC500 showed values of a few millivolts more negative. The difference between values between particles with the same chemistry and suspended in the same solution was due to differences in their surface state. It is presumed that differences between the production methods of nano and SiC500 particles led to variations in the particles surface state, i.e. changing the particles-electrolyte interactions differently. The production method of SiC60 (plasma arc vapour method) was the only publicly mentioned in the material's technical sheet. This information was not available for SiC50 or SiC500.

The powders surface treatment (ST) established a comparable particles surface state, thus minimising differences and bringing particles to a similar chemical interaction with the solution,

stabilising the ζ -potential values within the same range for all the particles independently of the supplier or size (Figure 14).

Supplement III introduces the addition of SDS to the electrolyte. Adding an anionic surfactant such as SDS caused a minor increase of the absolute ζ -potential value of SiC60, becoming more negative. Lari et al. [42] also reported more negative ζ -potentials values in Ni-Co/SiC baths after adding SDS. Kenjiro et al. [110] reported as well negative ζ -potential for SiC in the presence of SDS. The SiC50 and SiC500 particles also showed more negative values in Watts+SDS. However, the particles agglomeration size did not vary compared to additive-free Watts, showing values of $560.5 \pm 256.7 \mu\text{m}$ for SiC50 and $840.5 \pm 256.7 \mu\text{m}$ for SiC500.

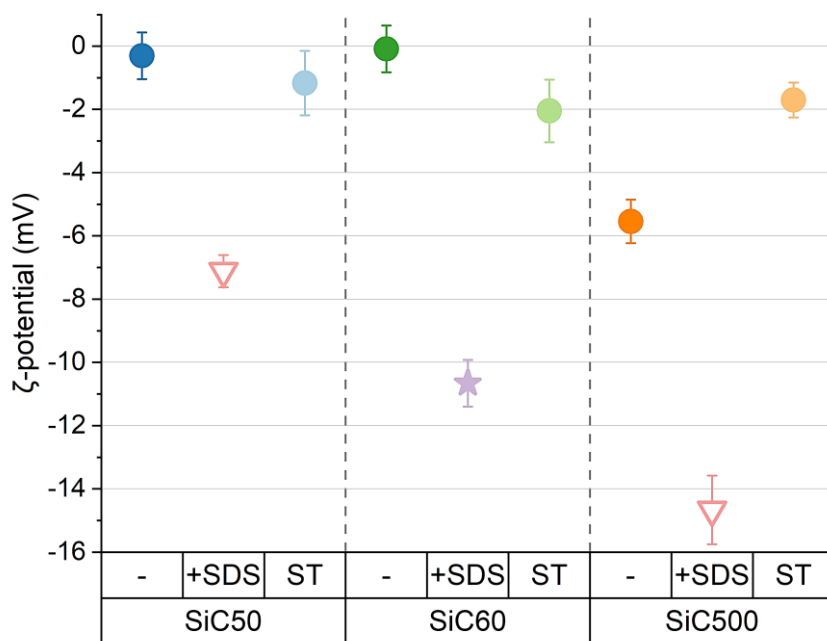


Figure 14: ζ -potentials of SiC50, SiC60 and SiC500 (0.2 g L^{-1}) in diluted (25%) Watts bath, with and without surface treatment (ST), and after addition of SDS.

4.1.3 Titration

The titration curves (Figure 15) showed visible pH buffering for all SiC particles when added to water, and they also confirmed the

significant differences between the particles surface state before surface treatment. Depending on the surface state, desorption of H^+ from the surface of the particles might counteract the addition of OH^- , delaying the pH change. Compared to the water titration curve (black line, Figure 15), SiC60 particles showed a pH buffering effect with a pH change with a gentler slope and no stabilisation plateau. SiC50 particles delayed the change of pH, showing a pH buffering effect more substantial than SiC60. SiC500 titration curve showed the strongest pH buffering, showing a stable pH even after the addition of 8 mL of the titrator.

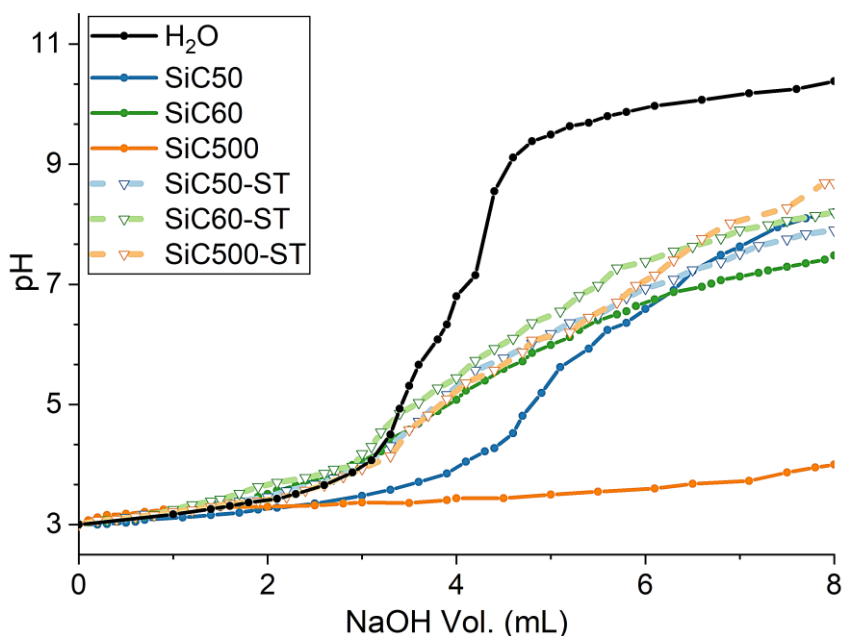


Figure 15: Titration curves (NaOH 0.01M) on 60 mL volume of H_2O and 20 g L^{-1} of SiC before and after surface treatment (ST).

Similar to the observations based on the ζ -potential measurements, the titration curves of the ST-particles confirmed the change of the particles surface state after the treatment (Figure 15). The buffering capability of the particles was reduced, and more importantly, all particles showed similar curves independently of the size, batch, or production route of the particles. After ST, the titration curves shifted closer to water, and the slope change

occurred with less addition of NaOH, thus showing a similar particles chemical behaviour and pH interaction.

4.2 PARTICLES CODEPOSITION

The main body of this section firstly covers the codeposition of particles as the result of the effects and control of particles-electrolyte interactions, studied in Supplements I and III, answering RQ1 and RQ2. Secondly, the type of agitation by stirring or US agitation studied in Supplements IV and VI. Finally, the current type: DC or PR, studied in Supplements II and III, is covered, addressing RQ2. This section also includes the influence of the particles on the side reactions, e.g. hydrogen evolution, studied in Supplements I to VI.

4.2.1 Effects on hydrogen evolution reaction (HER)

The pH was measured after each electrodeposition and compared to the initial pH (3.0). In all cases, the pH increased during deposition due to side reactions, i.e. hydrogen evolution [26]. Therefore, the current efficiency (CE) of nickel deposition was lower than 100%.

Pure nickel samples plated by DC studied in Supplements II to IV showed virtually no change in pH after electrodeposition and a CE of about 98%, independently of the agitation mode.

The addition of particles promoted an increase in hydrogen reduction. SiC50 and SiC60 composites from Supplements I, II, IV, V and VI produced by DC showed an increase in pH of about 0.1. SiC500 addition caused a higher increase in hydrogen evolution, showing an increase of pH of around 0.3 after deposition under stirring agitation, whereas ~0.2 under US agitation. The surface treatment of the SiC500 particles led to a smaller change in pH, of about 0.1. In all composites produced by DC, the CE decreased to ranges from 92 to 96%. However, the results agreed with what had been reported as cathode efficiency for Watts baths [37].

In the cases of both pure Ni and composites produced by PR in Supplements II and III, the CE was around 90%, despite the high pH

increase ranging between 0.4 and 1.0. The lack of correlation between pH change and CE was due to hydrogen reduction occurring at each electrode for each pulse in the cycle, as well as the anodic side reactions and current efficiency due to partial anode passivation. The reduction reaction alternates between the cathode during the cathodic pulse and at the counter electrode during the anodic pulse. Hence, hydrogen was reduced continuously for the total duration of the process, promoting further pH changes, while the Ni mass deposition was dependant on the cathodic and anodic CE.

The samples containing graphite, both as single and dual powder mix, studied in Supplement V, showed an increase in pH of around 0.1 but a decrease in CE down to 71% and 76%, respectively. These samples showed dendritic structures, which broke off from the surface after US cleaning, remaining in the water as debris. The loss of these metal dendrites resulted in a decrease in the total deposited metal mass. Therefore, after comparing the deposited mass to the theoretical electroplated mass, the CE resulted in a lower value with no link to hydrogen reduction.

The addition of MoS₂ particles in Supplement VI showed a strong influence on the hydrogen evolution. MoS₂ particles are catalytic for hydrogen reduction, providing multiple active sites on their surface: edge sites, sulfur vacancies, and grain boundaries to promote hydrogen evolution reactions [111]. MoS₂-DC4/US showed a pH increase of around 0.4 and about 65% CE, comparable to the observations made by Chang et al. [112]. Dual SiC:MoS₂-DC2/US showed a considerable pH increase of about 0.8 and CE around 78%.

4.2.1.1 Cathodic polarisation

Supplement IV includes the study of cathodic polarisation curves in a suspension of particles without metal salts (Figure 16). Therefore, showing the direct influence of the particles in the reduction of H⁺.

The polarisation curve of the water without particles (black-coloured) showed an initial limiting current plateau, corresponding to the reduction of H⁺ available in the solution at

pH 3. The hydrolysis coincided with the curve after the change of slope. The addition of SiC50 (blue-coloured curve, Figure 16) and SiC500 (orange-coloured curve, Figure 16) encouraged an initial shift in the current density to reduce the free H^+ , more evident in SiC500 encouraging a higher reduction rate. The part of the SiC50 curve corresponding to hydrolysis was equivalent to the solution without particles. Whereas in SiC500, the curve was displaced, showing their significant influence over H^+ , observed on their buffer capability proved by the titration.

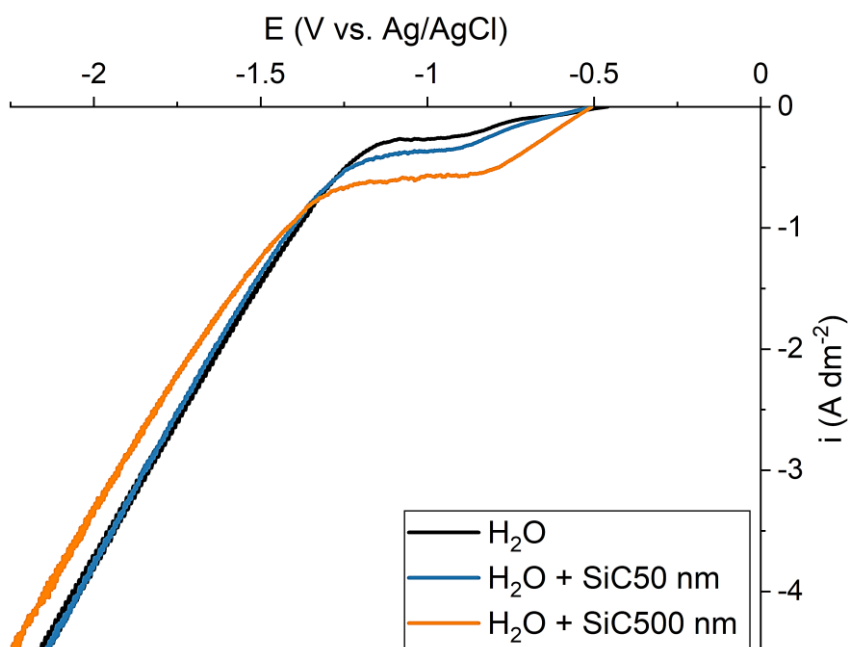


Figure 16: Polarisation curves of a solution without Ni salts and after addition of SiC50 and 500.

4.2.2 Particles codeposition rate

4.2.2.1 Surface treatment and electrolyte composition

Figure 17 shows the SiC codeposition rate after electrodeposition, with and without ST, and in a 2 L cell from an additive-free Watts or with SDS.

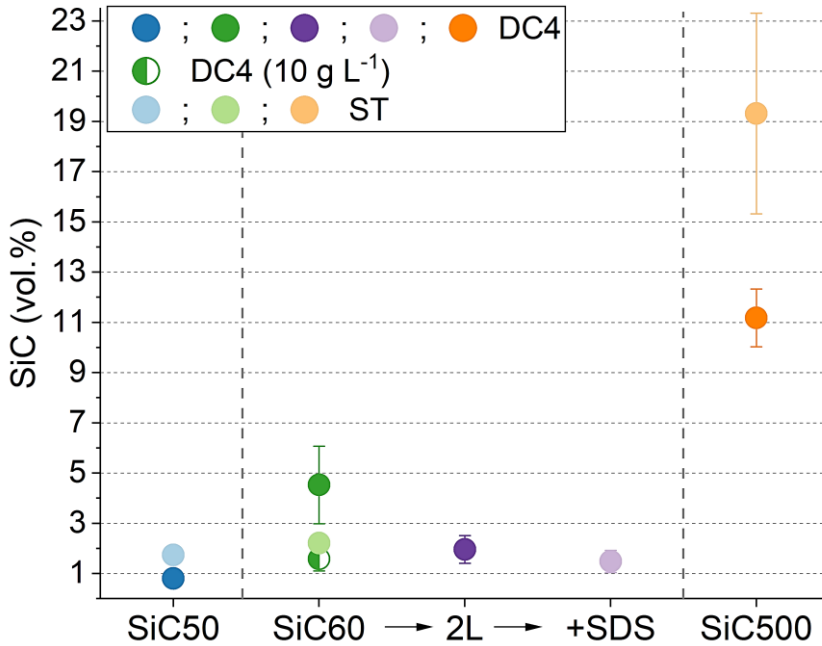


Figure 17: Particles content of composites produced using DC4 (vol.%). Codeposited SiC with and without ST, and after addition of SDS.

The codeposition of SiC50-DC4 was low, around 0.8 vol.% content, whereas SiC60-DC4 was close to 4.5 vol.%. The differences in codeposition rate, despite having almost the same particles average size, chemistry and electroplating conditions, well represent the controversy on codeposition rates of nanoparticles often encountered in literature results [9]. These differences in codeposition rate prove that the particles surface state, and its understanding, has an essential role in particles codeposition control. The ST brought particles to a common surface state, confirmed by similar ζ -potential values and titration curves, allowing the control of the particles-electrolyte interactions and providing reproducibility to the composite electrodeposition. For instance, after ST, particles (ST-SiC50 and ST-SiC60) with similar sizes and from different suppliers showed similar codeposition rates. For SiC50/ST-DC4, the codeposition was more than doubled (up to 1.7 vol.%) and halved (down to 2.2 vol.%) for SiC60/ST-DC4. For the latter, the scattering of the data was reduced compared the

to as-produced, thus showing the higher reproducibility in the composite production after ST.

The codeposition of SiC60 10 g L^{-1} -DC4 was carried out with half of the powder load (10 g L^{-1}) used in SiC60-DC4 (20 g L^{-1}), resulting in a reduction in the codeposition rate (1.6 vol.%). Previous studies also established the same correlation between the decrease in powder load and particles content [113–115].

The codeposition of the larger particles in SiC500-DC4 was higher (11 vol.%) compared to the nanoparticles. The volume content in SiC500/ST-DC4 increased up to 20 vol.% as a result of the ST. It is presumed that the codeposition rate benefited from a reduction in the interaction between the SiC500/ST surface and hydrogen evolution observed on the decrease of ΔpH . The decline in H_2 bubble evolution permits longer particles residence time at the cathode surface, improving their entrapment by the growing metal. These unforeseen interactions between non-inert particles and electrolyte might hinder the codeposition rate. The ST proposed in Supplement I offers a method to control these interactions, and in the case of SiC500, improved the codeposition.

SiC60(2L)-DC4 codeposited around 2 vol.%, lower than SiC60-DC4, despite the same electroplating conditions except for the size of the cell. This difference between SiC content highlighted how susceptible electroplating systems are to changes in the set-up and the importance of accounting for the electrolytic cell geometry and the hydrodynamics. SiC60(2L+SDS)-DC4 was codeposited in the presence of a surfactant, showing a decrease in SiC content (down to 1.4 vol.%). The ζ -potential of SiC60 after SDS addition compared to the values in additive-free Watts was more negative. Considering Guglielmi [75] model for particles transport and codeposition, negatively charged particles might be repulsed away from the negatively charged cathode, causing a decrease in the incorporation rate. Supplement III describes the mechanisms in details.

4.2.2.2 Agitation

The agitation type affected the particles codeposition rate (Figure 18) and their dispersion within the matrix (Figure 19). SiC50-DC4/US and SiC60-DC4/US showed higher codeposition rates compared to the composites produced under stirring agitation. The capacity of producing enriched deposits by US agitation was evident by comparing SiC60-DC4/US to SiC60 (Figure 18). US agitation encouraged a uniform particles dispersion instead of particles agglomerates (Figure 19a and b) and caused a significantly higher codeposition with the same powder load (1.6 vol% in 10 g L⁻¹ using stirring), or even after doubling the powder load (4.5 vol.% in 20 g L⁻¹ using stirring). Similar effects were reported in previous studies with nanoparticles and US agitation [54,56].

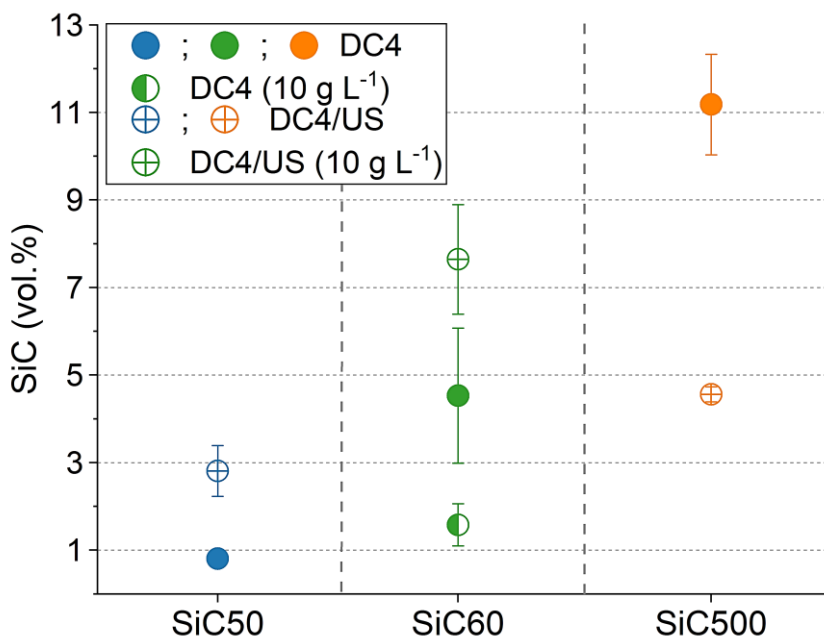


Figure 18: Composite particles content (vol.%) as determined by WDS of codeposited SiC using stirring or US agitation.

The codeposition of SiC500 using US was decreased compared to stirring by about 60%, from 11 vol.% down to 4.6 vol.%. The codeposition of larger particles was impacted negatively by the

ultrasonic waves and the cavitation near the cathode. In SiC500-DC4 using stirring, the particles were entrapped as agglomerates and showed a broad particles size distribution, ranging from smaller than 500 nm to micron sizes (Figure 19c). Whereas, in SiC500-DC4/US, particles were uniformly and well distributed, and codeposited particles appeared smaller than 500 nm in size (Figure 19d). In essence, US agitation appears to have encouraged a selective entrapment of the smaller particles. Since the US probe was immersed directly in the cell during electrodeposition, the unshielded surface was exposed to the cavitation. This may have caused the larger particles to collide and 'bounce' away from the electrode before being anchored by the growing metal [116], thus decreasing the volume content of SiC by repelling the larger particles.

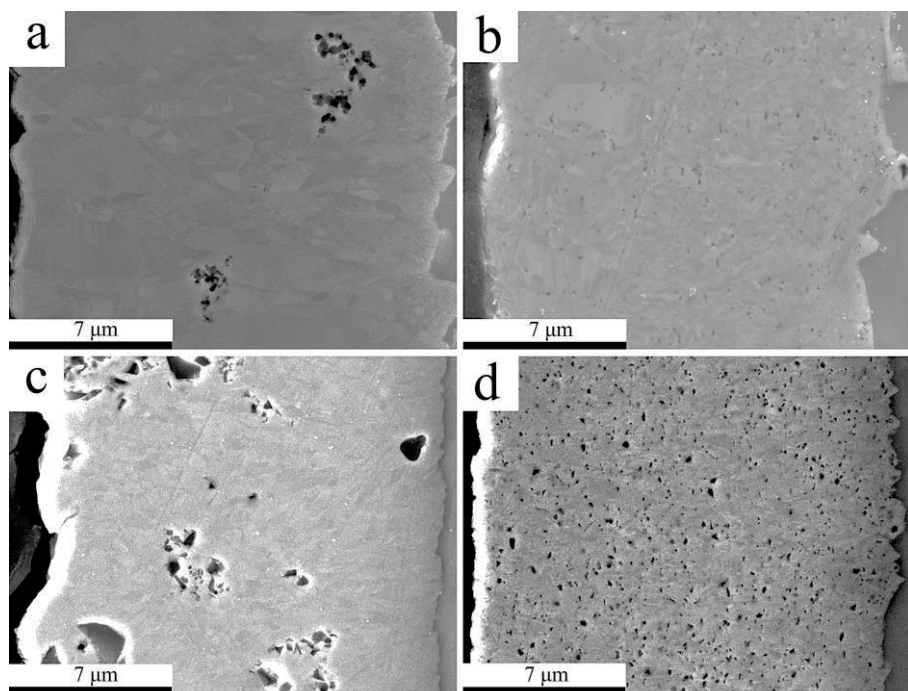


Figure 19: Cross-section SEM image of SiC60-DC4 using (a) stirring or (b) US agitation and SiC500-DC4 using (c) stirring or (d) US agitation. Taken from Supplement VII.

4.2.2.3 Current type and intensity

Variations in the current type and intensity modified the codeposition of nanoparticles (Figure 20). The nanocomposites produced by DC10 showed similar codeposition rates (~ 2 vol.%), even though the electrodeposition was carried out in cells with different volume, 500 mL for SiC50 and 2 L for SiC60. A similar entrapment mechanism present in both cells, driven by the high current density, might have caused nanoparticles to be rapidly captured by the fast-growing metal before fluid dynamics remove them away from the cathode surface. For instance, the DC4 codeposition for SiC50 in the 500 mL cell showed lower particles content (0.8 vol.%) than DC10 in the same volume cell.

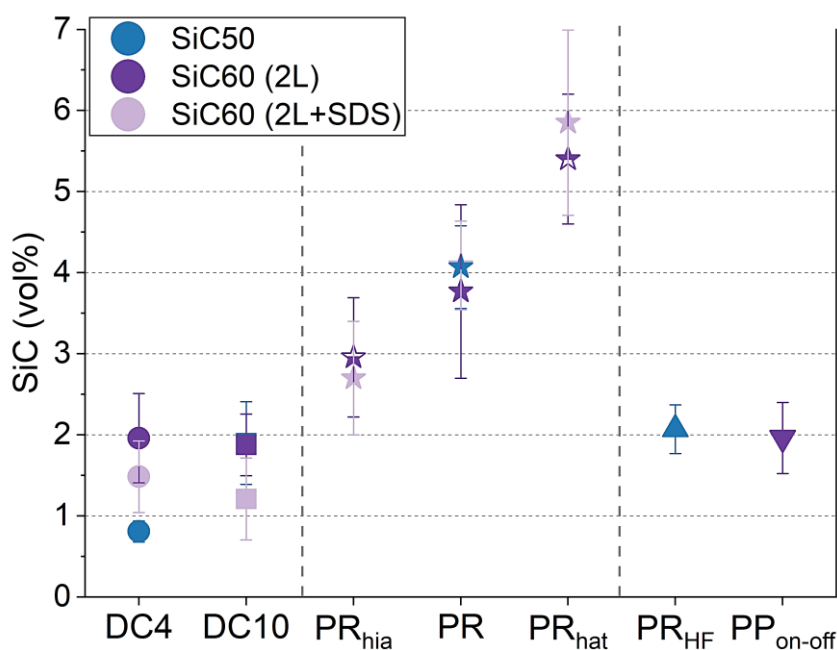


Figure 20: Composite particles content (vol.%) of codeposited SiC using different electric current densities and types.

The codeposition of SiC60(2L)-DC10 in the presence of SDS showed a decrease in SiC content (down to 1.2 vol.%) compared to the composite deposited from additive-free Watts (~ 2 vol.%). Analogous results are discussed in the previous section, where SiC60(2L)-DC4 also showed a decrease in particles content after

SDS addition. The electrophoretic transport and successive codeposition of negatively charged SiC60(+SDS) particles, observed by their ζ -potential value, might be hindered due to the repulsion from the negatively charged cathode.

Pulse-reverse (PR) electrodeposition was carried out by a waveform adapted to the particles average size: SiC 50 nm or 60 nm, provided by the supplier's production data. In both cases, the codeposition of SiC was significantly improved compared to DC deposition. The waveform was designed to entrap particles during the cathodic cycle and release some of the particles during the reverse cycle (Figure 21). Celis et al. [76] model of particles codeposition describes the incorporation rate as a function of the probability of particles being entrapped and the number of successfully transported particles to the cathode. The PR waveform was designed to increase the number of particles available for codeposition at the surface of the cathode during the cathodic cycle. In the successive cathodic period, newly arrived particles are entrapped, in addition to the re-entrapment of the previously released particles from the anodic cycle. Essentially, thanks to the continuous entrapment-release of particles, the incorporation rate was improved. The mechanisms are described in detail in Supplements II and III.

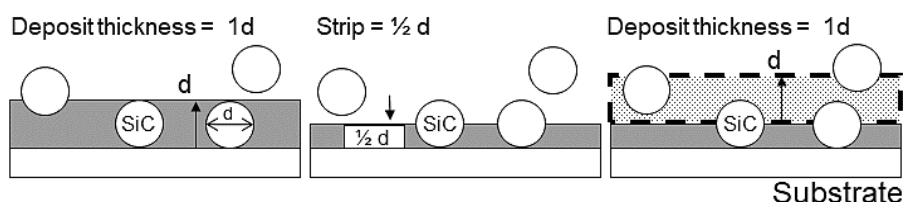


Figure 21: Pulse-reverse waveform representing the incorporation of nano-SiC.

All composites produced by the adapted PR waveform: SiC50-PR, SiC60(2L)-PR and the variations introduced in Supplement III (ic4, hia and hat) showed comparable SiC content, thereby showing the capability and reproducibility of the method to improve the particles incorporation rate compared to DC. Furthermore, despite the addition of SDS, SiC60(2L+SDS)-PR showed virtually the same codeposition rate, thus exhibiting the reproducibility of the

waveform in different electrolyte formulations. Supplement III describes a parametric study of the PR waveform, where the design was modified to verify which is the controlling parameter of the increase in the particles incorporation rates. The anodic cycle time was adjusted to promote a longer residence time of the particles on the surface of the cathode, permitting a controlled increase in the codeposition of particles. For instance, by increasing 65% the anodic cycle time, a modified PR_{hat} waveform increased the particles codeposition from 3.8 vol.% in SiC60-PR up to 5.5 vol.% (Figure 20). In contrast, the decrease of the anodic cycle time by 25% in the PR_{hia} waveform, albeit the increase in anodic current, caused a decrease in the particles codeposition rate down to 2.9 vol.% compared to the content (3.8 vol.%) observed in SiC60-PR (Figure 20).

Two additional types of pulse waveforms were used to test the critical role of the design of the anodic cycle based on the particles average size of the PR-waveform to increase the particles codeposition rate. Both pulses: High-frequency PR depositing SiC50 particles and pulse plating (PP_{on-off}) of SiC60, showed a codeposition comparable to DC10 (~2 vol.%). The design of these pulses: PR-HF, PP_{on-off} and PR (adapted to the particles average size), was purposely with a cathodic pulse current density of 10 A dm⁻². Thus, it confirms that adapting the anodic period to the particles size was the cause to enhance the codeposition.

4.2.2.4 Conductive particles

Table 6 shows the codeposition rate of graphite or MoS₂ particles. Supplements V and VI studies wear protection by the codeposition of SiC and self-lubricant particles as a dual dispersion mix.

Dual SiC:Graphite-DC4 showed a similar SiC and graphite content as the equivalent single power (either SiC or Graphite) composite electrodeposited with a particles concentration of 10 g L⁻¹. The comparison proved no synergies between codepositing particles. The microstructures of the deposits containing graphite, described in Supplement V, were not modified by graphite showing similarities to pure Ni.

Table 6: Volume content (%) of codeposited SiC, graphite and MoS₂ from Supplements V and VI.

	SiC60 10 gL ⁻¹ - DC4	Graphite- DC4	Dual SiC:Graphite-DC4	
			Graphite	SiC
Vol%	1.58 ± 0.48	3.99 ± 0.48	5.32 ± 1.50	1.45 ± 0.51
	SiC60 10 gL ⁻¹ - DC4/US	MoS ₂ - DC4/US	Dual SiC:MoS ₂ -DC2/US	
			MoS ₂	SiC
Vol%	7.64 ± 1.25	19.55 ± 1.60	8.27 ± 0.53	14.85 ± 1.10

The catalytic effect on the hydrogen reduction by the addition of MoS₂ particles caused intense H₂ evolution, leading to porosity in the MoS₂-DC4/US deposits (Figure 22a). Furthermore, the flake-shaped MoS₂ particles, once anchored on the metal, caused changes in the current distribution at the cathode surface, causing an uneven nickel electrocrystallisation, which led to dendritic structures and voids between the growing grains. Previous studies also reported similar defects in Ni-based composites with MoS₂ particles [117–119].

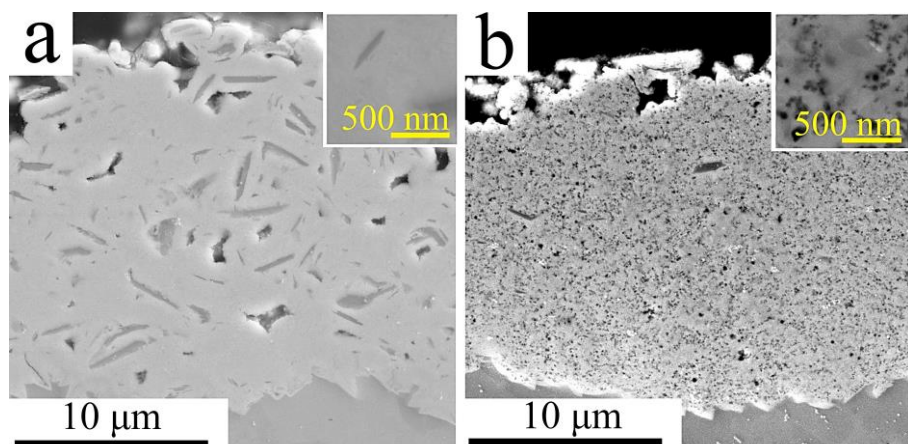


Figure 22: SEM cross-section image of composites produced under US agitation. (a) MoS₂-DC4 and (b) Dual SiC:MoS₂-DC2.

The particles content and appearance of MoS₂-DC4/US were similar to Ni-MoS₂ composites produced in a different study under high-shear mixing [119], showing a correlation between the two methods. The cross-section SEM image (Figure 22a) shows a broad MoS₂ particles size distribution ranging from micrometre sizes down to around 500 nm. These sizes were inconsistent with the reported as-received particles (90 nm average diameter size). Zhou et al. [119] also reported a broad particles-size distribution in MoS₂ particles codeposited without using high-shear mixing.

The cross-section SEM image of Dual SiC:MoS₂-DC2/US (Figure 22b) shows the synergistic effect between codepositing particles, opposite to SiC:Graphite codeposition. The content of SiC was almost doubled compared to the single SiC system, whereas the content of MoS₂ was decreased (Table 6). The codeposited MoS₂ appeared smaller in size in the dual composite than in the single particles composite, possibly due to the SiC particles. Jiang et al. [120] observed PTFE particles covered by nano-SiC after codepositing dual nano-SiC:PTFE in a nickel matrix. A similar interaction between MoS₂ and SiC particles might have caused a content increase of SiC in place of MoS₂. The larger MoS₂ might have attracted nano-SiC in their surrounding, promoting a codeposition of SiC per MoS₂ particles. As a result, a selective entrapment was prompted, allowing only the smaller MoS₂ particles to codeposit. The codeposition of both particles was uniformly dispersed within the matrix.

4.3 MICROSTRUCTURAL CHANGES

The changes in the nickel electrocrystallisation are studied in detail in Supplements I, II, IV, V and VI, addressing RQ3. The microstructural changes are correlated to the deposition parameters: agitation and current density, and particles codeposition. Table 7 summarises the average grain size and preferred crystal orientation of the nickel and nickel-based composites.

Table 7: Average grain area (μm^2) and max texture intensity in units of multiplies of random distribution (mrd) of pure nickel and Ni-matrix composites.

Sample	Average grain area (μm^2)	Max texture intensity (mrd)
Ni – DC4	8.09 ± 0.39	<div> <div>max = 4.88</div> </div>
Ni – DC4/US	7.77 ± 0.46	<div> <div>max = 4.58</div> </div>
Ni – DC10	2.64 ± 0.18	<div> <div>max = 2.37</div> </div>
Ni – PR	6.72 ± 0.36	<div> <div>max = 2.00</div> </div>

Table 7 (continued): Average grain area (μm^2) and max texture intensity in units of multiplies of random distribution (mrd) of pure nickel and Ni-matrix composites samples.

Sample	Average grain area (μm^2)	Max texture intensity (mrd)
SiC50 – DC4	7.12 ± 0.34	<div> <div>max = 4.01</div> </div>
SiC50/ST – DC4	6.20 ± 0.37	<div> <div>max = 2.54</div> </div>
SiC50 – DC4/US	6.71 ± 0.43	<div> <div>max = 3.53</div> </div>
SiC50 – PR	5.22 ± 0.36	<div> <div>max = 1.99</div> </div>

Table 7 (continued): Average grain area (μm^2) and max texture intensity in units of multiplies of random distribution (mrd) of pure nickel and Ni-matrix composites samples.


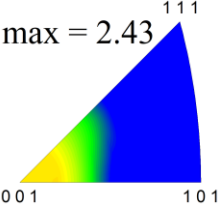
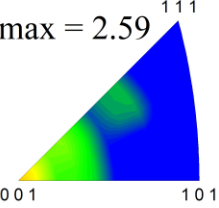
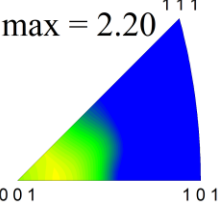
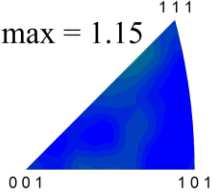

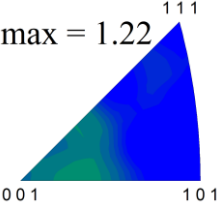
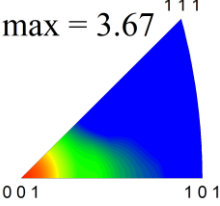
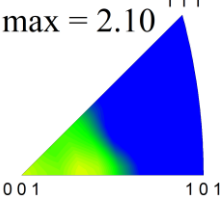
Sample	Average grain area (μm^2)	Max texture intensity (mrd)
		
SiC60 – DC4	4.76 ± 0.44	<div> <div>max = 2.43</div>  </div>
SiC60/ST – DC4	5.59 ± 0.43	<div> <div>max = 2.59</div>  </div>
SiC60 10 gL ⁻¹ – DC4/US	4.24 ± 0.30	<div> <div>max = 2.20</div>  </div>
SiC500 – DC4	1.40 ± 0.13	<div> <div>max = 1.15</div>  </div>

Table 7 (continued): Average grain area (μm^2) and max texture intensity in units of multiplies of random distribution (mrd) of pure nickel and Ni-matrix composites samples.

Sample	Average grain area (μm^2)	Max texture intensity (mrd)
		
SiC500 – DC4/US	1.29 ± 0.16	<div> <div>max = 1.22</div>  </div>
Graphite – DC4	7.86 ± 0.40	<div> <div>max = 3.67</div>  </div>
Dual SiC:Graphite – DC4	6.42 ± 0.30	<div> <div>max = 2.10</div>  </div>
MoS ₂ – DC4/US	< 0.02	-
Dual SiC:MoS ₂ – DC2/US	< 0.02	-

The selection of the input parameters and the content and size of codeposited particles provoked different magnitudes of grain refinement. The different extent of grain refinement caused the nickel microstructure to transition between four distinctive structures: (i) large columnar grains growing uninterrupted from the surface (Figure 23a), also observed in previous studies of pure nickel [121,122], to (ii) thinner and elongated columns with smaller grains in-between columns (Figure 23b), to (iii) grain structures dominated by equiaxial-looking growth (Figure 23c), and to (iv) nanocrystalline structures.

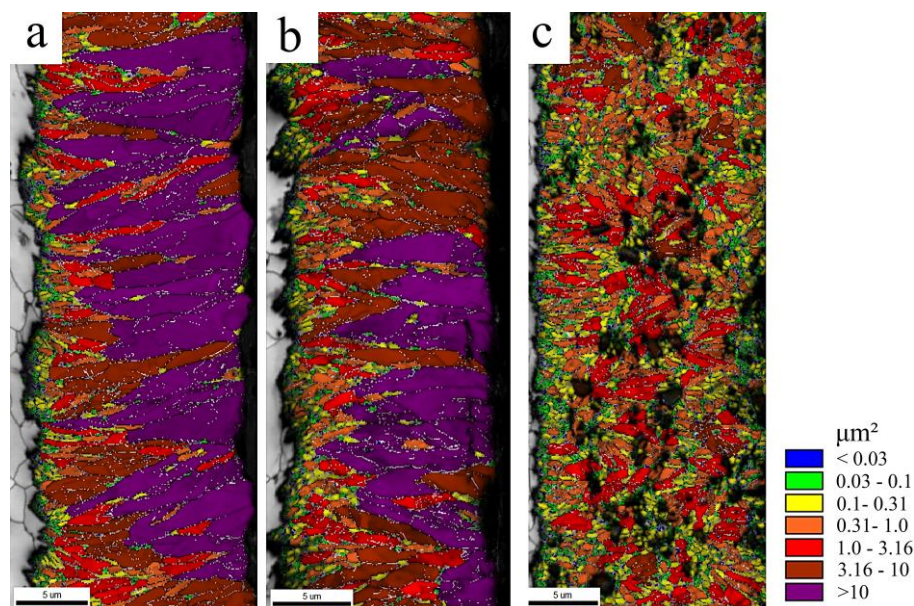


Figure 23: Grain size map, colour-coded in relation to the range of the grain's area (μm^2). (a) Ni-DC4, (b) SiC60 10 g L⁻¹-DC4, (c) SiC500-DC4.

Supplement II introduces the study of the effects of current density on the nickel microstructure. The higher current of DC10 led to a change from the larger columnar grains observed in pure nickel at DC4 to thinner structures, also causing an increase in the number of smaller grains. Thus, the average grain size of the Ni-DC10 deposit was decreased compared to Ni-DC4 (Table 7).

The use of US agitation in the deposition of pure nickel, studied in Supplement IV, showed a minor grain refinement effect in the microstructure (Table 7), also reported by Tudela et al. [60]. US agitation caused an increase in the number of smaller grains in the Ni-DC4/US deposits but with no effect on the grain morphology, also showing large columnar grains.

The preferential crystal growth in pure Ni samples was also modified by the selection of current density or agitation. Two factors were identified which changed the preferential growth from a dominant $\langle 100 \rangle$ direction observed in Ni-DC4 (Figure 24a) to less intense in Ni-DC10 (Table 7): (a) The increase of smaller grain led to more randomly oriented grains and (b) the increase of hydrogen evolution. The reduction of H^+ into H_2 , and the formation of $Ni(OH)_2$ (favoured by local pH change), are known as Ni growth inhibitors [26].

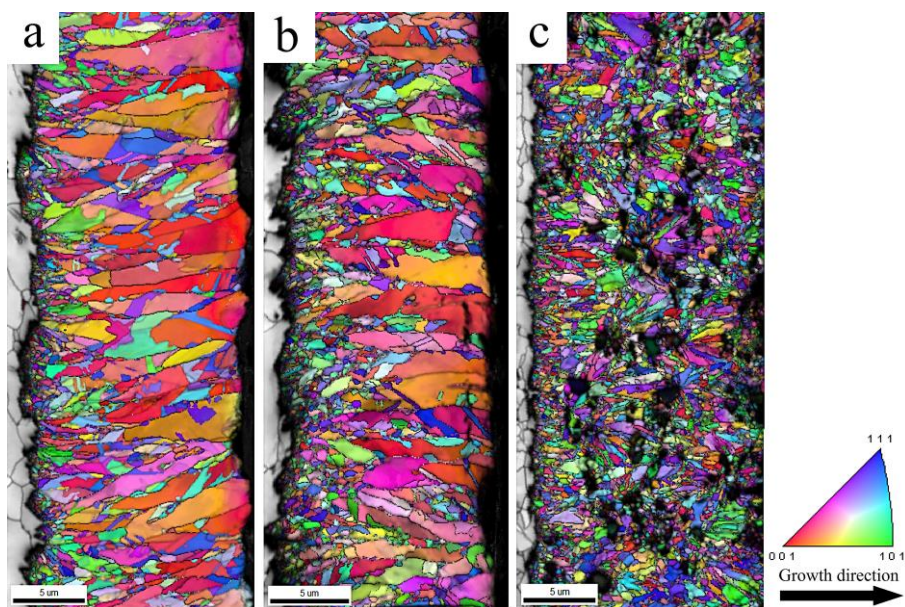


Figure 24: Orientation map, colour-coded in relation to the electrodeposits growth direction, shown by an arrow in the legend. (a) Ni-DC4, (b) SiC60 10 gL⁻¹-DC4, and (c) SiC500-DC4.

The particles codeposition caused significant changes in the Ni electrocrystallisation depending on their content, size, and dispersion within the matrix size. The nickel microstructure was refined, and the preferential crystal growth modified (Table 7, Figure 23b and Figure 24b). The intensity of the $\langle 100 \rangle$ Ni crystal growth was decreased as the result of the grain refinement and the change of columnar growth due to particles codeposition. Furthermore, particles promoted hydrogen evolution and thus caused inhibited Ni growth, contributing to decrease texture intensity.

The SiC50-DC4 microstructure was dominated by large columnar grains and slightly refined by particles codeposition [9]. Although due to the low particles content (0.8 vol.%), the microstructure was comparable to Ni-DC4 (Table 7).

The similarities between SiC50/ST-DC4 and SiC60/ST-DC4 microstructures due to similar particles content were evident. This observation proves how critical is the reproducibility of codeposition rate in the electrodeposition of nanocomposites. Samples with similar nanoparticles content: SiC50/ST, SiC60/ST, and SiC60 10 g L^{-1} showed similar grain sizes (Table 7) and comparable microstructures (Figure 23b), with large columnar grains and small-sized grains in-between columns. The SiC60-DC4 microstructure was further refined (Table 7) due to the higher particles content (4.5 vol.%), showing thinner columns with small grains in-between.

SiC60 10 g L^{-1} -DC4/US microstructure was finer than in composites using stirring (Table 7). The resulting microstructure was dominated by equiaxial grains with some columnar growth, showing the benefits of US agitation and the effects of high codeposition rates (7.6 vol.%) and uniformly dispersed SiC particles (Figure 19b) in the resulting composite.

The codeposition of SiC500 using stirring or US caused well-refined microstructures with nano-sized grains arranged as equiaxial structures (Figure 24c). The larger size of non-conductive SiC500, once anchored to the metal surface, increased the local cathodic current density around the particles, favouring metal nucleation

rate over grain growth, leading to grain refinement (Table 7). The preferential crystal growth in Ni was strongly modified by SiC500 particles (Figure 24c) independently of the agitation type. The combined effect of high grain refinement and prompted hydrogen evolution caused by SiC500, higher than the one observed in SiC50 or SiC60 codeposition, led to almost randomly oriented deposits.

The different types of agitation and particles sizes led to changes in the surface topography of the samples (Figure 25) as the result of grain refinement and changes in preferred crystal orientation.

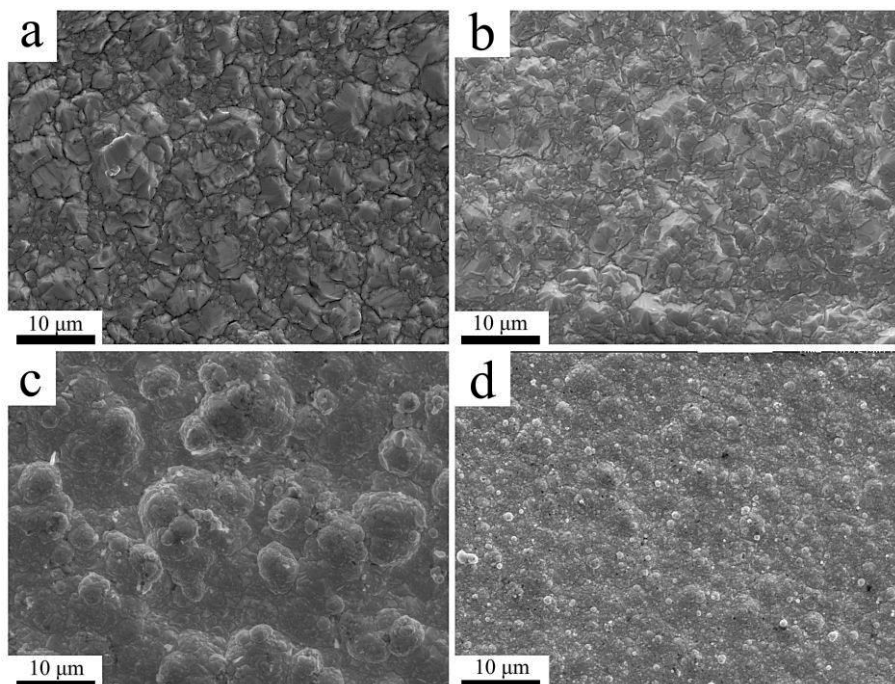


Figure 25: SEM image of surface topography of (a) Ni-DC4, (b) SiC60-DC4, (c) SiC500-DC4 and (d) SiC500-DC4/US. Taken from Supplement IV.

A pyramidal shaped surface topography was observed for all the nickel deposits dominated by the $\langle 100 \rangle$ uninhibited crystal orientation growth (Figure 25a). Although particles codeposition favoured grain refinement, the composites showed a similar pyramidal-shaped topography (Figure 25b). The surface roughness in pure Ni or composites produced using stirring and DC4 showed similar R_a values, ranging from 0.39 to 0.44. DC10 and US agitation

reduced the surface roughness to values ranging between 0.27 and 0.32 in all pure Ni or nanocomposite samples.

The addition of SiC500 modified the surface topography to globular shaped structures (Figure 25c) due to the preferred $\langle 111 \rangle$ crystal orientation growth mode caused by an inhibited growth. Winand [27] diagram (Figure 4), introduced in Chapter 1, describes how different microstructures are achieved as a function of inhibition. For instance, in SiC500 deposits due to inhibition, the bidimensional nucleation (columnar growth) was substituted by tridimensional nucleation (globular growth). Pavlatou et al. [69] also observed changes from pyramidal-shaped surface structures dominated by $\langle 100 \rangle$ texture, in uninhibited nickel deposits, to globular-shaped surface structures dominated by the $\langle 111 \rangle$ crystal orientation. The size of surface globularity was reduced by the US agitation (Figure 25d), thus reducing the R_a from 0.74, observed in SiC500-DC4, to 0.23 in SiC500-DC4/US.

The addition of irregular-shaped electrically conductive particles, such as graphite and MoS₂ prompted changes in the nickel electrocrystallisation. He et al. [123] illustrated the mechanisms of growth of NiP in the presence of conductive WS₂ particles. The codeposited particles provided an irregular cathodic surface changing the electric current distribution. At these points provided by the particles, current density was concentrated instead of uniformly distributed across the surrounding area. Therefore, the reduction of Ni ions was preferred on the surface of the particles, providing multiple nucleation sites instead of the growth of large columnar grains.

The codeposition of graphite particles had a limited impact on the grain refinement due to their low incorporation rate in both Graphite-DC4 and Dual SiC:Graphite-DC4. Furthermore, Dual SiC:Graphite showed similar R_a values, grain size and preferred crystal orientation compared to the single-SiC composites with similar SiC content (Table 7).

The addition of MoS₂ caused a substantial grain refinement in MoS₂-DC4/US and Dual SiC:MoS₂-DC2/US. The averaged grain area of these samples was reported in Table 7 as 'lower than' (<) due to

the nanocrystalline microstructure, confirmed by TEM imaging (Figure 26). The maximum resolution of the mapping technique was insufficient to index the nano-sized grains and thus unable to include them in the weighted average of the grain area or determine the preferred orientation. Hence, the grain area was supposed to be lower than the resolution of the technique. Nanocrystalline structures in nickel after the addition of MoS₂ were also observed by Shourije et al. [124], although the authors linked them to the presence of saccharine. Garcia-Lecina et al. [58] and Tudela et al. [116] reported nanocrystallinity in nickel composites after codepositing conductive WS₂.

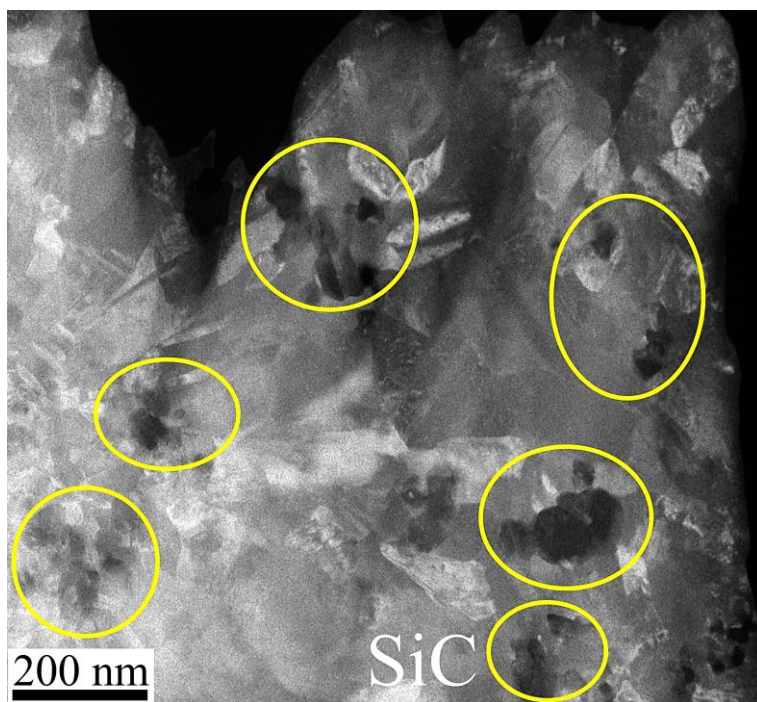


Figure 26: TEM cross-section image of Dual SiC:MoS₂-DC2/US. The yellow-coloured ovals indicate the SiC particles. Taken from Supplement VI.

4.4 HARDNESS AND WEAR BEHAVIOUR

Supplements I to VI study the microhardness of the composites as the result of the combined effect between the microstructural changes of the nickel matrix and the particles codeposition. Supplements V and VI study wear resistance of dual dispersion composites, where the functionalities of hard SiC and self-lubricant particles were combined. Supplement VII studies the contribution of different strengthening factors: Hall-Petch, Orowan, enhanced dislocation density and particles incorporation in the hardness of the composite coating, analysed by modelling methods. The results were also correlated to the wear behaviour based on the elastic strain to failure, i.e. H/E_r ratio, answering RQ4.

4.4.1 Hardening by particles codeposition

Figure 27 shows the particles volume content and hardness of the deposits. The results display an apparent linear relationship between terms, showing that in electrodeposition methods, where the incorporation of particles was increased, the hardness of the composite was also increased. However, the results also highlight the unreliability of the electrodeposition process in assuring similar particles content, leading to large variations in the hardness value of the composites. For instance, SiC50 and SiC60 under DC4 showed a significant difference between particles content and total hardness despite using the same nominal particles size.

The control of the electrodeposition process, possible by the powder surface treatment, allowed a reproducible codeposition rate in SiC50/ST and SiC60/ST, reducing the scattering of the data, observed by the smaller error bars, showing as well comparable hardness values. Likewise, the PR adapted to the particles average size showed the potential of controlling the improvement of the particles codeposition by modulating the anodic cycle time, increasing the hardness.

However, in some of the deposits, particles content and hardness were not related directly, showing a contradiction between hardness values and codeposition rate. For instance, SiC60 showed

a lower hardness than SiC500/US, despite the same content of the particles, and SiC60/US and SiC500 showed similar hardness values although particles content was higher in the latter. Thus, indicating that the strengthening effects act differently in each deposit, varying as the result of the process parameters and the characteristics of the codeposition: particles size, dispersion and volume content.

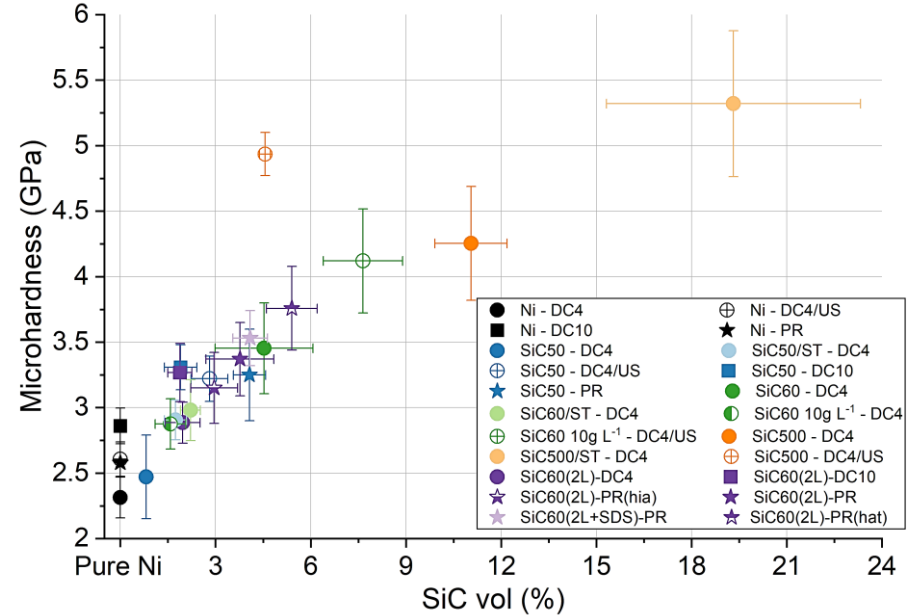


Figure 27: Microhardness (GPa) vs SiC volume content (%) of the deposits for each condition (averaged from two samples).

Supplements V and VI discuss in detail the hardening effects present in composites containing self-lubricant particles. Graphite codeposition had virtually no effect on the nickel matrix microstructure, and the inclusion of a softer material had no noticeable negative effect on hardness. Thus, Graphite-DC4 showed similar hardness (2.25 ± 0.20 GPa) values as Ni-DC4, and Dual SiC:Graphite-DC4 reported similar hardness values (2.77 ± 0.13 GPa) compared to single SiC60 10 g L⁻¹-DC4, both also showing similar SiC particles content (~1.5 vol.%).

The composites with MoS₂ particles, both as single and as dual SiC:MoS₂ dispersion mix, showed nanocrystalline matrix microstructures. As the result of the microstructure, the deposits hardness was increased by grain size strengthening despite the codeposition of soft MoS₂ particles. For instance, MoS₂-DC4/US showed microhardness values as high as 3.99 ± 0.49 GPa. Dual SiC:MoS₂-DC2/US benefited from both the nanocrystallinity of the matrix microstructure and a substantial codeposition of nanoSiC (~15 vol.%), resulting in extremely high hardness values of about 9.74 ± 0.64 GPa, which to the best of the author's knowledge, these hardness values have not been reported before in additive-free electroplated nickel-based composites.

4.4.2 Strengthening mechanisms

Supplement VII establishes the grain size strengthening of pure Ni produced using DC4, DC10 and PR, defining the Hall-Petch relationship for the electrodeposited nickel in the present work (Figure 28). Pure Ni samples produced using US agitation were excluded from the Hall-Petch relationship due to the additional strengthening effect caused by the work-hardening by ultrasounds [106]. Furthermore, because of the grain refinement caused by the ultrasonic agitation [60], these deposits showed further grain size strengthening in addition to the one drove by the electric current.

The Hall-Petch relationship represents the resistance of the microstructure to dislocation motions by the crystalline nature of the lattice (σ_0) and by the local stress needed at the grain boundary to transmit the plastic flow (k) [125]. In principle, these terms are expected to be similar on similar materials [126]. However, the anisotropy of electrodeposited metals makes the comparison of the Hall-Petch relationship between studies difficult. For instance, Godon et al. [127] observed changes in the Hall-Petch slope (k) of electrodeposited pure nickel due to the differences in grain shape and crystal orientation. Ni deposits dominated by the <100> crystal orientation showed similar k values (GPa $\mu\text{m}^{-1/2}$): ~ 2.1 [127] and ~ 2.2 [128], in agreement with the present study (2.54 ± 0.66). While, in deposits where <110> growth was dominant, the k value

was around 0.2 [127] and 0.1 [129], whereas in random deposits the values were: 0.7 [127] and 0.9 [130]. These results showed that considerations must be made in the study of the grain size strengthening on electrodeposited metals, accounting for the grain morphology and the reduction in the hardening effect depending on the texture of the nickel deposit. Indeed, when similar crystal orientations and grain shapes were observed in electrodeposited nickel, similar H_0 values (1.01 ± 0.41 GPa in the present study and 0.77 GPa by Miguel et al. [128]) were also observed.

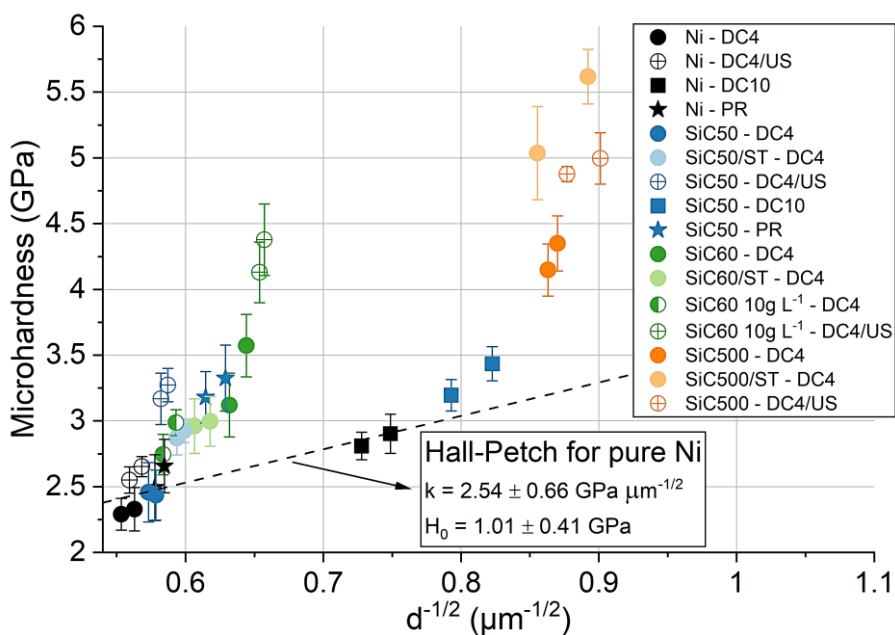


Figure 28: Microhardness (GPa) vs Grain average diameter ($\mu\text{m}^{-1/2}$) of the samples (two per condition). The Hall-Petch relationship for pure Ni deposits using DC4, DC10 and PR is indicated by the dashed line (Calculated in Supplement VII).

The codeposition of particles favoured additional hardening in the deposits, in combination with the one provided by the grain size strengthening driven by current density, by further grain refinement of the matrix (Figure 29). In some conditions, e.g. under stirring agitation, the grain refinement and particles codeposition showed an increasing linear trend. Additional strengthening effects were heavily influenced by the particles size, dispersion and

volume content. Thus, composites showed differences between hardness values, but the values were consistently above the Hall-Petch relationship for pure Ni (Figure 28).

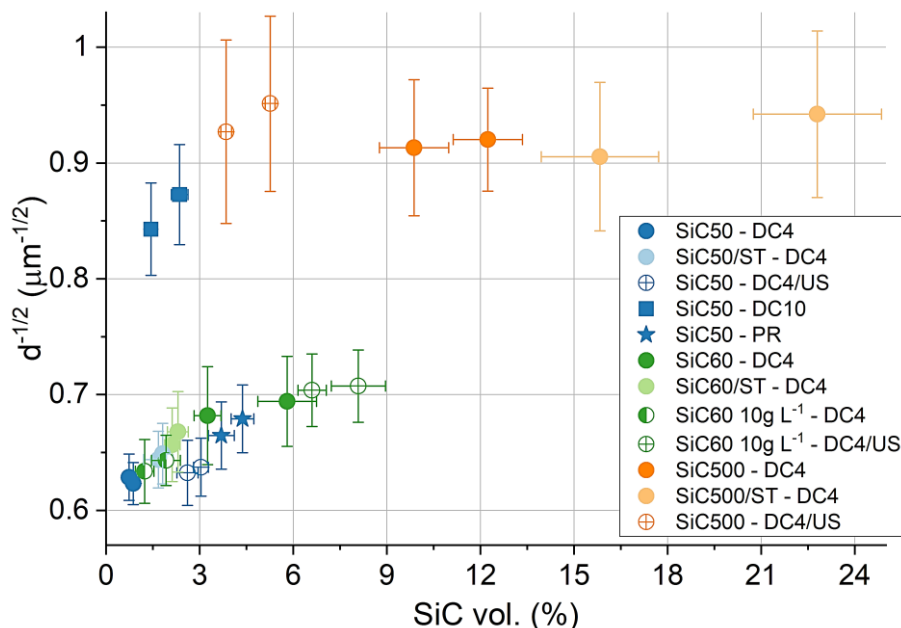


Figure 29: Grain average diameter ($\mu\text{m}^{-1/2}$) vs SiC volume content (%) of the electrodeposits (two per condition).

Supplement VII studies the contribution of each of the strengthening effects, considering their impact on the deposits hardness. In essence, the combination of the different strengthening mechanism present in the sample constituted the total hardness of the composite. Two methods were employed to account for their impact: the sums of contribution and the modified Clyne method [20] (Figure 30).

The sum of contribution (equation 4) considers each strengthening effect as single contributions, neglecting the effect of different mechanisms on each other. While the Clyne method (equation 5) considers the interdependencies between the particles codeposition and the strengthening factors, presenting the contribution of the different strengthening effects as the root of the sum of the squares of interrelated factors.

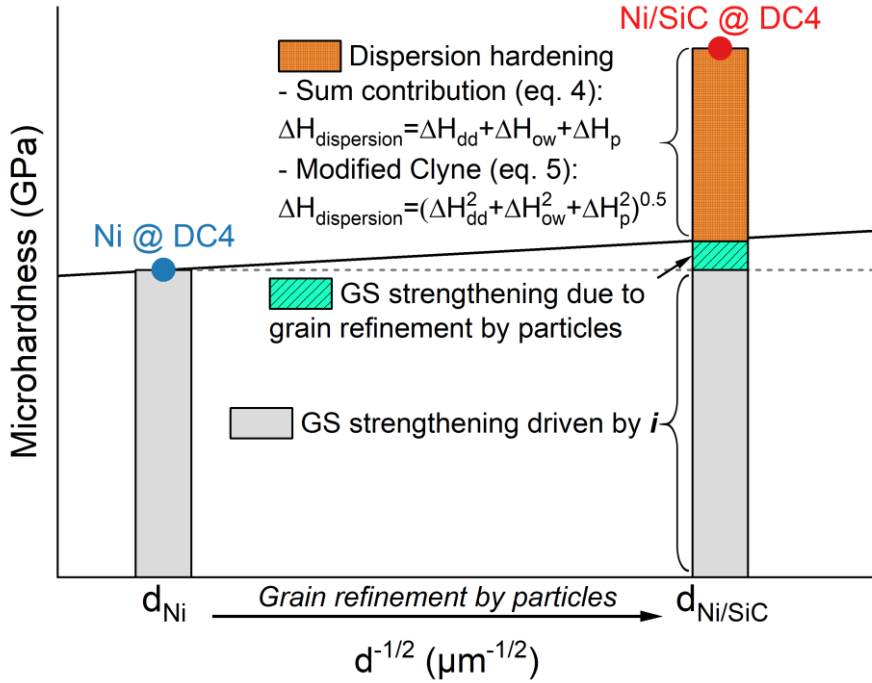


Figure 30: Total hardness of the electrodeposits as the combination of the strengthening effects. The black line indicates the Hall-Petch relationship.

Based on the considerations made in the methodology section: definition of the interdependency between strengthening effects and factors considered negligible in electrodeposited nanocomposites, the total hardness of the composites results from:

(i) The results of grain refinement from both particles codeposition [9], as observed in Figure 29, and current density [34]. Grain size strengthening shows separate components driven by particles content ($H_{\text{HP}(\text{SiC})}$) and driven by current density ($H_{\text{HP}(i)}$) (Figure 30). Furthermore, in the case of US agitation, additional grain refinement might be present [60], granting added grain size strengthening driven by ultrasound ($H_{\text{HP}(\text{US})}$).

(ii) Dislocation density strengthening due to ultrasounds ($H_{\text{dd}(\text{US})}$). For instance, pure Ni using US showed higher hardness as the result of strengthening by work-hardening [106]. The US cavitation during the electrocrystallisation placed the nickel under a strain rate deformation, causing an increase in the dislocation density,

leading to dislocation density strengthening ($H_{dd(US)}$) not present in deposits using stirring.

(iii) The particles codeposition: particles size, dispersion and volume content, affects greatly the Orowan strengthening [19] and on the hardening effect provided by particles, related by the composite rule of mixture [107,108].

Figure 31 shows samples produced using the same current density (DC4) representing different conditions by varying the codeposited particles size and content or agitation type. The hardness of the samples is depicted as the sum of contributions (equation 4) of each strengthening factors.

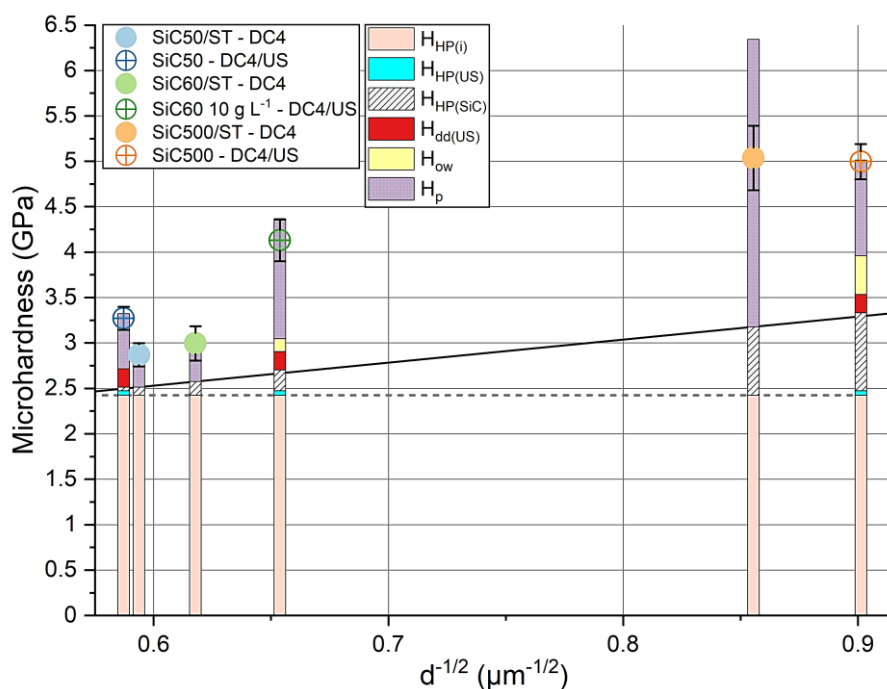


Figure 31: Microhardness vs Grain size diameter ($\mu\text{m}^{-1/2}$) of samples produced using the same current density (DC4) representing each condition. The solid black line indicates the Hall-Petch relationship (taken from Supplement VII).

The contribution of the grain size strengthening, driven by the current density (DC4), was approximated by the Hall-Petch relationship (equation 1). The value (~ 2.43 GPa) was considered as the base value ($H_{HP(I)}$) for the rest of the composites produced

using the same current density (DC4). The base value for composites produced with different current densities, e.g. DC10 or PR, was calculated using the same approach.

The grain size strengthening effect by ultrasonic agitation ($H_{HP(US)}$) was calculated by the difference between the base value ($H_{HP(i)}$) and the hardness value calculated by the Hall-Petch relationship for pure Ni-DC4/US, resulting in an approximate value of 0.05 GPa. This value was assumed constant for all of the composites. Likewise, the dislocation density strengthening due to ultrasonic agitation ($H_{dd(US)}$) was calculated by the difference between the value calculated by the Hall-Petch relationship for pure Ni-DC4/US and the experimental values, resulting in an approximate value of 0.2 GPa.

The grain refinement as the result of particles codeposition (Figure 29) granted added grain size strengthening ($H_{HP(SiC)}$) to the base value ($H_{HP(i)}$) of the SiC50/ST and SiC60/ST composites (Figure 31). Furthermore, the particles codeposition provided further hardening (H_p) calculated by the rule of mixture (equation 3). The Orowan strengthening in these deposits was considered negligible because of poor particles dispersion within the matrix. All nanocomposites produced using stirring showed an inter-particles distance of several micrometres (Figure 19a) and particles agglomeration (Figure 32a).

The US agitation improved the dispersion of particles within the matrix (Figure 19b) by breaking the agglomerations (Figure 32b). As a result, the inter-particles distance was reduced to about ~280 nm in SiC60/US. Therefore, in this deposit, Orowan strengthening (calculated by equation 2) was added in the total hardness of the composite (Figure 31), in addition to grain size strengthening as the result of refinement driven by current density ($H_{HP(i)}$), US agitation ($H_{HP(US)}$), and particles codeposition ($H_{HP(SiC)}$), the dislocation density strengthening by US agitation ($H_{dd(US)}$), and the second phase strengthening (H_p). In SiC50/US, the Orowan strengthening was negligible.

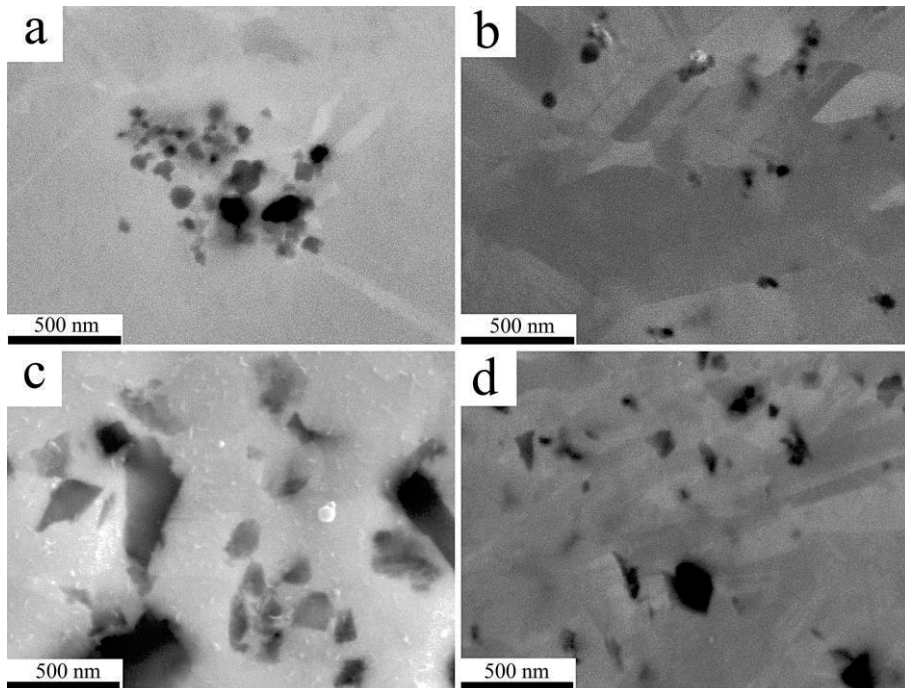


Figure 32: Cross-section SEM image of SiC60-DC4 using (a) stirring or (b) US agitation and SiC500-DC4 using (c) stirring or (d) US agitation.

The differences between codeposited particles size in SiC500/ST, ranging from micrometre sizes to nanometer (Figure 19c and Figure 32c), caused an overestimation of its hardness value (Figure 31) since particles sizes and agglomerations are not taken into account by the modelling equations. Sanaty-Zadeh et al. [20] also observed overestimation in the theoretical calculation of the hardness of composites, reporting a higher discrepancy in the sums of contribution method compared to the modified Clyne method.

The selective entrapment of particles in SiC500/US led to the codeposition of smaller particles (~ 250 nm in average diameter size), uniformly dispersed within the matrix (Figure 19d and Figure 32d) with an inter-particles spacing of around ~ 122 nm. Thus, the Orowan strengthening was more effective in SiC500/US than in SiC60/US because of the closer distance between particles. Although SiC500/US showed lower content of particles compared to SiC500/ST, both showed similar hardness values due to the

additional strengthening factors present in the composite produced using US agitation, thus, proving that increasing particles content in composite does not always guarantee an improvement in properties.

Supplement VII studies the comparison between the hardness measured experimentally for all pure Ni and Ni/SiC deposits and the hardness approximated by the sum of contributions method and the modified Clyne method. Table 8 shows a summary of this comparison, indicating only the deposits presented in Figure 31.

The hardness values approximated by the modelling methods are in good agreement with experimental values, with the exception of the composites containing SiC500. The sums of contribution showed a higher discrepancy than the modified Clyne method, also observed by Sanaty-Zadeh et al. [20]. SiC500-DC4/US hardness values were underestimated, possibly due to an unaccounted strengthening resulting from changes in the crystal structure, i.e. dislocations, due to variations in the electric current field by the particles codeposition, or by modifying the crystal structure by depositing well-distributed particles and with an approximate size (~ 250 nm in mean diameter size) of one-fifth of the grain size (~ 1300 nm in mean diameter size).

Table 8: Particles content (vol.%), microhardness (GPa) of the composites approximated by the sum of contribution method (equation 4) and the modified Clyne method (equation 5), and microhardness (GPa) measured experimentally of the deposits of Figure 31.

Sample	SiC vol.%	H _c (GPa) (eq. 4)	H _c (GPa) (eq. 5)	H _c (GPa) (exp)
SiC50/ST- DC4	1.67 ± 0.47	2.85	2.77	2.87 ± 0.13
	1.81 ± 0.12	2.89	2.80	2.93 ± 0.09
SiC50- DC4/US	2.61 ± 0.34	3.23	3.19	3.17 ± 0.20
	3.04 ± 0.24	3.33	3.28	3.27 ± 0.13

Table 8 (continued): Particles content (vol.%), microhardness (GPa) of the composites approximated by the sum of contribution method (equation 4) and the modified Clyne method (equation 5), and microhardness (GPa) measured experimentally of the deposits of Figure 31.

Sample	SiC vol.%	H _c (GPa) (eq. 4)	H _c (GPa) (eq. 5)	H _c (GPa) (exp)
SiC60/ST-	2.12 ± 0.25	2.97	2.87	2.96 ± 0.21
DC4	2.30 ± 0.33	3.04	2.91	3.00 ± 0.19
SiC60	6.60 ± 0.45	4.36	4.01	4.13 ± 0.23
10gL ⁻¹ - DC4/US	8.08 ± 0.87	4.64	4.30	4.38 ± 0.27
SiC500/ST-	22.80 ± 2.05	7.83	7.06	5.62 ± 0.21
DC4	15.83 ± 1.88	6.34	5.68	5.04 ± 0.35
SiC500-	5.26 ± 0.16	5.00	4.09	5.00 ± 0.19
DC4/US	3.85 ± 0.17	4.66	3.85	4.88 ± 0.10

4.4.3 Wear behaviour

Table 9 shows the average coefficients of friction (COF) and the volumetric wear factor of the deposits, summarising the results from Supplements VI and VII. The friction coefficient between the surface and the counter material depends on both adhesive and deformation forces [131]. In cases of high friction between touching materials, i.e. surfaces resisting the motion force, ploughing and pile-up of the material might occur [132], resulting in debris in the wear track. Ductile materials, such as nickel, are susceptible to this type of material detachment, i.e. adhesive wear. The coatings with better wear resistance endured the passing counter material, resulting in less worn material volume (Figure 33).

Table 9: Summary of the friction coefficient (COF) and volumetric wear factor $\times 10^{-4}$ ($\text{mm}^3 \text{Nm}^{-1}$) of the deposits presented in Supplements V, VI and VII.

Sample	COF	Volumetric wear factor $\times 10^{-4}$ ($\text{mm}^3 \text{Nm}^{-1}$)
Ni-DC4	0.15 ± 0.11	80 ± 7
Ni-DC/US	0.15 ± 0.13	62 ± 6
SiC50-DC4	0.16 ± 0.13	75 ± 6
SiC50/ST-DC4	0.20 ± 0.14	59 ± 5
SiC50-DC4/US	0.22 ± 0.18	49 ± 3
SiC60-DC4	0.29 ± 0.15	41 ± 3
SiC60/ST-DC4	0.21 ± 0.15	60 ± 6
SiC60 10gL^{-1} -DC4	0.22 ± 0.10	57 ± 4
SiC60 10gL^{-1} -DC4/US	0.37 ± 0.20	34 ± 3
SiC500-DC4	0.40 ± 0.10	35 ± 2
SiC500/ST-DC4	0.44 ± 0.10	30 ± 2
SiC500-DC4/US	0.29 ± 0.08	13 ± 2
Graphite-DC4	0.14 ± 0.09	70 ± 5
Dual SiC:Graphite-DC4	0.19 ± 0.09	53 ± 3
MoS ₂ -DC4/US	0.06 ± 0.02	11 ± 2
Dual SiC:MoS ₂ -DC2/US	0.08 ± 0.05	5 ± 2

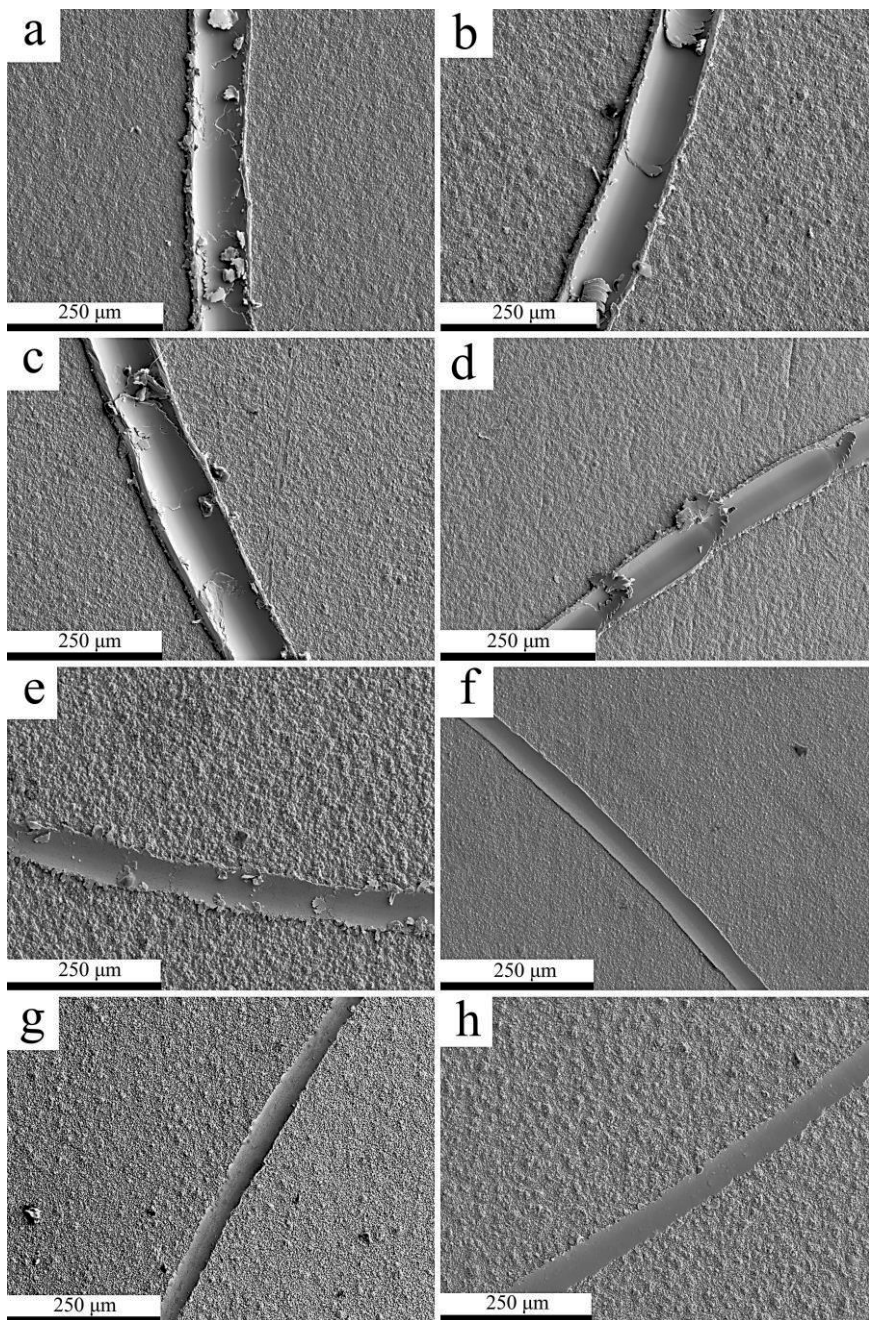


Figure 33: SEM image of the wear tracks: (a) Ni-DC4, (b) Ni-DC4(US), (c) SiC60-DC4, (d) SiC60 10gL⁻¹-DC4/US, (e) SiC500-DC4, (f) SiC500-DC4/US, (g) MoS₂ - DC4/US, (h) Dual SiC:MoS₂ - DC2/US.

The decrease in the wear volume was connected to the hardness of the deposit. Previous studies of SiC-based nickel composites [133–137] also described a decrease in wear with the increase of hardness, showing the established indirect relationship between hardness and wear resistance [8,138,139].

All pure Ni deposits showed somewhat similar COF, ranging between 0.1 and 0.2. 'Stick-slip' and material detachment, i.e. debris due to ploughing and pile-up during the tests, were visible in the wear tracks (Figure 33a and b). The friction probe recorded these adhesive events, showing an increase in the COF at every event [140], thus, scattering the value. Ni-DC4(US) exhibited better wear resistance than pure Ni deposit using stirring on account of the higher hardness.

The addition of nanoparticles increased the deposits hardness and thus reduced the wear rate of the coating. The wear tracks in the nanocomposites were comparable in appearance to pure Ni, showing similar ploughing and piling-up (Figure 33c and d). However, the particles codeposition increased the COF, ranging instead between 0.2 and 0.3. The increase in friction might be due to particles increasing the number of obstacles against the motion force, causing adhesive events. SiC60 10 g L⁻¹-DC4/US (Figure 33d) showed flake-like debris with partial detachment, recognised as large adhesive events, and thus, the COF in this sample was raised considerable (Table 9). Gyftou et al. [133] also reported increased friction, up to ~0.35, after SiC addition in nickel. Zhou et al. [136] and Benea et al. [137] reported a decrease in COF for nickel after SiC codeposition from 0.8 and 0.4, down to 0.2 and 0.3, respectively, although these Ni-SiC COF values were similar to ones reported in the present research. The minor differences between studies might be due to the nickel microstructure and surface morphology, and roughness. The present study and Gyftou et al. [133] observed a pyramidal-shaped surface topography in Ni-SiC, while Zhou et al. [136] and Benea et al. [137] showed globular structures.

The composites containing SiC500 shows the drawback of using submicron particles as the reinforcer phase in composites. The codeposition of large particles, in some cases in the micrometre

size range (Figure 19c), presented a larger opposing force against the passing counter material, increasing the COF in SiC500-DC4 and SiC500/ST-DC4. Lanzutti et al. [134] also observed an increase in COF due to the incorporation of micro-particles. The lack of these larger particles in SiC500-DC/US as the result of US agitation (Figure 19d) led to COF values comparable to the nanocomposites (Table 9).

The wear tracks of SiC500-DC4 and SiC500/ST-DC4 showed visible material debris but minor material pile-up (Figure 33e), indicating a change in the type of wear from adhesive to abrasive. Despite the high hardness reported in these deposits, the worn material volume was similar to the softer deposits, e.g. SiC60-DC4, due to wear by third-body abrasion (detached large particles), typical in abrasive wear. SiC500-DC4/US wear tracks (Figure 33f) showed little to no material pile-up or visible material debris. These deposits also reported low wear rates, in agreement with the reported high hardness and the codeposition of smaller particles.

Supplement V studies the codeposition of graphite for self-lubrication. Graphite-DC4 showed a similar COF value and a wear rate comparable to Ni-DC4. Therefore, no significant self-lubrication capability by the codeposited graphite was visible due to the low content. Likewise, Dual SiC:Graphite-DC4 reported a comparable COF value and wear rate to the ones reported in single-SiC composites showing no improvement by the presence of graphite as dual dispersion mix. Supplement V shows the wear tracks of these coatings.

Contrary to the codeposition of SiC and graphite, the addition of MoS₂ as single-particles or as a dual SiC:MoS₂ dispersion provided a self-lubrication capability to the coatings, causing a significant COF decrease (Table 9). Previous studies [63,117–119,124] also reported a similar decrease in friction by codepositing MoS₂ in a Ni-based matrix. Furthermore, the wear rate was significantly decreased in MoS₂ – DC4/US thanks to the combined effect of self-lubrication and high hardness. The wear track (Figure 33g) showed a smooth sliding by the counter material with no debris in the wear tracks and no signs of ploughing or piling-up.

The synergies of combining SiC and MoS₂ as dual dispersion mix were visible in Dual SiC:MoS₂ – DC2/US, showing the lowest wear rate among the composites (Table 9). The codeposition of MoS₂ provided self-lubrication, and the nanocrystalline structures and high SiC incorporation caused a significant increase in hardness. The wear track in this coating was nearly visible with no pile-up (Figure 33h).

4.4.3.1 Significance of the H/E ratio

Leyland et al. [141] proposed that the ratio between microhardness and elastic modulus is suitable for predicting wear resistance in a nanocomposite coating. Maximising the coating hardness by grain refinement or particles codeposition can be beneficial in terms of increasing the resistance to plastic deformation. Leyland et al. argued that a high material stiffness could be prejudicial to the coating, especially if there is a mismatch between the Young's modulus (E) value of the coating and the substrate. Low E values may help improve strain tolerance and permit limited cracking, thus exposing the reinforcer phase, particularly if they are self-lubricants. Therefore, the authors determined that a high ratio (H/E), i.e. elastic strain to failure, is considered an indicator of a durable material against wear. Góral et al. [142] also observed the same relation in nickel-based composites between H/E ratios and wear resistance.

Figure 34 shows the relation between the H/E_r ratio and wear rate, showing an evident link between high ratios and a lower volume of material worn. As the hardness of the deposits was increased by changes in the matrix microstructure and by the codeposition of particles, the resistance to plastic deformation was improved. This shows the critical role of promoting additional hardening effects in the composites by controlling how particles are codeposited. For instance, SiC60-DC4/US and SiC500-DC4/US showed that the added strengthening effects in these deposits increased the wear resistance.

Lastly, the analysis of the H/E_r ratio in single MoS₂ and dual SiC:MoS₂ proved the benefits of a self-lubrication capability and a

nanocrystalline matrix microstructure. Dual SiC:MoS₂ wear behaviour highlighted the potential of dual nanocomposites composites designed for wear resistance.

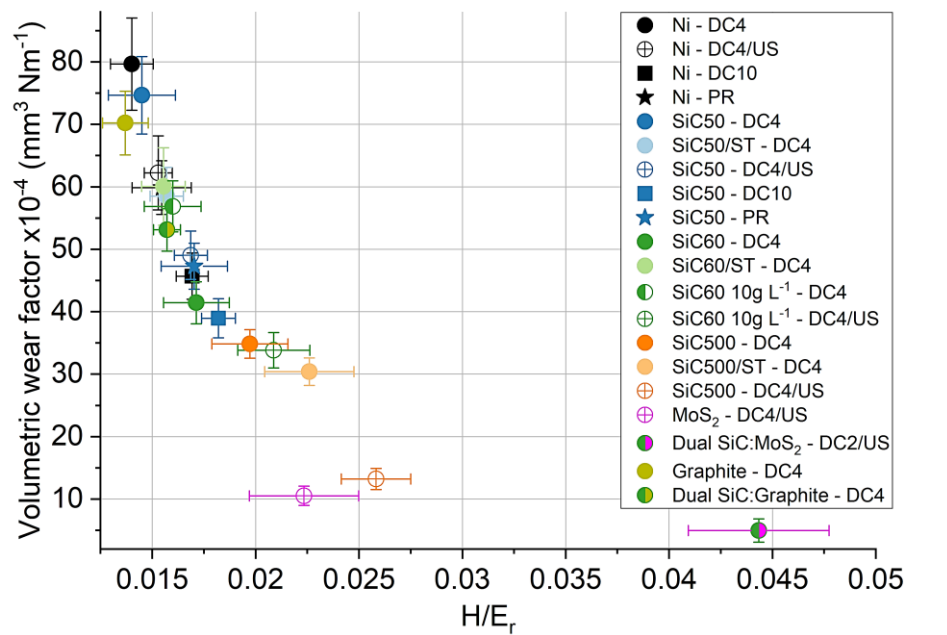


Figure 34: Elastic strain to failure, i.e. H/E_r ratio, vs the volumetric wear factor x10⁻⁴ (mm³ Nm⁻¹) of the deposits for each condition (averaged from two samples).

CONCLUSIONS

CHAPTER INTRODUCTION

In this chapter, the conclusions from the present work have been summarized.

The present work provided a better understanding of the factors that affect the codeposition of particles in the electrodeposition of nanocomposite coatings. The findings presented by this study were of significant importance as they supported new methods to ensure the reproducibility of the process. This work identified the influence of codepositing particles in the electrocrystallisation of the metal, correlating both elements to the strengthening effects present in electrodeposited nanocomposites. The hardness of the material was expressed as the contribution and combination of different strengthening mechanisms, linking the hardening to the wear resistance of the coating. The following main conclusions are highlighted:

(i) The surface state of particles must be considered as a variable in the electrodeposition of composites. Differences between surface states caused unpredictable particles-electrolyte interactions, even in particles with the same chemistry and similar size. The surface of the particles controls their response when added to a solution, finding that:

- SiC particles deriving from different supplier or production routes showed different ζ -potential values, despite the same chemical composition.
- The titration revealed different pH buffering capability of the SiC powders, varying with supplier or production routes, revealing a non-inert behaviour.

The proposed surface treatment based on nitric acid provided a method to control the variable of the surface state, bringing particles to a similar response. Composites produced with surface-treated nanopowders showed reproducible results displaying similar matrix microstructure, codeposition rates, hardness values and wear rates, independently of the batch, supplier, or production route.

(ii) A new experimental electrodeposition method based on pulse-reverse was developed during this study. The pulse-reverse waveform was adapted to the particles size by depositing a metal thickness equivalent to the particles average diameter during the cathodic cycle and stripping half during the anodic cycle. This pulse-reverse method increased the particles codeposition rate compared to direct current by at least a factor of four times, independently of the electrolyte formulation or cell geometry. Furthermore, the method was further optimised by controlling the anodic time, promoting the particles residence time, increasing the particles content and thus the hardness of the deposit.

(iii) Particles codeposition was proven to influence the electrocrystallisation of nickel. It was found that:

- The preferential $\langle 100 \rangle$ crystal growth intensity observed in pure nickel was reduced as particles codeposition caused an increase of nickel growth inhibitors, e.g. H_2 , H_{ads} and $Ni(OH)_2$.
- The matrix microstructure was modified from one dominated by large columnar grains to an equiaxial-type microstructure due to particles codeposition.
- The grain size of the matrix microstructure was reduced as nanoparticles content was increased.

(iv) The total hardness of the deposits was relative to the contribution and combination of different strengthening effects: grain size refinement, dislocation density, Orowan and particles incorporation.

Both the process parameters and particles codeposition, i.e. particles size, dispersion and content, heavily influenced the magnitude of the strengthening factors, showing that:

- Three distinct elements drove the grain size strengthening since the current density, US agitation and particles codeposition caused grain refinement.
- Dislocation density strengthening was linked to work-hardening due to US cavitation.
- Orowan strengthening was negligible in the composites produced using stirring due to micrometre inter-particles distances. In contrast, US agitation caused particles to codeposit uniformly dispersed within the matrix and having smaller spacing, inducing Orowan strengthening.

The prediction of the final coating hardness by the sum of contribution and the Clyne method, based on contribution and combination of different strengthening mechanisms, showed good agreement with the experimental data.

(v) The wear behaviour of the composites was directly linked to the hardening effects present in the material. The wear rate of the coating decreased with the hardness increase. The codeposition of micrometre size particles increased the wear rate due to third-body abrasion.

(vi) A novel dual dispersion coating was produced by a SiC:MoS₂ powder mix. A synergistic effect was observed when particles codeposited together, MoS₂ particles were smaller in size and more distributed within the matrix, and SiC codeposited at higher rates. The dual nanocomposite showed all the combined advantages observed individually in the single particles composites, a high hardness due to SiC incorporation and a nanocrystalline matrix due to MoS₂ codeposition, coupled with a self-lubrication capability, resulting in a nanocomposite coating with superior wear resistance.

FUTURE WORK

CHAPTER INTRODUCTION

In this chapter, some aspects of how to further advance future work are presented.

There are various elements related to the work described in this thesis that can be considered as aspects to complement and progress further in future work:

Codeposition by an adapted pulse-reverse waveform

Futures studies should test the concept of the particles residence time as the controlling parameter of the codeposition on different particles and bath chemistry. A pulse-reverse waveform adapted to the particles size in suspension instead of their average size as powders should also be considered.

Improving the study of the strengthening effects

Future studies using TEM analysis should verify the increase of dislocations in the crystal structure due to US agitation, comparing the results to ones of pure metal deposited by stirring. Similarly, TEM analysis should also be employed to study the crystal structure around the codeposited particles. The electric current field, which acts as the driving force for the electrocrystallisation of the metal, might be modified by the presence of the particles, provoking changes in the crystal structure. Thus, other strengthening effects might be present in the metal matrix.

Dual dispersion coatings

Dual SiC:MoS₂ composite showed an outstanding wear resistance due to the combination of high hardness and self-lubrication. This composite and the other examples from literature highlighted dual

particles mixes as a promising field to progress in the electrodeposition of composite coatings. Different particles, mix ratios, and additives typically used in industrial baths should be extensively studied in order to design an optimal multi-material composite coating.

Influence of the rest of the parameters

Some of the parameters that were kept constant in this thesis can also influence codeposition. For instance, the cell and electrode geometry and the hydrodynamics conditions are critical in the particles codeposition and should be considered in future studies regarding the industrial scale-up.

REFERENCES

1. Callister, W.D.; Rethwisch, D.G. *Materials science and engineering*, 9. ed., SI version; Wiley: Hoboken, NJ, 2015, ISBN 9781118319222.
2. Ashby, M.F. *Materials selection in mechanical design*, 4 edition; Elsevier/Butterworth-Heinemann: Amsterdam, 2011, ISBN 9781856176637.
3. European Chemicals Agency. Substances restricted under REACH. Available online: <https://echa.europa.eu/substances-restricted-under-reach> (accessed on 2 March 2019).
4. Campbell, F.C. *Structural composite materials*; ASM International: Materials Park, Ohio, 2010, ISBN 9781615030378.
5. Haghshenas, M. Metal–Matrix Composites. In *Hard Coatings on Cutting Tools and Surface Finish. Reference Module in Materials Science and Materials Engineering*; Caliskan, H.P.P.K.C., Ed.; Elsevier Science Direct, 2016, ISBN 9780128035818.
6. Miracle, D. Metal matrix composites – From science to technological significance. *Compos. Sci. Technol.* **2005**, *65*, 2526–2540, doi:10.1016/j.compscitech.2005.05.027.
7. Gyftou, P.; Pavlatou, E.A.; Spyrellis, N.; Hatzilyberis, K.S. Nickel Matrix Composite Coatings: Application in Textile Machinery and Evaluation of Cotton Products Quality. *Trans. IMF* **2000**, *78*, 223–226, doi:10.1080/00202967.2000.11871345.
8. Kerr, C.; Barker, D.; Walsh, F.; Archer, J. The electrodeposition of composite coatings based on metal matrix-included particle deposits. *Trans. IMF* **2000**, *78*, 171–178, doi:10.1080/00202967.2000.11871333.
9. Low, C.T.J.; Wills, R.G.A.; Walsh, F.C. Electrodeposition of composite coatings containing nanoparticles in a metal deposit. *Surf. Coat. Technol.* **2006**, *201*, 371–383, doi:10.1016/j.surfcoat.2005.11.123.
10. Karimzadeh, A.; Aliofkhazraei, M.; Walsh, F.C. A review of electrodeposited Ni-Co alloy and composite coatings: Microstructure, properties and applications. *Surf. Coat. Technol.* **2019**, *372*, 463–498, doi:10.1016/j.surfcoat.2019.04.079.
11. Torabinejad, V.; Aliofkhazraei, M.; Assareh, S.; Allahyarzadeh, M.H.; Rouhaghdam, A.S. Electrodeposition of Ni-Fe alloys,

- composites, and nano coatings—A review. *J. Alloys Compd.* **2017**, *691*, 841–859, doi:10.1016/j.jallcom.2016.08.329.
12. Vaezi, M.R.; Sadrnezhaad, S.K.; Nikzad, L. Electrodeposition of Ni–SiC nano-composite coatings and evaluation of wear and corrosion resistance and electroplating characteristics. *Colloids Surf. A Physicochem. Eng. Asp.* **2008**, *315*, 176–182, doi:10.1016/j.colsurfa.2007.07.027.
 13. Thiemig, D.; Bund, A. Characterization of electrodeposited Ni–TiO₂ nanocomposite coatings. *Surf. Coat. Technol.* **2008**, *202*, 2976–2984, doi:10.1016/j.surfcoat.2007.10.035.
 14. Lampke, T.; Leopold, A.; Dietrich, D.; Alisch, G.; Wielage, B. Correlation between structure and corrosion behaviour of nickel dispersion coatings containing ceramic particles of different sizes. *Surf. Coat. Technol.* **2006**, *201*, 3510–3517, doi:10.1016/j.surfcoat.2006.08.073.
 15. Zanella, C.; Lekka, M.; Bonora, P.L. Influence of the particle size on the mechanical and electrochemical behaviour of micro- and nano-nickel matrix composite coatings. *J. Appl. Electrochem.* **2009**, *39*, 31–38, doi:10.1007/s10800-008-9635-y.
 16. Roylance, D. *Mechanics of materials*; Wiley: Chichester, 1996, ISBN 0471593990.
 17. Ceschini, L.; Dahle, A.; Gupta, M.; Jarfors, A.E.W.; Jayalakshmi, S.; Morri, A.; Rotundo, F.; Toschi, S.; Singh, R.A. *Aluminum and magnesium metal matrix nanocomposites*; Springer: Singapore, 2017, ISBN 9789811026812.
 18. Zhang, Z.; Chen, D.L. Consideration of Orowan strengthening effect in particulate-reinforced metal matrix nanocomposites: A model for predicting their yield strength. *Scripta Mater.* **2006**, *54*, 1321–1326, doi:10.1016/j.scriptamat.2005.12.017.
 19. Zhang, Z.; Chen, D.L. Contribution of Orowan strengthening effect in particulate-reinforced metal matrix nanocomposites. *Mater. Sci. Eng. A* **2008**, *483–484*, 148–152, doi:10.1016/j.msea.2006.10.184.
 20. Sanaty-Zadeh, A.; Rohatgi, P.K. Comparison between current models for the strength of particulate-reinforced metal matrix nanocomposites with emphasis on consideration of Hall–Petch effect. *Mater. Sci. Eng. A* **2012**, *531*, 112–118, doi:10.1016/j.msea.2011.10.043.

21. Gamburg, Y.D.; Zangari, G. *Theory and Practice of Metal Electrodeposition*; Springer Science+Business Media LLC: New York, NY, 2011, ISBN 9781441996688.
22. Kobayashi, K.; Chiba, A.; Minami, N. Effects of ultrasound on both electrolytic and electroless nickel depositions. *Ultrason.* **2000**, *38*, 676–681, doi:10.1016/S0041-624X(99)00215-2.
23. Kolonits, T.; Jenei, P.; Tóth, B.G.; Czigány, Z.; Gubicza, J.; Péter, L.; Bakonyi, I. Characterization of Defect Structure in Electrodeposited Nanocrystalline Ni Films. *J. Electrochem. Soc.* **2016**, *163*, D107–D114, doi:10.1149/2.0911603jes.
24. Stappers, L.; Fransaer, J. Growth of Metal around Particles during Electrodeposition. *J. Electrochem. Soc.* **2006**, *153*, C472, doi:10.1149/1.2198090.
25. Budevski, E.; Staikov, G.; Lorenz, W.J. Electrocrystallization: Nucleation and growth phenomena. *Electrochim. Acta* **2000**, *45*, 2559–2574, doi:10.1016/S0013-4686(00)00353-4.
26. Amblard, J.; Epelboin, I.; Froment, M.; Maurin, G. Inhibition and nickel electrocrystallization. *J. Appl. Electrochem.* **1979**, *9*, 233–242, doi:10.1007/BF00616093.
27. Winand, R. Electrocrystallization - theory and applications. *Hydrometall.* **1992**, *29*, 567–598, doi:10.1016/0304-386X(92)90033-V.
28. Raghunathan, K.; Weil, R. The effects of some plating variables on the structure of thin nickel electrodeposits. *Surf. Technol.* **1980**, *10*, 331–342.
29. Vincenzo, A.; Cavallotti, P.L. Structure and electrokinetic study of nickel electrodeposition. *Russ. J. Electrochem* **2008**, *44*, 716–727, doi:10.1134/s1023193508060128.
30. Mason, T.J.; Coble, A.J.; Graves, J.E.; Morgan, D. New evidence for the inverse dependence of mechanical and chemical effects on the frequency of ultrasound. *Ultrason. Sonochem.* **2011**, *18*, 226–230, doi:10.1016/j.ultsonch.2010.05.008.
31. *Nickel and Chromium Plating (Third Edition)*; Dennis, J.K.; Such, T., Eds., Third Edition; Woodhead Publishing, 1993, ISBN 978-1-85573-081-6.
32. Kollia, C.; Spyrellis, N.; Amblard, J.; Froment, M.; Maurin, G. Nickel plating by pulse electrolysis: Textural and microstructural modifications due to adsorption/desorption phenomena. *J. Appl. Electrochem.* **1990**, *20*, 1025–1032, doi:10.1007/BF01019584.

33. Watts, O.P. Rapid nickel plating. *Trans. Am. Electrochem. Soc.* **1916**, 29, 395–403.
34. Rashidi, A.M.; Amadeh, A. The effect of current density on the grain size of electrodeposited nanocrystalline nickel coatings. *Surf. Coat. Technol.* **2008**, 202, 3772–3776, doi:10.1016/j.surfcoat.2008.01.018.
35. Vittal, R.; Gomathi, H.; Kim, K.-J. Beneficial role of surfactants in electrochemistry and in the modification of electrodes. *Adv. Colloid Interf. Sci.* **2006**, 119, 55–68, doi:10.1016/j.cis.2005.09.004.
36. Faraday, M. Experimental Researches in Electricity. Seventh Series. *Philos. Trans. R. Soc. London* **1834**, 124, 77–122, doi:10.1098/rstl.1834.0008.
37. Crouch, P.C.; Hendricksen, H.V. Current efficiency on Watts baths. *Trans. IMF* **1983**, 61, 133–140.
38. Chandrasekar, M.S.; Pushpavanam, M. Pulse and pulse reverse plating—Conceptual, advantages and applications. *Electrochim. Acta* **2008**, 53, 3313–3322, doi:10.1016/j.electacta.2007.11.054.
39. Walsh, F.C.; Low, C.T.J.; Bello, J.O. Influence of surfactants on electrodeposition of a Ni-nanoparticulate SiC composite coating. *Transactions of the IMF* **2015**, 93, 147–156, doi:10.1179/0020296715Z.0000000000237.
40. Hovestad, A.; Janssen, L.J.J. Electrochemical codeposition of inert particles in a metallic matrix. *J. Appl. Electrochem.* **1995**, 25, 519–527, doi:10.1007/BF00573209.
41. Bhattacharjee, S. DLS and zeta potential - What they are and what they are not? *J. Control. Release* **2016**, 235, 337–351, doi:10.1016/j.jconrel.2016.06.017.
42. Lari Baghal, S.M.; Amadeh, A.; Heydarzadeh Sohi, M.; Hadavi, S. The effect of SDS surfactant on tensile properties of electrodeposited Ni–Co/SiC nanocomposites. *Mater. Sci. Eng. A* **2013**, 559, 583–590, doi:10.1016/j.msea.2012.08.145.
43. Kılıç, F.; Gül, H.; Aslan, S.; Alp, A.; Akbulut, H. Effect of CTAB concentration in the electrolyte on the tribological properties of nanoparticle SiC reinforced Ni metal matrix composite (MMC) coatings produced by electrodeposition. *Colloids Surf. A Physicochem. Eng. Asp.* **2013**, 419, 53–60, doi:10.1016/j.colsurfa.2012.11.048.
44. Wang, S.-C.; Wei, W.-C.J. Kinetics of electroplating process of nano-sized ceramic particle/Ni composite. *Mater. Chem. Phys.* **2001**, 78, 574–580, doi:10.1016/S0254-0584(01)00564-8.

45. Hashiba, M.; Okamoto, H.; Nurishi, Y.; Hiramatsu, K. The zeta-potential measurement for concentrated aqueous suspension by improved electrophoretic mass transport apparatus - application to Al_2O_3 , ZrO_3 and SiC suspensions. *J. Mater. Sci.* **1988**, *23*, 2893–2896, doi:10.1007/BF00547464.
46. Yao, Y.; Yao, S.; Zhang, L.; Wang, H. Electrodeposition and mechanical and corrosion resistance properties of Ni–W/SiC nanocomposite coatings. *Mater. Lett.* **2007**, *61*, 67–70, doi:10.1016/j.matlet.2006.04.007.
47. Zoikis-Karathanasis, A.; Pavlatou, E.A.; Spyrellis, N. Pulse electrodeposition of Ni–P matrix composite coatings reinforced by SiC particles. *J. Alloys Compd.* **2010**, *494*, 396–403, doi:10.1016/j.jallcom.2010.01.057.
48. Stroumbouli, M.; Gyftou, P.; Pavlatou, E.A.; Spyrellis, N. Codeposition of ultrafine WC particles in Ni matrix composite electrocoatings. *Surf. Coat. Technol.* **2005**, *195*, 325–332, doi:10.1016/j.surfcoat.2004.06.034.
49. Lee, H.-K.; Lee, H.-Y.; Jeon, J.-M. Codeposition of micro- and nano-sized SiC particles in the nickel matrix composite coatings obtained by electroplating. *Surf. Coat. Technol.* **2007**, *201*, 4711–4717, doi:10.1016/j.surfcoat.2006.10.004.
50. Tudela, I.; Zhang, Y.; Pal, M.; Kerr, I.; Cobley, A.J. Ultrasound-assisted electrodeposition of composite coatings with particles. *Surf. Coat. Technol.* **2014**, *259*, 363–373, doi:10.1016/j.surfcoat.2014.06.023.
51. Mason, T.J.; Lorimer, J.P.; Walton, D.J. Sonochemistry. *Ultrason.* **1990**, *28*, 333–337, doi:10.1016/0041-624X(90)90041-L.
52. Brennen, C.E. *Cavitation and bubble dynamics*; Oxford University Press: New York, Oxford, 1995, ISBN 0195094093.
53. Zanella, C.; Lekka, M.; Rossi, S.; Deflorian, F. Study of the influence of sonication during the electrodeposition of nickel matrix nanocomposite coatings on the protective properties. *Corros. Rev.* **2011**, *29*, 253–260, doi:10.1515/CORRREV.2011.005.
54. Zanella, C.; Lekka, M.; Bonora, P.L. Effect of ultrasound vibration during electrodeposition of Ni–SiC nanocomposite coatings. *Surf. Eng.* **2013**, *26*, 511–518, doi:10.1179/174329409X438961.
55. Dietrich, D.; Scharf, I.; Nickel, D.; Shi, L.; Grund, T.; Lampke, T. Ultrasound technique as a tool for high-rate incorporation of Al_2O_3

- in NiCo layers. *J. Solid State Electrochem.* **2011**, *15*, 1041–1048, doi:10.1007/s10008-011-1348-1.
56. García-Lecina, E.; García-Urrutia, I.; Díez, J.A.; Morgiel, J.; Indyka, P. A comparative study of the effect of mechanical and ultrasound agitation on the properties of electrodeposited Ni/Al₂O₃ nanocomposite coatings. *Surf. Coat. Technol.* **2012**, *206*, 2998–3005, doi:10.1016/j.surfcoat.2011.12.037.
 57. Zheng, H.-Y.; An, M.-Z. Electrodeposition of Zn–Ni–Al₂O₃ nanocomposite coatings under ultrasound conditions. *J. Alloys Compd.* **2008**, *459*, 548–552, doi:10.1016/j.jallcom.2007.05.043.
 58. García-Lecina, E.; García-Urrutia, I.; Díez, J.A.; Fornell, J.; Pellicer, E.; Sort, J. Codeposition of inorganic fullerene-like WS₂ nanoparticles in an electrodeposited nickel matrix under the influence of ultrasonic agitation. *Electrochim. Acta* **2013**, *114*, 859–867, doi:10.1016/j.electacta.2013.04.088.
 59. Graves, J.E.; Sugden, M.; Litchfield, R.E.; Hutt, D.A.; Mason, T.J.; Cobley, A.J. Ultrasound assisted dispersal of a copper nanopowder for electroless copper activation. *Ultrason. Sonochem.* **2016**, *29*, 428–438, doi:10.1016/j.ultsonch.2015.10.016.
 60. Tudela, I.; Zhang, Y.; Pal, M.; Kerr, I.; Mason, T.J.; Cobley, A.J. Ultrasound-assisted electrodeposition of nickel: Effect of ultrasonic power on the characteristics of thin coatings. *Surf. Coat. Technol.* **2015**, *264*, 49–59, doi:10.1016/j.surfcoat.2015.01.020.
 61. Walsh, F.C.; Ponce de Leon, C. A review of the electrodeposition of metal matrix composite coatings by inclusion of particles in a metal layer: an established and diversifying technology. *Trans. IMF* **2014**, *92*, 83–98, doi:10.1179/0020296713z.000000000161.
 62. Li, Z.; Wang, J.; Lu, J.; Meng, J. Tribological characteristics of electroless Ni–P–MoS₂ composite coatings at elevated temperatures. *Appl. Surf. Sci.* **2013**, *264*, 516–521, doi:10.1016/j.apsusc.2012.10.055.
 63. He, Y.; Wang, S.C.; Walsh, F.C.; Chiu, Y.-L.; Reed, P. Self-lubricating Ni–P–MoS₂ composite coatings. *Surf. Coat. Technol.* **2016**, *307*, 926–934, doi:10.1016/j.surfcoat.2016.09.078.
 64. Bakhit, B.; Akbari, A. Effect of particle size and co-deposition technique on hardness and corrosion properties of Ni–Co/SiC composite coatings. *Surf. Coat. Technol.* **2012**, *206*, 4964–4975, doi:10.1016/j.surfcoat.2012.05.122.

65. Góral, A.; Nowak, M.; Berent, K.; Kania, B. Influence of current density on microstructure and properties of electrodeposited nickel-alumina composite coatings. *J. Alloys Compd.* **2014**, *615*, S406-S410, doi:10.1016/j.jallcom.2014.01.025.
66. Shawki, S.; Abdel Hamid, Z. Deposition of high wear resistance of Ni-composite coatings. *Anti-Corrosion Method & Mater.* **1997**, *44*, 178–185, doi:10.1108/00035599710167142.
67. Gyftou, P.; Pavlatou, E.A.; Spyrellis, N. Effect of pulse electrodeposition parameters on the properties of Ni/nano-SiC composites. *Appl. Surf. Sci.* **2008**, *254*, 5910–5916, doi:10.1016/j.apsusc.2008.03.151.
68. Gyftou, P.; Stroumbouli, M.; Pavlatou, E.A.; Spyrellis, N. Electrodeposition of Ni/SiC Composites by Pulse Electrolysis. *Trans. IMF* **2002**, *80*, 88–91, doi:10.1080/00202967.2002.11871440.
69. Pavlatou, E.A.; Stroumbouli, M.; Gyftou, P.; Spyrellis, N. Hardening effect induced by incorporation of SiC particles in nickel electrodeposits. *J. Appl. Electrochem.* **2006**, *36*, 385–394, doi:10.1007/s10800-005-9082-y.
70. Kollia, C.; Loizos, Z.; Spyrellis, N. Influence of pulse reversed current technique on the crystalline orientation and surface morphology of nickel electrodeposits. *Surf. Coat. Technol.* **1991**, *45*, 155–160, doi:10.1016/0257-8972(91)90218-L.
71. Gül, H.; Uysal, M.; Akbulut, H.; Alp, A. Effect of PC electrodeposition on the structure and tribological behavior of Ni–Al₂O₃ nanocomposite coatings. *Surf. Coat. Technol.* **2014**, *258*, 1202–1211, doi:10.1016/j.surfcoat.2014.07.002.
72. Lajevardi, S.A.; Shahrabi, T. Effects of pulse electrodeposition parameters on the properties of Ni–TiO₂ nanocomposite coatings. *Appl. Surf. Sci.* **2010**, *256*, 6775–6781, doi:10.1016/j.apsusc.2010.04.088.
73. Podlaha, E.J. Pulse-Reverse Plating of Nanocomposite Thin Films. *J. Electrochem. Soc.* **1997**, *144*, L200, doi:10.1149/1.1837799.
74. Xiong-Skiba, P.; Engelhaupt, D.; Hulguin, R.; Ramsey, B. Effect of Pulse Plating Parameters on the Composition of Alumina/Nickel Composite. *J. Electrochem. Soc.* **2005**, *152*, C571, doi:10.1149/1.1948947.
75. Guglielmi, N. Kinetics of the Deposition of Inert Particles from Electrolytic Baths. *J. Electrochem. Soc.* **1972**, *119*, 1009–1012, doi:10.1149/1.2404383.

76. Celis, J.P.; Roos, J.R.; Buelens, C. A Mathematical Model for the Electrolytic Codeposition of Particles with a Metallic Matrix. *J. Electrochem. Soc.* **1987**, *134*, 1402–1408, doi:10.1149/1.2100680.
77. Fransaer, J.; Celis, J.P.; Roos, J.R. Analysis of the Electrolytic Codeposition of Non-Brownian Particles with Metals. *J. Electrochem. Soc.* **1992**, *139*, 413–425, doi:10.1149/1.2069233.
78. Hwang, B.J. Mechanism of Codeposition of Silicon Carbide with Electrolytic Cobalt. *J. Electrochem. Soc.* **1993**, *140*, 979, doi:10.1149/1.2056239.
79. Vereecken, P.M.; Shao, I.; Searson, P.C. Particle Codeposition in Nanocomposite Films. *J. Electrochem. Soc.* **2000**, *147*, 2572, doi:10.1149/1.1393570.
80. Berçot, P.; Peña-Muñoz, E.; Pagetti, J. Electrolytic composite Ni–PTFE coatings: An adaptation of Guglielmi's model for the phenomena of incorporation. *Surf. Coat. Technol.* **2002**, *157*, 282–289, doi:10.1016/S0257-8972(02)00180-9.
81. Nowak, P.; Socha, R.P.; Kaisheva, M.; Fransaer, J.; Celis, J.-P.; Stoinov, Z. Electrochemical investigation of the codeposition of SiC and SiO₂ particles with nickel. *J. Appl. Electrochem.* **2000**, *30*, 429–437, doi:10.1023/A:1003979117146.
82. Wang, S.-C.; Wei, W.-C.J. Electrokinetic properties of nanosized SiC particles in highly concentrated electrolyte solutions. *J. Am. Ceram. Soc.* **2001**, *84*, 1411–1414, doi:10.1111/j.1151-2916.2001.tb00852.x.
83. Bund, A.; Thiemig, D. Influence of bath composition and pH on the electrocodeposition of alumina nanoparticles and nickel. *Surf. Coat. Technol.* **2007**, *201*, 7092–7099, doi:10.1016/j.surfcoat.2007.01.010.
84. Man, J.; Zhang, S.; Li, J.; Zhao, B.; Chen, Y. Effects of electrolyte pH on morphologies and mechanical properties of α -Al₂O₃/Ni composite coatings and role of zeta potentials in co-deposition process. *Surf. Coat. Technol.* **2014**, *249*, 118–124, doi:10.1016/j.surfcoat.2014.03.054.
85. Chen, L.; Wang, L.; Zeng, Z.; Zhang, J. Effect of surfactant on the electrodeposition and wear resistance of Ni–Al₂O₃ composite coatings. *Mater. Sci. Eng. A* **2006**, *434*, 319–325, doi:10.1016/j.msea.2006.06.098.
86. Borkar, T.; Harimkar, S.P. Effect of electrodeposition conditions and reinforcement content on microstructure and tribological

- properties of nickel composite coatings. *Surf. Coat. Technol.* **2011**, *205*, 4124–4134, doi:10.1016/j.surfcoat.2011.02.057.
87. Sheu, H.-H.; Huang, P.-C.; Tsai, L.-C.; Hou, K.-H. Effects of plating parameters on the Ni–P–Al₂O₃ composite coatings prepared by pulse and direct current plating. *Surf. Coat. Technol.* **2013**, *235*, 529–535, doi:10.1016/j.surfcoat.2013.08.020.
 88. Hou, K.-H.; Hwu, W.-H.; Ke, S.-T.; Ger, M.-D. Ni–P–SiC composite produced by pulse and direct current plating. *Mater. Chem. Phys.* **2006**, *100*, 54–59, doi:10.1016/j.matchemphys.2005.12.016.
 89. Aroyo, M.; Tzonev, N. Pulse periodic reverse plating: New possibilities for electrodeposition of metal coatings with improved properties: Part 1. *Plat. Surf. Finish.* **2002**, *89*, 48–53.
 90. Lampke, T.; Wielage, B.; Dietrich, D.; Leopold, A. Details of crystalline growth in co-deposited electroplated nickel films with hard (nano)particles. *Appl. Surf. Sci.* **2006**, *253*, 2399–2408, doi:10.1016/j.apsusc.2006.04.060.
 91. Góral, A. Nanoscale structural defects in electrodeposited Ni/Al₂O₃ composite coatings. *Surf. Coat. Technol.* **2017**, *319*, 23–32, doi:10.1016/j.surfcoat.2017.03.061.
 92. Benea, L.; Danaila, E.; Celis, J.-P. Influence of electro-co-deposition parameters on nano-TiO₂ inclusion into nickel matrix and properties characterization of nanocomposite coatings obtained. *Mater. Sci. Eng. A* **2014**, *610*, 106–115, doi:10.1016/j.msea.2014.05.028.
 93. Gül, H.; Kılıç, F.; Aslan, S.; Alp, A.; Akbulut, H. Characteristics of electro-co-deposited Ni–Al₂O₃ nano-particle reinforced metal matrix composite (MMC) coatings. *Wear* **2009**, *267*, 976–990, doi:10.1016/j.wear.2008.12.022.
 94. Huang, Y.S.; Zeng, X.T.; Annergren, I.; Liu, F.M. Development of electroless NiP–PTFE–SiC composite coating. *Surf. Coat. Technol.* **2003**, *167*, 207–211, doi:10.1016/S0257-8972(02)00899-X.
 95. Tang, A.; Wang, M.; Huang, W.; Wang, X. Composition design of Ni–nano-Al₂O₃–PTFE coatings and their tribological characteristics. *Surf. Coat. Technol.* **2015**, *282*, 121–128, doi:10.1016/j.surfcoat.2015.10.034.
 96. Zhou, J.; Zhao, G.; Li, J.; Chen, J.; Zhang, S.; Wang, J.; Walsh, F.C.; Wang, S.; Xue, Y. Electroplating of non-fluorinated superhydrophobic Ni/WC/WS₂ composite coatings with high

- abrasive resistance. *Appl. Surf. Sci.* **2019**, *487*, 1329–1340, doi:10.1016/j.apsusc.2019.05.244.
97. Williamson, K.; Bow, A. *Research methods for students, academics and professionals: Information management and systems*, Second edition; Centre for Information Studies: Wagga Wagga, New South Wales, 2002, ISBN 178063420X.
 98. Schwartz, A.J.; Kumar, M.; Adams, B.L.; Field, D.P. *Electron Backscatter Diffraction in Materials Science*; Springer US: Boston, MA, 2009, ISBN 978-0-387-88135-5.
 99. Oliver, W.C.; Pharr, G.M. An improved technique for determining hardness and elastic modulus using load and displacement sensing indentation experiments. *J. Mater. Res.* **1992**, *7*, 1564–1583, doi:10.1557/JMR.1992.1564.
 100. Magnani, G.; Galvagno, S.; Sico, G.; Portofino, S.; Freda, C.; Burresi, E. Sintering and mechanical properties of β -SiC powder obtained from waste tires. *Journal of Advanced Ceramics* **2016**, *5*, 40–46, doi:10.1007/s40145-015-0170-0.
 101. Li, Y.; Yu, C.; Gan, Y.; Jiang, P.; Yu, J.; Ou, Y.; Zou, D.-F.; Huang, C.; Wang, J.; Jia, T.; et al. Mapping the elastic properties of two-dimensional MoS₂ via bimodal atomic force microscopy and finite element simulation. *npj Computational Materials* **2018**, *4*, 49, doi:10.1038/s41524-018-0105-8.
 102. Ebrahimi, F.; Bourne, G.; Kelly, M.; Matthews, T. Mechanical properties of nanocrystalline nickel produced by electrodeposition. *Nanostruct. Mater.* **1999**, *11*, 343–350, doi:10.1016/S0965-9773(99)00050-1.
 103. Merita, F.; Umemoto, D.; Yuasa, M.; Miyamoto, H.; Goto, T. Electrodeposition of nanocrystalline nickel embedded with inert nanoparticles formed via inverse hydrolysis. *Appl. Surf. Sci.* **2018**, *458*, 612–618, doi:10.1016/j.apsusc.2018.07.123.
 104. Hou, F.; Wang, W.; Guo, H. Effect of the dispersibility of ZrO₂ nanoparticles in Ni–ZrO₂ electroplated nanocomposite coatings on the mechanical properties of nanocomposite coatings. *Appl. Surf. Sci.* **2006**, *252*, 3812–3817, doi:10.1016/j.apsusc.2005.05.076.
 105. Zhou, W.; Ren, X.; Yang, Y.; Tong, Z.; Chen, L. Dislocation behavior in nickel and iron during laser shock-induced plastic deformation. *Int J Adv Manuf Technol* **2020**, *108*, 1073–1083, doi:10.1007/s00170-019-04822-8.

106. Walker, C.T.; Walker, R. New Explanation for the Hardening Effect of Ultrasound on Electro-deposits. *Nat. Phys. Sci.* **1973**, *244*, 141–142, doi:10.1038/physci244141a0.
107. Galvan, D.; Pei, Y.T.; Hosson, J. de. Influence of deposition parameters on the structure and mechanical properties of nanocomposite coatings. *Surf. Coat. Technol.* **2006**, *201*, 590–598, doi:10.1016/j.surfcoat.2005.12.007.
108. Farrokhzad, M.A.; Khan, T.I. A study on hardness of nickel-based cermet coatings composed of α -Al₂O₃ and TiO₂ nanoparticles. *Advanced Composite Materials* **2015**, *24*, 141–159, doi:10.1080/09243046.2014.882537.
109. Kobayashi, H.; Imamura, K.; Kim, W.-B.; Im, S.-S.; Asuha. Nitric acid oxidation of Si (NAOS) method for low temperature fabrication of SiO₂/Si and SiO₂/SiC structures. *Appl. Surf. Sci.* **2010**, *256*, 5744–5756, doi:10.1016/j.apsusc.2010.03.092.
110. Kenjiro, M.; Takahisa, U.; Tetsuya, H.; Kunio, E. Effects of surfactants and surface treatment on aqueous dispersion of silicon carbide. *Bull. Chem. Soc. Jpn.* **1987**, *60*, 89–94, doi:10.1246/bcsj.60.89.
111. Li, G.; Du Zhang; Qiao, Q.; Yu, Y.; Peterson, D.; Zafar, A.; Kumar, R.; Curtarolo, S.; Hunte, F.; Shannon, S.; et al. All The Catalytic Active Sites of MoS₂ for Hydrogen Evolution. *J. Am. Chem. Soc.* **2016**, *138*, 16632–16638, doi:10.1021/jacs.6b05940.
112. Chang, Y.-C.; Chang, Y.-Y.; Lin, C.-I. Process aspects of the electrolytic codeposition of molybdenum disulfide with nickel. *Electrochim. Acta* **1998**, *43*, 315–324, doi:10.1016/S0013-4686(97)00072-8.
113. Gül, H.; Kılıç, F.; Uysal, M.; Aslan, S.; Alp, A.; Akbulut, H. Effect of particle concentration on the structure and tribological properties of submicron particle SiC reinforced Ni metal matrix composite (MMC) coatings produced by electrodeposition. *Appl. Surf. Sci.* **2012**, *258*, 4260–4267, doi:10.1016/j.apsusc.2011.12.069.
114. Alizadeh, M.; Mirak, M.; Salahinejad, E.; Ghaffari, M.; Amini, R.; Roosta, A. Structural characterization of electro-codeposited Ni–Al₂O₃–SiC nanocomposite coatings. *J. Alloys Compd.* **2014**, *611*, 161–166, doi:10.1016/j.jallcom.2014.04.181.
115. Hou, K.; Ger, M.; Wang, L.; Ke, S. The wear behaviour of electro-codeposited Ni–SiC composites. *Wear* **2002**, *253*, 994–1003, doi:10.1016/S0043-1648(02)00222-3.

116. Tudela, I.; Zhang, Y.; Pal, M.; Kerr, I.; Cobley, A.J. Ultrasound-assisted electrodeposition of thin nickel-based composite coatings with lubricant particles. *Surf. Coat. Technol.* **2015**, *276*, 89–105, doi:10.1016/j.surfcoat.2015.06.030.
117. Cardinal, M.F.; Castro, P.A.; Baxi, J.; Liang, H.; Williams, F.J. Characterization and frictional behavior of nanostructured Ni–W–MoS₂ composite coatings. *Surf. Coat. Technol.* **2009**, *204*, 85–90, doi:10.1016/j.surfcoat.2009.06.037.
118. Huang, Z.; Xiong, D. MoS₂ coated with Al₂O₃ for Ni–MoS₂/Al₂O₃ composite coatings by pulse electrodeposition. *Surf. Coat. Technol.* **2008**, *202*, 3208–3214, doi:10.1016/j.surfcoat.2007.11.033.
119. Zhou, N.; Wang, S.; Walsh, F.C. Effective particle dispersion via high-shear mixing of the electrolyte for electroplating a nickel-molybdenum disulphide composite. *Electrochim. Acta* **2018**, *283*, 568–577, doi:10.1016/j.electacta.2018.06.187.
120. Jiang, W.; Shen, L.; Wang, Z.; Wang, K.; Xu, M.; Tian, Z. Wear resistance of a Ni-PTFE composite coating strengthened with nano-SiC particles. *Mater. Res. Express* **2019**, *6*, 96443, doi:10.1088/2053-1591/ab320b.
121. Alimadadi, H.; Fanta, A.B.; Somers, M.A.; Pantleon, K. Crystallographic orientations and twinning of electrodeposited nickel—a study with complementary characterization methods. *Surf. Coat. Technol.* **2016**, *254*, 207–216, doi:10.1016/j.surfcoat.2014.06.013.
122. Godon, A.; Creus, J.; Feaugas, X.; Conforto, E.; Pichon, L.; Armand, C.; Savall, C. Characterization of electrodeposited nickel coatings from sulphamate electrolyte without additive. *Mater. Charact.* **2011**, *62*, 164–173, doi:10.1016/j.matchar.2010.11.011.
123. He, Y.; Sun, W.T.; Wang, S.C.; Reed, P.; Walsh, F.C. An electrodeposited Ni-P-WS₂ coating with combined super-hydrophobicity and self-lubricating properties. *Electrochim. Acta* **2017**, *245*, 872–882, doi:10.1016/j.electacta.2017.05.166.
124. Shourije, S.M.J.S.; Bahrololoom, M.E. Effect of current density, MoS₂ content and bath agitation on tribological properties of electrodeposited nanostructured Ni–MoS₂ composite coatings. *Tribol.-Mater. Surf. Interfaces* **2019**, *13*, 76–87, doi:10.1080/17515831.2019.1589160.

125. Armstrong, R.W. 60 Years of Hall-Petch: Past to Present Nano-Scale Connections. *Mater. Trans.* **2014**, *55*, 2–12, doi:10.2320/matertrans.MA201302.
126. Cordero, Z.C.; Knight, B.E.; Schuh, C.A. Six decades of the Hall–Petch effect – a survey of grain-size strengthening studies on pure metals. *Int. Mater. Rev.* **2016**, *61*, 495–512, doi:10.1080/09506608.2016.1191808.
127. Godon, A.; Creus, J.; Cohendoz, S.; Conforto, E.; Feaugas, X.; Girault, P.; Savall, C. Effects of grain orientation on the Hall–Petch relationship in electrodeposited nickel with nanocrystalline grains. *Scripta Mater.* **2010**, *62*, 403–406, doi:10.1016/j.scriptamat.2009.11.038.
128. Miguel, F.L.; Müller, R.; Mathur, S.; Mücklich, F. Microstructure and mechanical properties of electrodeposited Ni and Ni–matrix–nanocomposite thin films. *Mater. Sci. Eng. A* **2015**, *646*, 254–262, doi:10.1016/j.msea.2015.08.069.
129. Shakibi Nia, N.; Savall, C.; Creus, J.; Bourgon, J.; Girault, P.; Metsue, A.; Cohendoz, S.; Feaugas, X. On the implication of solute contents and grain boundaries on the Hall-Petch relationship of nanocrystalline Ni-W alloys. *Mater. Sci. Eng. A* **2016**, *678*, 204–214, doi:10.1016/j.msea.2016.09.097.
130. Knapp, J.A.; Follstaedt, D.M. Hall–Petch relationship in pulsed-laser deposited nickel films. *J. Mater. Res.* **2004**, *19*, 218–227, doi:10.1557/jmr.2004.19.1.218.
131. Hutchings, I.; Shipway, P. *Tribology: friction and wear of engineering materials*, 2 Edition; Elsevier / Butterworth-Heinemann: Amsterdam, 2017, ISBN 9780081009512.
132. Holmberg, K.; Ronkainen, H.; Laukkanen, A.; Wallin, K. Friction and wear of coated surfaces — scales, modelling and simulation of tribomechanisms. *Surf. Coat. Technol.* **2007**, *202*, 1034–1049, doi:10.1016/j.surfcoat.2007.07.105.
133. Gyftou, P.; Stroumbouli, M.; Pavlatou, E.A.; Asimidis, P.; Spyrellis, N. Tribological study of Ni matrix composite coatings containing nano and micro SiC particles. *Electrochim. Acta* **2005**, *50*, 4544–4550, doi:10.1016/j.electacta.2004.10.090.
134. Lanzutti, A.; Lekka, M.; Leitenburg, C. de; Fedrizzi, L. Effect of pulse current on wear behavior of Ni matrix micro-and nano-SiC composite coatings at room and elevated temperature. *Tribol. Int.* **2019**, *132*, 50–61, doi:10.1016/j.triboint.2018.12.011.

135. Gyawali, G.; Joshi, B.; Tripathi, K.; Lee, S.W. Effect of Ultrasonic Nanocrystal Surface Modification on Properties of Electrodeposited Ni and Ni-SiC Composite Coatings. *J. Mater. Eng. Perform.* **2017**, *26*, 4462–4469, doi:10.1007/s11665-017-2891-4.
136. Zhou, Y.; Zhang, H.; Qian, B. Friction and wear properties of the co-deposited Ni–SiC nanocomposite coating. *Appl. Surf. Sci.* **2007**, *253*, 8335–8339, doi:10.1016/j.apsusc.2007.04.047.
137. Benea, L.; Bonora, P.L.; Borello, A.; Martelli, S. Wear corrosion properties of nano-structured SiC–nickel composite coatings obtained by electroplating. *Wear* **2002**, *249*, 995–1003, doi:10.1016/S0043-1648(01)00844-4.
138. Donnet, C.; Erdemir, A. Historical developments and new trends in tribological and solid lubricant coatings. *Surf. Coat. Technol.* **2004**, *180-181*, 76–84, doi:10.1016/j.surfcoat.2003.10.022.
139. Mahidashti, Z.; Aliofkhazraei, M.; Lotfi, N. Review of Nickel-Based Electrodeposited Tribo-Coatings. *Trans. Indian Inst. Met.* **2017**, *258*, 6550, doi:10.1007/s12666-017-1175-x.
140. Berman, A.D.; Ducker, W.A.; Israelachvili, J.N. Experimental and Theoretical Investigations of Stick-Slip Friction Mechanisms. In *Physics of Sliding Friction*; Persson, B.N.J., Tosatti, E., Eds.; Springer Netherlands: Dordrecht, 1996; pp 51–67, ISBN 978-90-481-4674-1.
141. Leyland, A.; Matthews, A. On the significance of the H/E ratio in wear control: a nanocomposite coating approach to optimised tribological behaviour. *Wear* **2000**, *246*, 1–11, doi:10.1016/S0043-1648(00)00488-9.
142. Góral, A.; Lityńska-Dobrzyńska, L.; Kot, M. Effect of Surface Roughness and Structure Features on Tribological Properties of Electrodeposited Nanocrystalline Ni and Ni/Al₂O₃ Coatings. *J. Mater. Eng. Perform.* **2017**, *26*, 2118–2128, doi:10.1007/s11665-017-2662-2.

APPENDED PAPERS

- Supplement I** S. Pinate, A. Ispas, P. Leisner, C. Zanella
Electrocodeposition of Ni composites and surface treatment of SiC nano-particles
Surface and Coatings Technology, 2021. Vol. 406, pp. 12663. (Open access)
DOI: 10.1016/j.surfcoat.2020.126663
- Supplement II** S. Pinate, P. Leisner, C. Zanella
Electrocodeposition of nano-SiC particles by pulse-reverse under an adapted waveform
Journal of The Electrochemical Society, 2019. Vol. 166, pp. D804-D809.
DOI: 10.1149/2.0441915jes
- Supplement III** S. Pinate, N. Nefzi, C. Zanella
Role of anodic time in pulse-reverse electrocodeposition of nano-SiC particles
Manuscript submitted for journal publication
- Supplement IV** S. Pinate, F. Eriksson, P. Leisner, C. Zanella
Effects of particles codeposition and ultrasound agitation on the electrocrystallization of metal matrix composites
Manuscript submitted for journal publication
- Supplement V** S. Pinate, C. Zanella
Wear behaviour of Ni-based composite coatings with dual nano-SiC:Graphite powder mix
Coatings, 2020. Vol. 10, pp. 1060.
DOI: 10.3390/coatings10111060
(Open access)

- Supplement VI** S. Pinate, P. Leisner, C. Zanella
Wear resistance and self-lubrication of electrodeposited Ni-SiC:MoS₂ dual composite coatings
Manuscript for submitted journal publication
- Supplement VII** S. Pinate, E. Ghassemali, C. Zanella
Strengthening mechanisms by particles codeposition and wear behaviour of electroplated Ni-SiC coatings
Manuscript for journal publication

School of Engineering Dissertation Series

1. Olofsson, Jakob. (2012). Microstructure-based Mechanical Behaviour in Structural Analyses of Cast Components. Licentiate Thesis.
School of Engineering Dissertation Series No 1. ISBN 978-91-87289-01-9
2. Bäckstrand, Jenny. (2012). A Method for Customer-driven Purchasing Aligning Supplier interaction and Customer-driven manufacturing. Doctoral Thesis.
School of Engineering Dissertation Series No 2. ISBN 978-91-87289-02-6
3. Olofsson, Jakob. (2014). Simulation of Microstructure-based Mechanical Behaviour of Cast Components. Doctoral Thesis.
School of Engineering Dissertation Series No 3. ISBN 978-91-87289-04-0
4. Fourlakidis, Vasilios. (2014). Dendritic Morphology and Ultimate Tensile Strength in Lamellar Graphite Iron. Licentiate Thesis.
School of Engineering Dissertation Series No 4. ISBN 978-91-87289-05-7
5. Ghasemi, Rohollah. (2015). Tribological and Mechanical Behaviour of Lamellar and Compacted Graphite Irons in Engine Applications. Licentiate Thesis.
School of Engineering Dissertation Series No 5. ISBN 978-91-87289-06-4
6. Payandeh, Mostafa. (2015). Rheocasting of Aluminium Alloys: Slurry Formation, Microstructure, and Properties. Licentiate Thesis.
School of Engineering Dissertation Series No 6. ISBN 978-91-87289-07-1
7. Zamani, Mohammadreza. (2015). Al-Si Cast Alloys – Microstructure and mechanical properties at ambient and elevated temperature. Licentiate Thesis.
School of Engineering Dissertation Series No 7. ISBN 978-91-87289-08-8
8. Bjurenstedt, Anton. (2015). Imperfections in Recycled Aluminium-Silicon Cast Alloys. Licentiate Thesis.
School of Engineering Dissertation Series No 8. ISBN 978-91-87289-09-5
9. Kasvayee, Keivan Amiri. (2015). Microstructure and deformation behaviour of ductile iron under tensile loading. Licentiate Thesis.
School of Engineering Dissertation Series No 9. ISBN 978-91-87289-10-1
10. Dini, Hoda. (2015). As-cast AZ91D magnesium alloy properties. Effect of microstructure and temperature. Licentiate Thesis.
School of Engineering Dissertation Series No 10. ISBN 978-91-87289-11-8
11. Poorkiany, Morteza (2015). Support Maintenance of Design Automation Systems – A framework to Capture, Structure and Access Design Rationale. Licentiate Thesis.
School of Engineering Dissertation Series No 11. ISBN 978-91-87289-12-5

12. Cenanovic, Mirza (2015). Finite element methods on surfaces. Licentiate Thesis.
School of Engineering Dissertation Series No 12. ISBN 978-91-87289-13-2
13. Amouzgar, Kaveh (2015). Metamodel based multi-objective optimization.
Licentiate Thesis.
School of Engineering Dissertation Series No 13. ISBN 978-91-87289-14-9
14. Wlazlak, Paraskeva (2016). Integration in global development projects: a study of new product development and production relocation projects. Licentiate Thesis.
School of Engineering Dissertation Series No 14. ISBN 978-91-87289-15-6
15. Payandeh, Mostafa (2016). Rheocasting of Aluminium Alloys: Process and Components Characteristics. Doctoral Thesis.
School of Engineering Dissertation Series No 15. ISBN 978-91-87289-16-3
16. Alayón, Claudia (2016). Exploring Sustainable Manufacturing Principles and Practices. Licentiate Thesis.
School of Engineering Dissertation Series No 16. ISBN 978-91-87289-17-0
17. Ghasemi, Rohollah (2016). Influence of Microstructure on Mechanical and Tribological Properties of Lamellar and Compacted Irons in Engine Applications. Doctoral Thesis.
School of Engineering Dissertation Series No 17. ISBN 978-91-87289-18-7
18. Tiedemann, Fredrik (2017). Strategic Lead-Times and their Implications on Financial Performance. Licentiate Thesis.
School of Engineering Dissertation Series No 18. ISBN 978-91-87289-19-4
19. Zhu, Baiwei (2017). On the Influence of Si on Anodising and Mechanical Properties of Cast Aluminium Alloys. Licentiate Thesis.
School of Engineering Dissertation Series No 19. ISBN 978-91-87289-20-0
20. André, Samuel (2017). Supporting the Utilization of a Platform Approach in the Engineer-to-Order Supplier Industry. Licentiate Thesis.
School of Engineering Dissertation Series No 20. ISBN 978-91-87289-21-7
21. Zamani, Mohammadreza (2017). Al-Si Cast Alloys – Microstructure and Mechanical Properties at Ambient and Elevated Temperatures. Doctoral Thesis.
School of Engineering Dissertation Series No 21. ISBN 978-91-87289-22-4
22. Cenanovic, Mirza (2017). Finite element methods for surface problems. Doctoral Thesis.
School of Engineering Dissertations Series No. 22. ISBN 978-91-87289-23-1
23. Hernando, Juan Carlos (2017). Morphological Characterization of Primary Austenite in Cast Iron. Licentiate Thesis.
School of Engineering Dissertation Series No. 23. ISBN 978-91-87289-24-8

24. Domeij, Björn (2017). On the Solidification of Compacted and Spheroidal Graphite Iron. Licentiate Thesis.
School of Engineering Dissertation Series No. 24. ISBN 978-91-87289-25-5
25. Salim, Roaa (2017). Exploring aspects of automation decisions – A study in the Swedish wood products industry. Licentiate Thesis.
School of Engineering Dissertation Series No. 25. ISBN 978-91-87289-26-2
26. de Goey, Heleen (2017). Exploring design-driven innovation: A study on value creation by SMEs in the Swedish wood products industry. Licentiate Thesis.
School of Engineering Dissertation Series No. 26. ISBN 978-91-87289-27-9
27. Kasvayee, Keivan Amiri (2017). On deformation behavior and cracking of ductile iron; effect of microstructure. Doctoral Thesis.
School of Engineering Dissertation Series No. 27. ISBN 978-91-87289-28-6
28. Bjurenstedt, Anton (2017). On the influence of imperfections on microstructure and properties of recycled Al-Si casting alloys. Doctoral Thesis.
School of Engineering Dissertation Series No. 28. ISBN 978-91-87289-29-3
29. Siafakas, Dimitrios (2017). The influence of deoxidation practice on the as-cast grain size of austenitic manganese steels. Licentiate Thesis.
School of Engineering Dissertation Series No. 29. ISBN 978-91-87289-30-9
30. Dini, Hoda (2017). As-Cast AZ91D Magnesium Alloy Properties – Effect of Microstructure and Temperature. Doctoral Thesis.
School of Engineering Dissertation Series No. 30. ISBN 978-91-87289-31-6
31. Poorkiany, Morteza (2017). Design Rationale Management as Part of Engineering Design and Design Automation. Doctoral Thesis.
School of Engineering Dissertation Series No. 31. ISBN 978-91-87289-32-3
32. Hellström, Kristina (2017). Density variations during solidification of lamellar graphite iron. Licentiate Thesis.
School of Engineering Dissertation Series No. 32. ISBN 978-91-87289-33-0
33. Riestra, Martin (2017). High Performing Cast Aluminium Silicon Alloys. Licentiate Thesis.
School of Engineering Dissertation Series No. 33. ISBN 978-91-87289-34-7
34. Sansone, Cinzia (2018). Critical operations capabilities in a high cost environment. Licentiate Thesis.
School of Engineering Dissertation Series No. 34. ISBN 978-91-87289-35-4
35. Popovic, Djordje (2018). Off-site manufacturing systems development in timber house building. Towards mass customization-oriented manufacturing. Licentiate Thesis.
School of Engineering Dissertation Series No. 35. ISBN 978-91-87289-36-1

36. Santos, Jorge (2018). Al-7Si-Mg Semi-Solid Castings – Microstructure and Mechanical Properties. Licentiate Thesis.
School of Engineering Dissertation Series No. 36. ISBN 978-91-87289-37-8
37. Heikkinen, Tim (2018). Multidisciplinary Design Automation: Working with Product Model Extensions. Licentiate Thesis.
School of Engineering Dissertation Series No 37. ISBN 978-91-87289-38-5
38. Fournalakidis, Vasilios (2019). Dendritic Morphology and Ultimate Tensile Strength of Pearlitic Lamellar Graphite Iron. Doctoral Thesis.
School of Engineering. Dissertation Series No 38. ISBN 978-91-87289-40-8
39. Pinate, Santiago (2019). Study of Particle-Current-Electrocrystallization Interactions in Electroplating of Ni/SiC Coatings. Licentiate Thesis.
School of Engineering. Dissertation Series No 39. ISBN 978-91-87289-41-5
40. Hernando Sanz, Juan Carlos (2019). The Role of Primary Austenite Morphology in Cast Iron. Doctoral Thesis.
School of Engineering. Dissertation Series No 40. ISBN 978-91-87289-42-2
41. Zhu, Baiwei (2019). Casting and Anodising of Al Alloys - Alloy Design, Manufacturing Process and Material Properties. Doctoral Thesis.
School of Engineering. Dissertation Series No 41. ISBN 978-91-87289-43-9
42. Hedvall, Lisa (2019). Reducing and Absorbing Variations in a Manufacturing Context. Licentiate Thesis.
School of Engineering. Dissertation Series No. 42. ISBN 978-91-87289-45-3
43. Siafakas, Dimitrios (2019). On Particles and Slags in Steel Casting. Doctoral Thesis.
School of Engineering. Dissertation Series No. 43. ISBN 978-91-87289-46-0
44. Samvin, David (2019). Finite Element Methods for Interface Problems. Licentiate Thesis.
School of Engineering. Dissertation Series No. 44. ISBN 978-91-87289-47-7
45. Jansson Johan (2019). Process-Induced Local Material Variations in Finite Element Simulations of Cast and Fibre Reinforced Injection Moulded Components. Licentiate Thesis.
School of Engineering. Dissertation Series No. 45. ISBN 978-91-87289-48-4
46. Domeij, Björn (2019). Compacted Graphite Iron: On Solidification Phenomena Related to Shrinkage Defects. Doctoral Thesis.
School of Engineering. Dissertation Series No. 46. ISBN 978-91-87289-49-1
47. Wlazlak, Paraskeva (2019). Management of the Industrialisation Process in Distributed Geographical and Organisational Context. Doctoral Thesis.
School of Engineering. Dissertation Series No. 47. ISBN 978-91-87289-50-7

48. André, Samuel (2019). The Design Platform Approach – Enabling Platform-Based Development in the Engineer-to-Order Industry. Doctoral Thesis. School of Engineering. Dissertation Series No. 48. ISBN 978-91-87289-51-4
49. Kallin, Sara (2019). Deformation of human soft tissues – Experimental and numerical aspects. Licentiate Thesis. School of Engineering. Dissertation Series No. 49. ISBN 978-91-87289-52-1
50. Käkelä, Nikolas (2019). Customization-based interaction in ETO. Licentiate Thesis. School of Engineering. Dissertation Series No. 50. ISBN 978-91-87289-53-8
51. Sollander, Kristina (2020). Organisational Ambidexterity in Practice: A Study of Managerial Work in Manufacturing SMEs. Licentiate Thesis. School of Engineering. Dissertation Series No. 51. ISBN 978-91-87289-54-5
52. Vestin, Alexander (2020). Smart Manufacturing for the Wooden Single-Family House Industry. Licentiate Thesis. School of Engineering. Dissertation Series No. 52. ISBN 978-91-87289-55-2
53. Thajudeen, Shammath (2020). Supporting the Design Phase of Industrialised House Building Using a Product Platform Approach - A Case Study of a Timber-based Post and Beam Building System. Licentiate Thesis. School of Engineering. Dissertation Series No. 53. ISBN 978-91-87289-56-9
54. Sequeira, Movin Frank (2020). Developing Decision-Support Tools for Evaluation of Manufacturing Reshoring Decisions. Licentiate Thesis. School of Engineering. Dissertation Series No. 54. ISBN 978-91-87289-57-6
55. Popovic, Djordje (2020). The Development and Use of Product Platforms in Single-Family Industrialized House Building. Doctoral Thesis. School of Engineering. Dissertation Series No. 55. ISBN 978-91-87289-58-3
56. Tiedemann, Fredrik (2020). Strategies for Demand-Driven Supply Chains – A Decoupling Thinking Perspective. Doctoral Thesis. School of Engineering. Dissertation Series No. 56. ISBN 978-91-87289-59-0
57. Santos, Jorge (2020). Semi-Solid Al-7Si-Mg Castings – Microstructure and Mechanical Properties. Doctoral Thesis. School of Engineering. Dissertation Series No. 57. ISBN 978-91-87289-61-3
58. Ekström, Thomas (2020). Segmentation and Differentiation in Defence Supply Chain Design – A Dynamic Purchasing Portfolio Model for Defence Procurement. Doctoral Thesis. School of Engineering. Dissertation Series No. 58. ISBN 978-91-87289-62-0.
59. Sainis, Salil (2021). The Influence of Al Alloy Microstructure on Conversion Coating Formation. Licentiate Thesis. School of Engineering. Dissertation Series No. 59. ISBN 978-91-87289-63-7.

60. Heikkinen, Tim (2021). Extended Product Models Supporting Multidisciplinary Design Automation. Doctoral Thesis. School of Engineering. Dissertation Series No. 60. ISBN 978-91-87289-64-4

61. Salim, Roaa (2021). Exploring the Content and Process of Automation Decisions in Manufacturing System Development Projects – A Study in the Swedish Wood Products Industry. Doctoral Thesis. School of Engineering. Dissertation Series No. 61. ISBN 978-91-87289-65-1

62. Bogdanoff, Toni (2021). The Influence of Microstructure on the Crack Initiation and Propagation in Al-Si Casting Alloys. Licentiate Thesis. School of Engineering. Dissertation Series No. 62. ISBN 978-91-87289-66-8

63. Piñate, Santiago (2021). Control of Particles Codeposition and Strengthening Mechanisms in Nickel Based Nanocomposite Coatings. Doctoral Thesis. School of Engineering. Dissertation Series No. 63. ISBN 978-91-87289-67-5

Control of Particles Codeposition and Strengthening Mechanisms in Nickel Based Nanocomposite Coatings

Surface durability is a key factor in the service life of components. Depending on the aggressiveness of the environment, surface deterioration by wear or corrosion leads to failure of the bulk material and eventually to the loss of functionality of the component. Therefore, designing surfaces to withstand service requirements is a critical aspect of product realisation.

Electroplating is an attractive technique to mass-produce affordable protective coatings due to its low cost, easy maintenance, and adjustable production times. Producing nanocomposite coatings by electroplating has received significant attention for decades due to their potential to provide excellent surface protection. Nanocomposites provide the possibility of combining different materials to achieve multifunctionality and, due to the nanometer size of the reinforcer phase, promote additional strengthening effects in the matrix not present in microcomposites. However, the industrial applicability remains limited due to the lack of control in their production process.

The present work focuses on the relationship between the input parameters and codeposition of nanoparticles, identifying critical factors and providing methods to control the process. A surface treatment for the reinforcing powder was developed to minimise the differences between the particles surface state deriving from different batches, supplier or production routes. Composites produced with surface-treated nanoparticles showed reproducible results displaying similar particles content and hardness values. Additionally, a pulse-reverse plating waveform, adapted to the nanoparticles average size, was designed and optimised to improve the particles codeposition.

The study of the impact of the reinforcer phase on the electrocrystallisation of the matrix showed a correlation between microstructure and particles size, chemistry and dispersion. The strengthening mechanisms were linked to the microstructural changes resulting from the process parameters, particles codeposition and the agitation mode. Different models were used to predict the hardness of the composites based on the contribution and combination of each strengthening factor, showing a good agreement with the experimental data.

The wear behaviour of the coatings was analysed and connected to the hardening effects, highlighting how the particles size, type, content, and dispersion affected the wear resistance. A novel multifunctional nanocomposite coating based on a dual dispersion mix of hard carbides and self-lubricant particles was designed, resulting in a surface with high hardness, low friction and low wear.



SANTIAGO PIÑATE is a doctoral candidate in the Department of Materials and Manufacturing at the School of Engineering, Jönköping University. He holds an Engineer's degree in Mining Engineering with a specialisation in Material Sciences from Universidad Politécnica de Madrid, Spain, and a M.Sc. degree in Product development and Material Engineering from Jönköping University. His research lies in the fields of material sciences, surface technology and manufacturing engineering.